AD-A250 023

ON PAGE

1. AGENCY USE ONLY (Leave blank)	2. REPORT DATE 2/29/92	3. REPORT TYPE AND DATES COVERED Final Report 10/1/89 – 12/31/91

4. TITLE AND SUBTITLE

Nonlinear Sloshing and the Coupled Dynamics of Liquid Propellants and Spacecraft

(U.)

5. FUNDING NUMBERS

AFOSR 89-0444

6. AUTHOR(S)

Tsung-chow Su

7. PERFORMING ORGANIZATION NAME(S) AND ADDRESS(ES)

Center for Applied Stochastics Research and Department of Ocean Engineering, Florida Atlantic University, Boca Raton, Florida

8. PERFORMING ORGANIZATION REPORT NUMBER

61102F
2302/B1

9. SPONSORING / MONITORING AGENCY NAME(S) AND ADDRESS(ES)

AFOSR /NA
Bolling AFB, DC 20332-6448

10. SPONSORING / MONITORING AGENCY REPORT NUMBER

AEOSR-TR· 92 0229

DTIC
ELECTE
APR 16 1992
S
D

11. SUPPLEMENTARY NOTES

12a. DISTRIBUTION / AVAILABILITY STATEMENT

Unlimited

This document has been approved for public release and sale; its distribution is unlimited.

12b. DISTRIBUTION CODE

D

13. ABSTRACT (Maximum 200 words)

Current and future space-based systems have rather complex mission requirements which demand the storage of large amounts of liquid propellants on board. With large controller bandwidths and rapid maneuvering of the spacecraft in a low gravity environment, potential coupling between the sloshing liquid, the spacecraft motion and structural modes need to be carefully evaluated to ensure the system design adequacy. For achieving the mission success, the first important step is to understand the nonlinear dynamics of the liquid sloshing.

The report summarizes a two-year study on the development and application of the numerical method for three-dimensional liquid sloshing simulation. Fluid dynamics and fluid loading, including total force and impact for the vessel undergoing rapid movement were simulated. Effects of baffles and active baffles with or without feedback mechanism for sloshing control were compared. It was found that moving baffles can be very effective in suppressing large amplitude sloshing. Complicated swirling intensification by drainage was also numerically simulated.

14. SUBJECT TERMS

Sloshing, Breaking wave, VOF method, active control

15. NUMBER OF PAGES
82

16. PRICE CODE

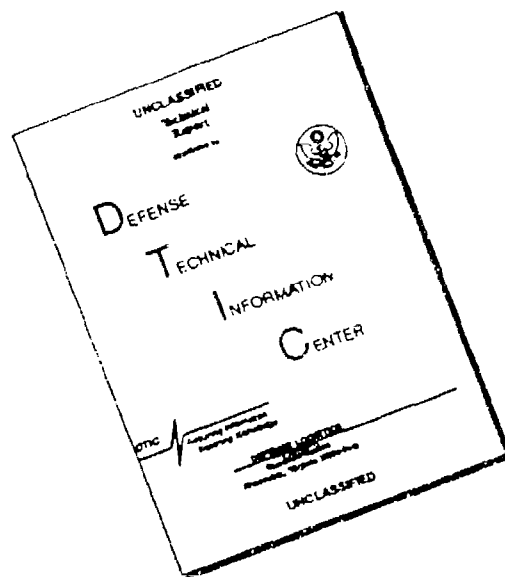| 17. SECURITY CLASSIFICATION OF REPORT	18. SECURITY CLASSIFICATION OF THIS PAGE	19. SECURITY CLASSIFICATION OF ABSTRACT	20. LIMITATION OF ABSTRACT
Unclassified	Unclassified	Unclassified	UL

DISCLAIMER NOTICE

THIS DOCUMENT IS BEST QUALITY AVAILABLE. THE COPY FURNISHED TO DTIC CONTAINED A SIGNIFICANT NUMBER OF PAGES WHICH DO NOT REPRODUCE LEGIBLY.

NONLINEAR SLOSHING AND THE COUPLED DYNAMICS
OF LIQUID PROPELLANTS AND SPACECRAFT

Final Report
(for the Period 01 October 89 - 31 December 91)

Submitted to
Air Force Office of Scientific Research

by

Dr. Tsung-chow Su
Professor of Ocean Engineering and
Center for Applied Stochastic Research
Florida Atlantic University
Boca Raton, Florida 33432

92-09761

The views and conclusions contained in this document are those of the authors and should not be interpreted as necessarily representing the official policies or endorsements, either expressed or implied, of the Air Force Office of Scientific Research or the U. S. Government.

TABLE OF CONTENTS

NONLINEAR SLOSHING AND THE COUPLED DYNAMICS OF LIQUID PROPELLANTS AND SPACECRAFT

ABSTRACT

Current and future space-based systems have rather complex mission requirements which demand the storage of large amounts of liquid propellants on board. With large controller bandwidths and rapid maneuvering of the spacecraft in a low gravity environment, potential coupling between the sloshing liquid, the spacecraft motion and structural modes need to be carefully evaluated to ensure the system design adequacy. For achieving the mission success, the first important step is to understand the nonlinear dynamics of the liquid sloshing.

The report summarizes a two-year study on the development and application of the numerical method for three-dimensional liquid sloshing simulation. Fluid dynamics and fluid loading, including total force and impact for the vessel undergoing rapid movement were simulated. Effects of baffles and active baffles with or without feedback mechanism for sloshing control were compared. It was found that moving baffles can be very effective in suppressing large amplitude sloshing. Complicated swirling intensification by drainage was also numerically simulated.

CHAPTER 1:   INTRODUCTION

Liquid sloshing in a moving container constitutes a broad class of problems of great practical importance in many engineering applications, such as tank truck accidents, tank car derailing, helicopter flip-over, liquid fuel sloshing in space rockets, movement of liquid cargo in ocean-going vessels, and on a much larger scale, the oscillations of water in lakes and harbors occurring as the result of earthquakes. The potential for significant loads resulting from sloshing liquids in containers has been realized for years. Such loads may cause structural damage, create a destabilization effect and produce environmental hazards.

Within the moving container, various types of sloshing waves can be created depending on the liquid depth and motion frequency. In an unbaffled tank, typical forms are standing waves, travelling waves, solitary waves, hydraulic jumps and a combination of these. Associated with these waves, impulsive and non-impulsive pressures can be created by a sloshing liquid. Impulsive pressures which are usually associated with hydraulic jump and travelling waves are localized, very high pressures, with a duration of 1-10 msec, caused by the impact of the liquid on the solid boundaries. Non-impulsive pressures are slowly varying dynamic pressures resulting from standing waves. Usually the most severe impact pressures occur on the boundaries near the stationary liquid level or at the corners of the container. In spite of harmonic excitation, these pressures are neither harmonic nor periodic. Various baffles produce complicated wave forms, most of which are not well understood.

The problem of sloshing has been studied by many investigators and rather comprehensive reference lists have been published on several occasions[1-5]. Most of these earlier investigations are concerned with fuel tanks for rockets for the space program. Much of the sloshing technology developed for space applications is limited to spherical and cylindrical containers, while the

1

nature of slosh loading in prismatic tanks is probably less understood. The emphasis was placed on frequencies and total forces as they relate to control system requirements and, therefore, the effects of local peak impact pressure on structural requirements were not studied to any extent. Further, the excitation amplitudes considered in space applications are too small for many other simulations such as ship motion[6]. Analytical techniques for predicting large amplitude sloshing are still not fully developed. The problem is essentially nonlinear and, therefore, few theories are available for predicting damping[7-11]. Our principal knowledge of damping characteristic remains the result of extensive experimental studies. A detailed description of sloshing and evaluation of slosh loads in marine applications has been given in a report by Cox, Bowles and Bass[12]. Several articles of fluid-structure vibration and liquid sloshing in reactor technology applications under earthquake excitation can be found in Ma and Su[13]. Sloshing in the dam-reservoir system, including fluid-structure interaction, has been investigated[14,15].

A linear mathematical model has been developed for rectangular tanks executing a roll oscillation by Graham[16] and Chu, et al.[17]. In their analytical and experimental study for ship-roll stabilization tanks, Chu, et al., have concluded that the antirolling tank is a nonlinear control element throughout its practical range of operation and that a nonlinear mathematical model must be developed before any significant gain over present design methods can be foreseen.

Nonlinear theories of forced oscillations of liquid in a rectangular container has been developed by Faltinsen[18] and Verhagen and Wijngaarden[19]. Both studies are concerned with the frequency range near the lowest resonance frequency and, although the nonlinear free surface condition has been used, only the _small_ amplitude roll motions of the container are considered. Furthermore, the analysis of Verhagen and Wijngaarden is based on shallow-water theory and its application is limited to the low fill depth case, while

2

the analysis of Faltinsen considers the depth of fluid is either O(1) or infinite. The comparison between theory and experiment has been made for each study. Both authors attributed the discrepancy between theory and experiment to the neglect of viscosity in the theory. Faltinsen mentioned that *"obvious nonlinearities are occurring and it is possible that viscous effects play a dominant role... further study must investigate the possibility of incorporating viscous effects in an approximate way in our potential theory."* In a later paper[20], Faltinsen developed a numerical nonlinear method for the study of sloshing based on the boundary integral technique. For small amplitude liquid sloshing study, the finite element method has been applied by Ikekawa[21] and the boundary element method has been used by Nakayama and Washizu[22].

For the study of large amplitude sloshing when the excitation is O(1), one has to use a numerical technique. Numerical techniques have been used to solve time-dependent incompressible fluid flow problems for more than 20 years. One of the best known techniques, the Marker-and-Cell (MAC) method, uses an Eulerian finite-difference formulation in which pressure and velocity are the primary dependent variables. Hirt, et al. of Los Alamos Scientific Laboratory developed a numerical solution algorithm (SOLA), using a finite difference technique based on the MAC method for solving the Navier-Stokes equations for an incompressible fluid[23]. An extension of the SOLA code, SOLA-SURF, permits a free surface to be located across the top of the fluid regions. Navickas, et al., modified the SOLA-SURF code to study sloshing of fluids at high-fill levels in closed tanks to predict cargo response characteristics in liquefied natural gas tankers at high loading levels due to both periodic and random excitations[24]. The recent sloshing R & D project at Lloyd's Register of Shipping also emphasizes the computer analysis of sloshing effects based on this SOLA-SURF code[25]. The principal restriction of the SOLA-SURF code is that the free surfaces must be definable by single-valued function. Also, the slope of the surface must not exceed the cell aspect

3

ratio $\sigma y/\sigma x$. In marine applications, large amplitude excitations are often anticipated with violent fluid response inevitable and these limitations become too restrictive. To overcome the difficulty of tracking the complicated fluid interface, further extension, SOLA-VOF, uses the volume of fluid technique[26] to track a free fluid surface.

In the VOF method, the volume of fluid function F is introduced, defined as unity at any point occupied by fluid, and zero elsewhere. The discrete value of F in a grid cell represents the fractional volume of the cell occupied by fluid. The distribution of F contains implicit information about the location of the interface without an excessive use of computer time. The multiple interacting free surfaces that occur in liquid sloshing in baffled tank are simply defined by the VOF method. Su, et al.[27,28], using the moving coordinate system with this volume of fluid technique, studied the nonlinear behavior and damping characteristics of liquid sloshing in partially filled enclosed prismatic tanks subjected to a large amplitude excitation for marine and land transportation applications. The liquid was assumed to be homogeneous and to remain laminar. Sloshing inside partially filled, enclosed, baffled tanks and unbaffled tanks was studied. Several baffle configurations were investigated and their effects on sloshing have been identified. A few comparisons between numerical results and experimental data have also been made with good agreement observed for both impact and non-impact type slosh loads. For large amplitude excitations, however, the liquid responded violently which, after an initial period, caused the numerical solution to become unstable. In an ensuing investigation, an improved donor-acceptor method which takes into account surface orientation and transports trapezoidal shapes from cell to cell is used. The improved algorithm extends the applicability of numerical sloshing simulation to permit repeated liquid impacts on the surface of the container[29,30,31]. Sufficient number of statistically distributed impact pressure can then be generated. Experimental investigation was carried out which verified the accuracy of wave height and

impact pressure computation[32]. Very recently, a three-dimensional finite-difference scheme based on the volume of fluid technique has been developed[33,34,35]. 3-D numerical simulation of sloshing in arbitrary containers becomes feasible.

Meanwhile, current and future spacecraft mission requirements demand the storage of large amounts of liquid propellants on board. Space applications again attract the attention of sloshing researchers[36,37,38]. Potential coupling between liquid and the remaining portion of the spacecraft can be expected due to large liquid mass fractions, large controller bandwidths, low frequency spacecraft modes, low-g conditions and rapid maneuverability requirements. Understanding the sloshing and the associated phenomena is essential to ensure the system design adequacy and the mission success. The objective of the research was to extend the recent progress of computational technique to understand and predict the dynamic response of liquid in partially filled moving containers relevant to spacecraft/space station applications and to apply this technique to achieve effective fuel tank design optimization and baffle selection.

CHAPTER 2. VOLUME OF FLUID TECHNIQUE FOR SLOSHING SIMULATION

The case to be considered is that of a three-dimensional, rigid, enclosed tank that is partially filled with a viscous liquid. The liquid is assumed to be homogeneous and to remain laminar. A general motion of a vehicle-fixed coordinate system (x,y,z) with respect to an inertial coordinate system is prescribed. The continuity equation for an incompressible fluid is given by

$$\frac{\partial}{\partial x}(\theta u) + \frac{\partial}{\partial y}(\theta v) + \frac{\partial}{\partial z}(\theta w) = 0 \tag{1}$$

The equations of motion are the Navier-stokes equations for Newtonian fluids

x--momentum equation,

$$\frac{\partial u}{\partial t} + u\frac{\partial u}{\partial x} + v\frac{\partial u}{\partial y} + w\frac{\partial u}{\partial z} = -\frac{1}{\rho}\frac{\partial p}{\partial x} + g_x + \nu\left[\frac{\partial^2 u}{\partial x^2} + \frac{\partial^2 u}{\partial y^2} + \frac{\partial^2 u}{\partial z^2}\right] \tag{2}$$

y--momentum equation,

$$\frac{\partial v}{\partial t} + u\frac{\partial v}{\partial x} + v\frac{\partial v}{\partial y} + w\frac{\partial v}{\partial z} = -\frac{1}{\rho}\frac{\partial p}{\partial y} + g_y + \nu\left[\frac{\partial^2 v}{\partial x^2} + \frac{\partial^2 v}{\partial y^2} + \frac{\partial^2 v}{\partial z^2}\right] \tag{3}$$

z--momentum equation,

$$\frac{\partial w}{\partial t} + u\frac{\partial w}{\partial x} + v\frac{\partial w}{\partial y} + w\frac{\partial w}{\partial z} = -\frac{1}{\rho}\frac{\partial p}{\partial z} + g_z + \nu\left[\frac{\partial^2 w}{\partial x^2} + \frac{\partial^2 w}{\partial y^2} + \frac{\partial^2 w}{\partial z^2}\right] \tag{4}$$

where

θ = the partial cell parameter

u = velocity of the fluid in the x direction

v = velocity of the fluid in the y direction

w = velocity of the fluid in the z direction

p = pressure

ρ = density of the fluid

ν = coefficient of kinematic viscosity

g_x = body acceleration in the x direction

6

g_y = body acceleration in the y direction

g_z = body acceleration in the z direction

The gravitational acceleration is included as part of body accelerations, which is the external forcing term of sloshing motion.

Finite difference representation of the governing partial differential equations is obtained as described in Reference [35]. The finite difference cells, which are composed of cuboid of length δx_i, width δy_j and height δz_k, are used for solving the governing equations numerically. A typical computational grid is illustrated in Fig. 1. The tank inside is divided into the IBAR cells in the x direction, JBAR cells in the y direction and KBAR cells in the z direction. A single layer of boundary cells surrounds the tank such that the total number of cells is IMAX (=IBAR+2) times JMAX (=JBAR+2) times KMAX (=KBAR+2). These fictitious cells are used to set regular boundary conditions so that the same difference equations used in interior cell can also be used at the boundaries. A staggered grid is used as shown in Fig. 2 with u--velocity at the right face of the cell, w--velocity at the front face of the cell, v--velocity at the top face of the cell, and pressure and F ' 'he volume of fluid function) at the cell center. Fig. 2 also shows the locations of the geometrical quantities AR, AT, AF, and VC, arising from the partial cell treatment, which are the fractions of the right cell face, top cell face, front cell face and cell volume open to flow. Geometrical arrays AR, AT, AF, and VC must be defined if an obstacle or a curved boundary is included in the mesh.

The finite difference approximation representing the continuity equation for a typical cell (i,j,k) is:

$$\frac{1}{VC_{i,j,k}} \left[\frac{1}{\delta x_i} (u^{n+1}_{i,j,k}AR_{i,j,k} - u^{n+1}_{i-1,j,k}AR_{i-1,j,k}) + \frac{1}{\delta y_j}(v^{n+1}_{i,j,k}AT_{i,j,k} - \right.$$

$$\left. v^{n+1}_{i,j-1,k}AT_{i,j-1,k}) + \frac{1}{\delta z_k} (w^{n+1}_{i,j,k}AF_{i,j,k} - w^{n+1}_{i,j,k-1}AF_{i,j,k-1}) \right] = 0 \qquad (5)$$

7

The finite difference approximation of momentum equations are:

$$u_{i,j,k}^{n+1} - u_{i,j,k}^{n} + \delta t \left[- \frac{1}{\delta x_{i+1/2}} (p_{i+1,j,k}^{n+1} - p_{i,j,k}^{n+1}) + GX - FUX - FUY - FUZ + VISX \right] \quad (6)$$

$$v_{i,j,k}^{n+1} - v_{i,j,k}^{n} + \delta t \left[- \frac{1}{\delta y_{j+1/2}} (p_{i,j+1,k}^{n+1} - p_{i,j,k}^{n+1}) + GY - FVX - FVY - FVZ + VISY \right] \quad (7)$$

$$w_{i,j,k}^{n+1} - w_{i,j,k}^{n} + \delta t \left[- \frac{1}{\delta z_{k+1/2}} (p_{i,j,k+1}^{n+1} - p_{i,j,k}^{n+1}) + GZ - FWX - FWY - FWZ + VISZ \right] \quad (8)$$

Where the convective and viscous fluxes in x direction are defined as:

$$FUX = (u_{i,j,k}^{n}/\delta x_{u}) \left[- \frac{\delta x_{i+1}}{\delta x_{i}} (u_{i,j,k}^{n} - u_{i-1,j,k}^{n}) + \frac{\delta x_{i}}{\delta x_{i+1}} (u_{i+1,j,k}^{n} - u_{i,j,k}^{n}) \right] +$$

$$(u_{i,j,k}^{n}/\delta x_{u})\alpha * sgn(u_{i,j,k}^{n}) \left[\frac{\delta x_{i+1}}{\delta x_{i}} (u_{i,j,k}^{n} - u_{i-1,j,k}^{n}) - \frac{\delta x_{i}}{\delta x_{i+1}} (u_{i+1,j,k}^{n} - u_{i,j,k}^{n}) \right] \quad (9)$$

$$\delta x_{u} = \delta x_{i} + \delta x_{i+1} + \alpha * sgn(u_{i,j,k}^{n}) (\delta x_{i+1} - \delta x_{i})$$

$$FUY = (v^{*}/\delta y_{u}) \left[\frac{\delta y_{j+1/2}}{\delta y_{j-1/2}} (u_{i,j,k}^{n} - u_{i,j-1,k}^{n}) - \frac{\delta y_{j-1/2}}{\delta y_{j+1/2}} (u_{i,j+1,k}^{n} - u_{i,j,k}^{n}) \right] +$$

$$(v^{*}/\delta y_{u})\alpha * sgn(v^{*}) \left[\frac{\delta y_{j+1/2}}{\delta y_{j-1/2}} (u_{i,j,k}^{n} - u_{i,j-1,k}^{n}) - \frac{\delta y_{j-1/2}}{\delta y_{j+1/2}} (u_{i,j+1,k}^{n} - u_{i,j,k}^{n}) \right] \quad (10)$$

$$\delta y_{j+1/2} = (\delta y_{j} + \delta y_{j+1})/2$$

$$\delta y_{j-1/2} = (\delta y_{j} + \delta y_{j-1})/2$$

$$\delta y_{u} = \delta y_{j+1/2} + \delta y_{j-1/2} + \alpha * sgn(v^{*}) (\delta y_{j+1/2} - \delta y_{j-1/2})$$

$$v^{*} = \frac{1}{2(\delta x_{i} + \delta x_{i+1})} \left[\delta x_{i}(v_{i+1,j,k}^{n} + v_{i+1,j-1,k}^{n}) + \delta x_{i+1}(v_{i,j,k}^{n} + v_{i,j-1,k}^{n}) \right]$$

$$FUZ = (w^{*}/\delta z_{u}) \left[\frac{\delta z_{k+1/2}}{\delta z_{k-1/2}} (u_{i,j,k}^{n} - u_{i,j,k-1}^{n}) + \frac{\delta z_{k-1/2}}{\delta z_{k+1/2}} (u_{i,j,k+1}^{n} - u_{i,j,k}^{n}) \right] +$$

$$(w^*/\delta z_u)\alpha * \mathrm{sgn}(w^*)\left[\frac{\delta z_{k+1/2}}{\delta z_{k-1/2}}(u^n_{i,j,k}-u^n_{i,j,k-1}) - \frac{\delta z_{k-1/2}}{\delta z_{k+1/2}}(u^n_{i,j,k+1}-u^n_{i,j,k})\right] \quad (11)$$

$$\delta z_{k+1/2} = (\delta z_k \div \delta z_{k+1})/2$$

$$\delta z_{k-1/2} = (\delta z_k + \delta z_{k-i})/2$$

$$\delta z_u = \delta z_{k+1/2} + \delta z_{k-1/2} + \alpha * \mathrm{sgn}(w^*)(\delta z_{k+1/2} - \delta z_{k-1/2})$$

$$w^* = \frac{1}{2(\delta x_i + \delta x_{i+1})}\left[\delta x_i(w^n_{i+1,j,k}+w^n_{i+1,j,k-1}) + \delta x_{i+1}(w^n_{i,j,k}+w^n_{i,j,k-1})\right]$$

$$\mathrm{VISX} = \nu\left(\frac{\partial^2 u}{\partial x^2} + \frac{\partial^2 u}{\partial y^2} + \frac{\partial^2 u}{\partial z^2}\right) \quad (12)$$

$$\frac{\partial^2 u}{\partial x^2} = \frac{1}{\delta x_{i+1/2}\delta x_{i+1}\delta x_i}\left[\delta x_i(u^n_{i+1,j,k}-u^n_{i,j,k}) - \delta x_{i+1}(u^n_{i,j,k}-u^n_{i-1,j,k})\right] \quad (13)$$

$$\frac{\partial^2 u}{\partial y^2} = \frac{2}{(\delta y_{j-1/2}+\delta y_{j+1/2})\delta y_{j+1/2}\,\delta y_{j-1/2}}$$

$$\left[\delta y_{j-1/2}(u^n_{i,j+1,k}-u^n_{i,j,k}) - \delta y_{j+1/2}(u^n_{i,j,k}-u^n_{i,j-1,k})\right] \quad (14)$$

$$\frac{\partial^2 u}{\partial z^2} = \frac{2}{(\delta z_{k-1/2}+\delta z_{k+1/2})\delta z_{k+1/2}\,\delta z_{k-1/2}}$$

$$\left[\delta z_{k-1/2}(u^n_{i,j,k+1}-u^n_{i,j,k}) - \delta z_{k+1/2}(u^n_{i,j,k}-u^n_{i,j,k-1})\right] \quad (15)$$

In the equal mesh condition,

$$\delta x_{i+1} = \delta x_i = \delta x_{i-1} = \delta x$$

$$\delta y_{j+1} = \delta y_j = \delta y_{j-1} = \delta y$$

$$\delta z_{k+1} = \delta z_k = \delta z_{k-1} = \delta z$$

9

The expressions for FUX, FUY, FUZ, VISX can be simplified as follows:

$$\text{FUX} = \frac{u^n_{i,j,k}}{2\delta x}\left[(1-A)u^n_{i+1,j,k} + 2Au^n_{i,j,k} - (1+A)u^n_{i-1,j,k}\right] \tag{16}$$

$$A = \alpha * \text{sgn}(u^n_{i,j,k})$$

$$\text{FUY} = \frac{v^*}{2\delta x}\left[(1-B)u^n_{i,j+1,k} + 2Bu^n_{i,j,k} - (1+B)u^n_{i,j-1,k}\right] \tag{17}$$

$$B = \alpha * \text{sgn}(v^*)$$

$$v^* = \frac{1}{4}(v^n_{i+1,j,k} + v^n_{i+1,j-1,k} + v^n_{i,j,k} + v^n_{i,j-1,k})$$

$$\text{FUZ} = \frac{w^*}{2\delta x}\left[(1-C)u^n_{i,j,k+1} + 2Cu^n_{i,j,k} - (1+C)u^n_{i,j,k-1}\right] \tag{18}$$

$$C = \alpha * \text{sgn}(w^*)$$

$$w^* = \frac{1}{4}(w^n_{i+1,j,k} + w^n_{i+1,j,k-1} + w^n_{i,j,k} + w^n_{i,j,k-1})$$

$$\text{VISX} = \frac{\nu}{\delta x^2}(u^n_{i+1,j,k} - 2u^n_{i,j,k} + u^n_{i-1,j,k})$$

$$+ \frac{\nu}{\delta y^2}(u^n_{i,j+1,k} - 2u^n_{i,j,k} + u^n_{i,j-1,k})$$

$$+ \frac{\nu}{\delta z^2}(u^n_{i,j,k+1} - 2u^n_{i,j,k} + u^n_{i,j,k-1}) \tag{19}$$

As the same way, we can define the expressions for convective and viscous fluxes in y and z direction, FVX, FVY, FVZ, VISY, FWX, FWY, FWZ and VISZ.

The coefficient α in these expressions gives the desired amount of upstream (donor cell) differencing; that is, when α is zero, these difference equations are second order accurate, centered difference approximation. When α is equal to unity, the equations reduce to the full upstream or donor cell

form. The proper choice for α is needed to insure numerical stability and is discussed later.

In order to satisfy these equations, the well-known SOLA-VOF algorithm is employed to satisfy the three difference equations in each control volume and to correct the results. At each time step, we must solve for the u--velocity, v--velocity, w--velocity and pressure in each control volume. Explicit approximations of the velocity field are obtained from the momentum equations, Eq. (6),(7),(8), using old time level values for the advective, pressure, viscous, and body force terms. In order to satisfy the continuity equations, the pressure (and velocities) must be adjusted in each computational cell occupied by fluid.

The finite-difference form of continuity equation (5) can be rewritten as

$$S = \frac{1}{VC_{i,j,k}} \left[\frac{1}{\delta x_i} (u^{n+1}_{i,j,k} AR_{i,j,k} - u^{n+1}_{i-1,j,k} AR_{i-1,j,k}) + \frac{1}{\delta y_j} (v^{n+1}_{i,j,k} AT_{i,j,k} \right.$$

$$\left. - v^{n+1}_{i,j-1,k} AT_{i,j-1,k}) + \frac{1}{\delta z_k} (w^{n+1}_{i,j,k} AF_{i,j,k} - w^{n+1}_{i,j,k-1} AF_{i,j,k-1}) \right] \qquad (20)$$

This equation is an implicit relation for the new pressures. A solution may be obtained by the iterative process. In each cell containing fluid, but not a free surface, the pressure change needed to drive the S of Eq. (20) toward zero is

$$\delta p = \frac{-S}{\partial S / \partial p} \qquad (21)$$

where S is evaluated with the most updated values of p,u,v, and w available, and the derivative is with respect to $p_{i,j,k}$. The equation (21) is derived by substituting the Eqs. (25) through (30) below into equation (20) and solving for δp. The quantity $\beta = 1/(\partial S / \partial p)$ is

$$\beta = \frac{VC_{i,j,k}}{2\delta t(\lambda_i + \lambda_{i-1} + \xi_j + \xi_{j-1} + \varsigma_k + \varsigma_{k-1})} . \qquad (22)$$

11

where

$$\lambda_i = \frac{AR_{i,j,k}}{\delta x_i (\delta x_i + \delta x_{i+1})}$$

$$\lambda_{i-1} = \frac{AR_{i-1,j,k}}{\delta x_i (\delta x_i + \delta x_{i-1})}$$

$$\xi_j = \frac{AT_{i,j,k}}{\delta y_j (\delta y_j + \delta y_{j+1})}$$

$$\xi_{j-1} = \frac{AT_{i,j-1,k}}{\delta y_j (\delta y_j + \delta y_{j-1})}$$

$$\zeta_k = \frac{AF_{i,j,k}}{\delta z_k (\delta z_k + \delta z_{k+1})}$$

and

$$\zeta_{k-1} = \frac{AF_{i,j,k-1}}{\delta z_k (\delta z_k + \delta z_{k-1})}$$

In equal mesh condition

$$\beta = \frac{VC_{i,j,k}}{\delta t \left[\frac{1}{\delta x^2} (AR_{i,j,k} + AR_{i-1,j,k}) + \frac{1}{\delta y^2} (AT_{i,j,k} + AT_{i,j-1,k}) + \frac{1}{\delta z^2} (AF_{i,j,k} + AF_{i,k,k-1}) \right]} \tag{23}$$

The new estimate for the cell pressure is then

$$P_{i,j,k} + \delta p \tag{24}$$

and new estimates for the velocities located on the sides of the cell are

$$u_{i,j,k} + \frac{\delta t \delta p}{\delta x_i} \tag{25}$$

$$u_{i-1,j,k} - \frac{\delta t \delta p}{\delta x_i} \tag{26}$$

$$v_{i,j,k} + \frac{\delta t \delta p}{\delta y_j} \tag{27}$$

$$v_{i,j-1,k} - \frac{\delta t \delta p}{\delta y_j} \tag{28}$$

$$w_{i,j,k} + \frac{\delta t \delta p}{\delta z_k} \tag{29}$$

$$w_{i,j,k-1} + \frac{\delta t \delta p}{\delta z_k} \tag{30}$$

This procedure is modified for cells containing a free surface. For these cells, the free surface boundary condition is satisfied by setting the surface cell pressure $p_{i,j,k}$ equal to the value obtained by a linear interpolation between the pressure wanted at the surface p_s and a pressure of its interpolation cell inside the fluid p_n, so the S function is:

$$S = (1-\eta)p_n + \eta p_s - p_{i,j,k} \tag{31}$$

where $\eta = d_c/d_s$ is the ratio of the distance between the cell centers and the distance between the free surface and the center of the interpolation cell as shown in Fig. 3. A δp is obtained from the new p_n and the old $p_{i,j,k}$ and the new $p_{i,j,k}$ is obtained interactively by under-relaxation.

Before using Eq. (31) for surface cell interpolation, we must first determine the distance d_s, the distance between the free surface and the center of the interpolation cell. Since the free surface is assumed either nearly horizontal or vertical in original VOF method, the real surface in Fig. 4(a) is treated as the surface in Fig. 4(b). Therefore, the free surface condition does not impose the right position and large error can occur due to this approximation. This situation may become even worse in three-dimensional problem, the free surface of which is far more complex. The algorithm of determining distance d_s is improved in Reference [35]. The free surface is treated as a plane. The slopes of plane AN and BN are computed by the F value of its adjacent cells and discussed in the next section. The distance d_s is

determined by letting the volume between the plane and bottom face be equal to the F value of surface cell. Fig. 5 illustrates the positions of two kinds of approximate plane in surface cell. In the case of Fig. 5(a), the plane is entirely in the surface cell and F value in surface cell satisfies

$$F > \frac{BN}{2}\overline{\delta x} + \frac{AN}{2}\overline{\delta z} \tag{32}$$

where, $\overline{\delta x} = \delta x/\delta y$ and $\overline{\delta z} = \delta z/\delta y$. The distance d_s is

$$d_s = (0.5 + F_{i,j,k})\delta y \tag{33}$$

In the case of Fig. 5(b), the approximate plane intersects the bottom face of surface cell and F value in surface cell satisfies

$$F < \frac{BN}{2}\overline{\delta x} + \frac{AN}{2}\overline{\delta z} \tag{34}$$

Through geometrical analysis in this case, we can obtain the distance d_s as follows:

$$d_s = \left[(0.5 + \frac{BN}{2}\overline{\delta x} + \frac{AN}{2}\overline{\delta z}) - \overline{\delta} \right] \delta y \tag{35}$$

$\overline{\delta}$ in Eq. (35) is one of the roots of the following cubic algebraic equation

$$\overline{\delta}^3 + p\overline{\delta} + q = 0 \tag{36}$$

where

$$p = -6(AN)(BN)\,\overline{\delta x}\,\overline{\delta z}$$

$$q = 6(AN)(BN)\,\overline{\delta x}\,\overline{\delta z}\,(\frac{BN}{2}\overline{\delta x} + \frac{AN}{2}\overline{\delta z} - F_{i,j,k})$$

A complete iteration, therefore, consists of adjusting pressures and velocities in all cells occupied by fluid according to Eq. (24) through Eq. (30). Convergence of the iteration is achieved when all cells have S values whose magnitudes are below some small number, ϵ. Typically, ϵ is of order 10^{-3}, although it can vary with the problem being solved and the units

chosen for the problem. The last iterated quantities of velocity and pressure are taken as the advanced time values.

In some cases, convergence of iteration can be accelerated by multiplying δp from Eq. (21) by an over-relaxation factor ω. A value of $\omega = 1.7$ has provided relatively efficient results, but the optimal value is flow-dependent. A value of two or greater gives an unstable iteration. In practice, the free surface condition, Eq. (31) leads to an over-relaxation type of instability when the interpolation factor ω is greater than one. Stability can be insured by under-relaxing the pressure variations in cells used as interpolation neighbors for surface cells.

Tracking the free surface is essential in a free surface flow computation. The free surface is treated by introducing a function $F(x,y,z,t)$ that is defined to be unity at any point occupied by the fluid and zero elsewhere. Thus, F=1 implies a cell full of fluid, while F=0 denotes an empty cell. A cell with F values between zero and one are partially filled with fluid; they are either intersected by a free surface or contain voids (bubbles) smaller than cell mesh dimensions. A free surface cell (i,j,k) is defined as a cell containing a non-zero value of F and having at least one neighboring cell (i±1,j,k), (i,j±1,k), (i,j,k±1), that contains a zero value of F. The F function is utilized to determine which cells contain a boundary and where the fluid is located in those cells. Additionally, the derivatives of F can be used to determine the mean local surface normal, and using also the cell F value, to construct a plane cutting the cell that will approximate the interface.

The time dependence of F is governed by

$$\frac{\partial F}{\partial t} + u\frac{\partial F}{\partial x} + v\frac{\partial F}{\partial y} + w\frac{\partial F}{\partial z} = 0 \tag{37}$$

We combine Eq. (37) and continuity equation (1) to obtain

$$\frac{\partial}{\partial t}(\theta F) + \frac{\partial}{\partial x}(\theta uF) + \frac{\partial}{\partial y}(\theta vF) + \frac{\partial}{\partial z}(\theta wF) = 0 \tag{38}$$

15

where Θ is the partial cell parameter defined as before. The difference approximation of Eq. (38) is

$$F^{n+1}_{i,j,k} = F_{i,j,k}$$

$$- \frac{\delta t}{VC_{i,j,k}} \left[\frac{1}{\delta x_i} (AR_{i,j,k} u^{n+1}_{i,j,k} F_{i,j,k} - AR_{i-1,j,k} u^{n+1}_{i-1,j,k} F_{i-1,j,k}) \right.$$

$$+ \frac{1}{\delta y_j} (AT_{i,j,k} v^{n+1}_{i,j,k} F_{i,j,k} - AT_{i,j-1,k} v^{n+1}_{i,j-1,k} F_{i,j-1,k})$$

$$+ \left. \frac{1}{\delta z_k} (AF_{i,j,k} w^{n+1}_{i,j,k} F_{i,j,k} - AF_{i,j,k-1} w^{n+1}_{i,j,k-1} F_{i,j,k-1}) \right] \qquad (39)$$

which serves as the basis for the convection of F.

The convection algorithm must (1) preserve the sharp definition of free boundaries; (2) avoid negative diffusion truncation errors; and (3) not flux more fluid, or more void, across a computing cell interface than the cell losing the flux contains. To accomplish this, a type of donor-acceptor flux approximation from original SOLA-VOF is improved and employed in Reference (35). In this FAU modified VOF technique, it is assumed that the fluid/void interface is a plane segment cutting through the surface cell. So all the surface physics algorithms must be improved.

The basic orientation of a surface cell is described by the parameter NF through its numerical values 1, 2, 3, 4, 5, or 6. The definition of numerical values for the NF is specified in Table 1. The differential geometry describing the surface curvatures depends strongly on the numerical value selected for NF; it is important to make an appropriate choice for NF.

Nevertheless it has not been possible to devise a completely satisfactory algorithm of general applicability of the choice of NF values. The algorithms that are currently implemented in the FAUMVOF code suffice to provide reasonable simulations for the problems to which the code has been applied so far.

16

TABLE 1

DEFINITION OF VALUES FOR NF

NF=0   fluid cell, contains fluid and has no void adjacent to any of its faces.

NF=1   surface cell, fluid most nearly on the left of the surface cell.

NF=2   surface cell, fluid most nearly on the right of the surface cell.

NF=3   surface cell, fluid most nearly under the bottom of the surface cell.

NF=4   surface cell, fluid most nearly above the top of the surface cell.

NF=5   surface cell, fluid most nearly in the back of the surface cell.

NF=6   surface cell, fluid most nearly in the front of the surface cell.

NF=7   isolated cell, contains fluid but all cells adjacent to one of its faces are void.

NF=8   void cell, contains no fluid.

We calculate the value of NF by deciding where the fluid is mostly located. If surface cell has only one empty adjacent cell, the value of NF is made by choosing the adjacent cell opposite to empty cell, that cell is also the interpolation neighbor fluid cell. For example, the value of NF is 3 and cell $(i,j-1,k)$ is the interpolation neighbor fluid cell, if cell $(i,j+1,k)$ is only empty cell of surface cell (i,j,k). If surface cell has two empty adjacent cells, the value of NF is made by choosing from the two adjacent cells opposite the empty cells, that cell with the largest F value, i.e., containing the most fluid, to be the interpolation neighbor fluid cell. For example, if two adjacent cells, cell $(i+1,j,k)$ and cell $(i,j+1,k)$ are the empty cells and F value of cell $(i-1,j,k)$ is greater than that of cell $(i,j-1,k)$, the value of NF is 1 and cell $(i-1,j,k)$ is chosen as interpolation neighbor fluid cell.

The two slopes of the interface AN and BN can be defined according to the value of NF and are discussed at the end of this section. The interface is approximately represented by a plane equation at its local coordinates $\xi_x \xi_y \xi_z$. For example, if value of NF is 3, the local coordinate is such that its origin is at the center of bottom face of the surface cell and ξ_y is upward. The plane equation is given by

$$\xi_y = \gamma_0 + BN\xi_x + AN\xi_z \qquad\qquad 0 < \xi_y < \delta y_j \qquad\qquad (40)$$

two restrictions for ξ_y are

$$\xi_y = \delta y_j \qquad\qquad\qquad\qquad \xi_y > \delta y_j \qquad\qquad (41)$$

$$\xi_y = 0 \qquad\qquad\qquad\qquad\qquad \xi_y < 0 \qquad\qquad (42)$$

where γ_0 is the distance between the free surface and bottom face of the surface cell. From the definition of $\eta = d_c/d_s$ in Eq. (31), we can obtain γ_0 as:

$$\gamma_0 = d_c(1/\eta - 0.5) \qquad\qquad\qquad\qquad (43)$$

The improved donor-acceptor method is employed to calculate the advection of F through the cells. First, at each face of each computing cell, the two cells immediately adjacent to the interface are distinguished, one becoming a donor cell and the other an acceptor cell, and cell quantities are given the subscripts D and A, respectively, e.g., F_D, F_A. The labeling is accomplished by means of the algebraic sign of the fluid velocity normal to the face; the donor cell is always upstream, and the acceptor cell downstream, of the face. We emphasize that the D and A labels are assigned separately for each cell face. Thus, each computational cell will have six separate assignments of D or A corresponding to each of its cell face.

The amount of F fluxed across the donor cell face in one time step can be calculated for different value of NF. Fig. 6 gives an illustration of F-advection in the typical case when NF=3. In this case, the amount of F

18

across the right face of the cell at one time step δt is ΔF_x shown in Fig. 6(a). By the partitioning of the δz_k into M equal subdivisions, each of length $\delta \xi_z$, and with midpoints $\xi_{z1}, \ldots, \xi_{zm}, \ldots, \xi_{zM}$, we can obtain the ΔF_x as

$$\Delta F_x = \frac{u\delta t}{\delta y_j \delta z_k} \sum_{m=1}^{M} \xi_y (\frac{1}{2} \delta x_i - \frac{1}{2} u\delta t, \xi_{zm}) \delta \xi_z \qquad (44)$$

The amount of F fluxed across the top face of the cell at one time step is ΔF_y shown in Fig. 6(b). Again by the partitioning of the δx_i into L equal subdivisions, each of length $\delta \xi_x$, and the midpoints $\xi_{x1}, \ldots, \xi_{x1}, \ldots, \xi_{xL}$, we can obtain the ΔF_y as

$$\Delta F_y = \frac{1}{\delta x_i \delta z_k} \sum_{l=1}^{L} \sum_{m=1}^{M} \xi_y^* \delta \xi_x \delta \xi_z \qquad (45)$$

where

$$\xi_y^* = \text{MAX} \left[\xi_y (\xi_{x1}, \xi_{zm}) - (\delta y_j - v\delta t), \ 0 \right] \qquad (46)$$

The amount of F across the front face of the cell at one time step is ΔF_z shown in Fig. 6(c). We can obtain the ΔF_z as

$$\Delta F_z = \frac{w\delta t}{\delta x_i \delta y_j} \sum_{l=1}^{L} \xi_y (\xi_{x1}, \frac{1}{2} \delta z_k - \frac{1}{2} w\delta t) \delta \xi_x \qquad (47)$$

To prevent the fluxing of more fluid from the donor cell than it contains, the following restrictions are applied to ΔF_x, ΔF_y and ΔF_z

$$\Delta F_x = \text{MIN} \left[\Delta F_x, \ F_D \delta x_D VC_D / AR_{i,j,k} \right] \qquad (48)$$

$$\Delta F_y = \text{MIN} \left[\Delta F_y, \ F_D \delta y_D VC_D / AT_{i,j,k} \right] \qquad (49)$$

$$\Delta F_z = \text{MIN} \left[\Delta F_z, \ F_D \delta z_D VC_D / AF_{i,j,k} \right] \qquad (50)$$

The complete fluxing algorithm is applied independently at the six computing cell faces. When the necessary fluxes have been computed, F is advanced through one time step using Eq. (39).

19

Sometimes, above F-advection algorithm will generate spurious small wisps of fluid in the void cells of the computing mesh. An algorithm used to suppress these spurious wisps of fluid is to set a lower bound for F, i.g. 0.05. If a surface cell is trying to flux material into an empty cell, the flux is set to zero until it is greater than 0.05. The limiting value of 0.05 may not be optimal for all problems.

Truncation errors and rounding errors can cause F-values determined by the above procedure to occasionally have values slightly less than zero or slightly greater than unity. Therefore, after the advection calculation has been completed, a pass is made through the mesh to reset values of F less than zero back to zero and values of F greater than one back to one. Accumulated error in fluid volume introduced by these adjustments are recorded and may be printed at any time.

There is a final adjustment needed in F so that it may be used as a boundary cell flag. Boundary cells have values of F lying between zero and one. However, in a numerical solution, F-values cannot be tested against an exact number like zero and one because rounding rounding errors would cause spurious results. Instead, a cell is defined to be empty of F when F is less than EMF and full when F is greater than 1-EMF, where EMF is typically 10^{-6}. If, after advection, a cell has an F value less than EMF, this F is set to zero and all neighboring full cells become surface cells by having their F-values reduced from unity by an amount 1.1*EMF. These changes in F are also included in the accumulated volume error. Volume errors, after hundreds of cycles, are typically observed to be a fraction of 1% of the total F volume.

Following the calculation of the new F-values for all cells, the new cell types are redefined and appropriate flags NF are assigned. At the same time, the approximate orientation of the fluid in each surface cell is determined and a pressure interpolation neighbor cell is assigned. The slope of inter-face is estimated by introducing six surface-height functions $\partial Y/\partial Z$, $\partial Y/\partial X$, $\partial Z/\partial X$, $\partial Z/\partial Y$, $\partial X/\partial Y$, $\partial X/\partial Z$ based on the values of F in the surface cell and

20

its neighbors. The good approximations to these functions are:

$$\frac{\partial Y}{\partial Z} = \frac{2(Y_{i,k+1} - Y_{i,k-1})}{\delta z_{k+1} + 2\delta z_k + \delta z_{k-1}} \tag{51}$$

$$Y_{i,k+1} = F_{i,j-1,k+1}\delta y_{j-1} + F_{i,j,k+1}\delta y_j + F_{i,j+1,k+1}\delta y_{j+1}$$

$$Y_{i,k-1} = F_{i,j-1,k-1}\delta y_{j-1} + F_{i,j,k-1}\delta y_j + F_{i,j+1,k-1}\delta y_{j-1}$$

$$\frac{\partial Y}{\partial X} = \frac{2(Y_{i+1,k} - Y_{i-1,k})}{\delta x_{i+1} + 2\delta x_i + \delta x_{i-1}} \tag{52}$$

$$Y_{i+1,k} = F_{i+1,j-1,k}\delta y_{j-1} + F_{i+1,j,k}\delta y_j + F_{i+1,j+1,k}\delta y_{j+1}$$

$$Y_{i-1,k} = F_{i-1,j-1,k}\delta y_{j-1} + F_{i-1,j,k}\delta y_j + F_{i-1,j+1,k}\delta y_{j+1}$$

$$\frac{\partial Z}{\partial X} = \frac{2(Z_{i+1,j} - Z_{i-1,j})}{\delta x_{i+1} + 2\delta x_i + \delta x_{i-1}} \tag{53}$$

$$Z_{i+1,j} = F_{i+1,j,k-1}\delta z_{k-1} + F_{i+1,j,k}\delta z_k + F_{i+1,j,k+1}\delta z_{k+1}$$

$$Z_{i-1,j} = F_{i-1,j,k-1}\delta z_{k-1} + F_{i-1,j,k}\delta z_k + F_{i-1,j,k+1}\delta z_{k+1}$$

$$\frac{\partial Z}{\partial Y} = \frac{2(Z_{i,j+1} - Z_{i,j-1})}{\delta y_{j+1} + 2\delta y_j + \delta y_{j-1}} \tag{54}$$

$$Z_{i,j+1} = F_{i,j+1,k-1}\delta z_{k-1} + F_{i,j+1,k}\delta z_k + F_{i,j+1,k+1}\delta z_{k+1}$$

$$Z_{i,j-1} = F_{i,j-1,k-1}\delta z_{k-1} + F_{i,j-1,k}\delta z_k + F_{i,j-1,k+1}\delta z_{k+1}$$

$$\frac{\partial X}{\partial Y} = \frac{2(X_{j+1,k} - X_{j-1,k})}{\delta y_{j+1} + 2\delta y_j + \delta y_{j-1}} \tag{55}$$

$$X_{j+1,k} = F_{i-1,j+1,k}\delta x_{i-1} + F_{i,j+1,k}\delta x_i + F_{i+1,j+1,k}\delta x_{i+1}$$

$$X_{j-1,k} = F_{i-1,j-1,k}\delta x_{i-1} + F_{i,j-1,k}\delta x_i + F_{i+1,j-1,k}\delta x_{i+1}$$

$$\frac{\partial X}{\partial Z} = \frac{2(X_{j,k+1} - X_{j,k-1})}{\delta z_{k+1} + 2z_k + z_{k-1}} \tag{56}$$

21

$$X_{j,k+1} = -F_{i-1,j,k+1}\,\delta x_{i-1} + F_{i,j,k+1}\,\delta x_i + F_{i+1,j,k+1}\,\delta x_{i+1}$$

$$X_{j,k-1} = -F_{i-1,j,k-1}\,\delta x_{i-1} + F_{i,j,k-1}\,\delta x_i + F_{i+1,j,k-1}\,\delta x_{i-1}$$

For each surface having certain NF value, the slope of the interface AN and BN can be assigned according to the definition in Table 2.

TABLE 2

THE DEFINITION OF VALUES FOR AN AND BN

NF = 1,2	$AN = \dfrac{\partial X}{\partial Y}$	$BN = \dfrac{\partial X}{\partial Z}$
NF = 3,4	$AN = \dfrac{\partial Y}{\partial Z}$	$BN = \dfrac{\partial Y}{\partial X}$
NF = 5,6	$AN = \dfrac{\partial Z}{\partial X}$	$BN = \dfrac{\partial Z}{\partial Y}$

In addition to the free surface boundary condition, it is necessary to set conditions at all mesh boundaries and at surface of all internal obstacles. At the mesh boundaries, a variety of conditions may be set using the layer of fictitious cells surrounding the mesh. Consider, for example, the left boundary; if this is a rigid-free slope wall, the normal velocity there must be zero and the tangential velocity should have no normal gradient, i.e.

$$u_{1,j,k} = 0$$
$$v_{1,j,k} = v_{2,j,k}$$
$$w_{1,j,k} = w_{2,j,k} \tag{57}$$
$$P_{1,j,k} = P_{2,j,k}$$
$$F_{1,j,k} = F_{2,j,k}$$

If the left boundary is a no-slip rigid wall, then the tangential velocity component at the wall should also be zero, i.e.

$$u_{1,j,k} = 0$$

$$v_{1,j,k} = -v_{2,j,k}$$

$$w_{1,j,k} = -w_{2,j,k} \qquad\qquad (58)$$

$$P_{1,j,k} = P_{2,j,k}$$

$$F_{1,j,k} = F_{2,j,k}$$

Boundary conditions similar to those for the left wall are used at the right, front, back, top and bottom boundaries of the mesh. In the case of a tank with baffles, velocities are set to zero all the time for the interior obstacles and the other variables are maintained at their initial values.

In practice, non-rectangular containers such as cylindrical and spherical containers are commonly used. The boundary treatment for rectangular tank wall will encounter severe difficulties when curved boundary is encountered. For a free-slip condition on tank wall, the following must occur: (a) the velocity normal to a boundary surface is zero; (b) the tangential velocity does not have normal gradient; and (c) the divergence of a boundary cell is zero. In this research, an improved partial cell treatment is developed to fulfill the above three conditions. The partial cell is defined as the cell that intersects curved boundary or internal obstacle. The curved boundary surface is approximated by a plane. The basic orientation of the plane is described by the parameter NFB through its numerical values 1, 2, 3, 4, 5, or 6. The definition of numerical values for the NFB is specified in Table 3.

The value of NFB is only dependent on mesh division and does not change through the computation. The two slopes of the boundary plane, ANB and BNB can be assigned according to the definition in Table 4.

23

TABLE 3

DEFINITION OF VALUES FOR NFB

NFB=-1   obstacle cell, all faces of the cell are closed.

NFB= 1   partial cell, the right face of the cell is closed.

NFB= 2   partial cell, the left face of the cell is closed.

NFB= 3   partial cell, the bottom face of the cell is closed.

NFB= 4   partial cell, the top face of the cell is closed.

NFB= 5   partial cell, the front face of the cell is closed.

NFB= 6   partial cell, the back face of the cell is closed.

TABLE 4

THE DEFINITION OF VALUES FOR ANB AND BNB

$$NF = 1,2 \qquad ANB = \frac{\partial X}{\partial Y} \qquad BNB = \frac{\partial X}{\partial Z}$$

$$NF = 3,4 \qquad ANB = \frac{\partial Y}{\partial Z} \qquad BNB = \frac{\partial Y}{\partial X}$$

$$NF = 5,6 \qquad ANB = \frac{\partial Z}{\partial X} \qquad BNB = \frac{\partial Z}{\partial Y}$$

In the improved partial cell treatment, the normal and tangential velocity conditions on the boundary plane are first considered. Fig. 7 gives an illustration for the case when NFB=2. In this case, the fluid is mostly on the right side of the boundary plane and the left side of the boundary is closed. The unknown velocity component $u_{i-1,j,k}$ is set so that the zero velocity normal to a boundary surface is fulfilled. The normal velocity u_n

can be written as

$$u_n = u\cos(n,x) + v\cos(n,y) + w\cos(n,z) \qquad (59)$$

Three direction cosine, $\cos(n,x)$, $\cos(n,y)$ and $\cos(n,z)$ are given by

$$\cos(n,x) = \frac{1}{\sqrt{ANB^2 + BNB^2 + 1}}$$

$$\cos(n,y) = \frac{-ANB}{\sqrt{ANB^2 + BNB^2 + 1}} \qquad (60)$$

$$\cos(n,z) = \frac{-BNB}{\sqrt{ANB^2 + BNB^2 + 1}}$$

u, v, and w are the average velocities in x, y, and z direction, respectively, and are expressed as:

$$u = \lambda u_{i-1,j,k} + (1-\lambda)u_{i,j,k}$$

$$v = \frac{1}{2}(v_{i,j-1,k} + v_{i,j,k}) \qquad (61)$$

$$w = \frac{1}{2}(w_{i,j,k-1} + w_{i,j,k})$$

where $\lambda = \gamma_b/\delta x_i$; γ_b is the distance between the boundary face and the center

of right face, as shown in Fig. 7(a). By substituting Eq. (60) and Eq. (61)

into Eq. (59) and letting left side of Eq. (59) be zero, we can obtain

$u_{i-1,j,k}$ as follows

$$u_{i-1,j,k} = -\frac{1-\lambda}{\lambda}u_{i,j,k} - \frac{1}{2\lambda\cos(n,x)}(v_{i,j-1,k} + v_{i,j,k})\cos(n,y)$$

$$- \frac{1}{2\lambda\cos(n,x)}(w_{i,j,k-1} + w_{i,j,k})\cos(n,z) \qquad (62)$$

Now, the continuity equation (20) is satisfied by adjusting the partial cell pressure. The difference between the partial cell and interior cell is the value of partial cell geometrical quantities $VC_{i,j,k}$, $AR_{i,j,k}$, $AT_{i,j,k}$, and $AF_{i,j,k}$. $VC_{i,j,k}$ is the fractional volume of cell (i,j,k) open to fluid; $AR_{i,j,k}$, $AT_{i,j,k}$, and $AF_{i,j,k}$ are the fractions of the area of the right face, the top face and the front face of cell (i,j,k) that is open to flow. These geometrical quantities need to calculate according to the definition. Fig. 7(b) is the example for the case when NFB=2. It is noted that all these geometrical quantities are simply set to 1 for interior cell.

For the free surface boundary conditions, the stress tangential to the surface must vanish; therefore, the velocities of both fluids must be equal and the stress normal to the free surface must be exactly balanced by externally applied normal stresses.

In the finite difference scheme, the normal free surface boundary condition is satisfied by setting the surface cell pressures $p_{i,j,k}$ equal to the value calculated by a linear interpolation between the surface pressure p_s and pressure p_n of the adjacent cell. In the absence of the surface tension, the pressure at the free surface is set equal to the atmospheric pressure.

The tangential free surface boundary condition is satisfied by setting velocities on every cell boundary between a surface cell and an empty cell.

If the surface cell has only one neighboring empty cell, the boundary velocity is set to insure the vanishing of velocity divergence defined in Eq. (20). When there are two or more empty neighbor cells, the individual contributions to the divergence $\frac{\partial u}{\partial x}$, $\frac{\partial v}{\partial y}$, $\frac{\partial w}{\partial z}$ are separately set to zero.

Numerical calculations often have computed quantities that develop large, high-frequency oscillations in space, time, or both. This behavior is usually referred to as a numerical instability, especially if the physical problem being studied is known not to have unstable solutions. When the physical problem does have unstable solutions and if the calculated results exhibit

significant variations over distances comparable to a cell width or over times comparable to the time increment, the accuracy of the results cannot be relied on. To prevent this type of numerical instability or inaccuracy, certain restrictions must be observed in defining the mesh increments δx_i, δy_j and δz_k, the time increment δt, and the upstream differencing parameter α.

For accuracy, the mesh increments must be chosen small enough to resolve the expected spatial variations in all dependent variables. The choice of the time increment necessary for stability is governed by two restrictions. First, the convective limit (the Courant condition). The material cannot move through more than one cell in one time step because the difference equations assume fluxes only between adjacent cells. The numerical expression may be written as

$$\delta t < \text{MIN} \left\{ \frac{\delta x_i}{|u_{i,j,k}|} \,, \, \frac{\delta y_j}{|v_{i,j,k}|} \,, \, \frac{\delta z_k}{|w_{i,j,k}|} \right\} \tag{63}$$

where the minimum is taken over all cells of the computing mesh, but it is usual to require that δt be no more than a small fraction, e.g., 1/4 of the minimum cell transit time.

Second, the diffusive limit states that when a non-zero value of kinematic viscosity is used, momentum must not diffuse more than approximately one cell in one time step. A linear stability analysis shows that this limitation implies

$$\nu \delta t < \frac{1}{2} \left(\frac{1}{\delta x_i^2} + \frac{1}{\delta y_j^2} + \frac{1}{\delta z_k^2} \right)^{-1} \tag{64}$$

with δt chosen to satisfy the above two inequalities, the parameter α describing the proportion of donor cell differencing should have

$$1 > \alpha > \text{MAX} \left\{ \left| \frac{u_{i,j,k} \delta t}{\delta x_i} \right| \,, \, \left| \frac{v_{i,j,k} \delta t}{\delta y_j} \right| \,, \, \left| \frac{w_{i,j,k} \delta t}{\delta z_k} \right| \right\} \tag{65}$$

As a rule of thumb, an α approximately 1.2 to 1.5 times larger than the right-hand member of the last inequality is a good choice. If α is too large, an unnecessary amount of numerical smoothing (diffusion-like truncation errors) may be introduced.

This improvement of the volume of fluid (VOF) technique allows the numerical simulation of three-dimensional liquid sloshing in a container of arbitrary geometry. Major improvements were the taking into account of free surface orientation, transporting hexahedral shape fluid volume from cell to cell and considering the normal and tangential velocity boundary conditions on curved solid boundaries in partial cell treatments. The following chapters describe simulation results in various application conditions.

CHAPTER 3: SUBHARMONIC RESPONSES UNDER VERTICAL EXCITATION AND ITS CONTROL BY BAFFLESINTRODUCTION

It is known that vertical vibration causes a quiescent liquid surface to become unstable and the frequency of surface oscillations usually occurs at exactly one-half that of the container motion[39]. As part of the algorithm testing, numerical experiments are carried out to examine certain phenomena associated with flow instability.

A rectangular tank of 25.4 cm long, 25.4 cm wide and 35.56 cm high is used for the numerical simulation. Two different water depths[h] are chosen, h = 19.05 cm for deep water care and h = 6.35 cm for shallow water sloshing. Zero initial velocity field and hydrostatic pressure distribution are first assumed. Later, a small velocity perturbation with horizontal component u_o = 0.127 cm/s and vertical component v_o = 0.127 cm/s are introduced to accelerate the growth of instability. In all cases, vertical harmonic excitations $y_o \sin \omega t$ are applied with maximum amplitude of y_o = 1.27 cm and the exciting frequency ω slightly greater than twice of the first linear natural sloshing frequency ω_N.

Deep Water Sloshing

Sloshing in the tank without baffles. The frequency of forced oscillation is chosen as 22.258 rad/s ($2.04\omega_N$). The computed free surfaces are shown in Fig. 8(a) through Fig. 8(e) at five different times; 2.95s(10.5T), 3.24s(11.5T), 3.81s(13.5T), 4.09s(14.5T) and 4.37s(15.5T). T is the period of forced oscillation. Fig. 8(f) shows the free surface at 4.37s(15.5T) without higher order initial velocity perturbation. The computed velocity-vector field on vertical (x,y) and (z,y) planes are shown in Fig. 9. In the figures, Section I and K are parallel to the left wall of the tank and parallel to the front wall of the tank respectively. The subharmonic responses of free surface are indeed observed in the simulation results. That is, the surface wave only oscillates half period when the forced-oscillation passes one

29

period. Since the natural frequency of free sloshing in x direction is equal to that in z direction due to the tank configuration, the subharmonic responses occur in the both directions at the same time. As a result, the free surface waves are obviously three-dimensional, with maximum wave height on the tank corner. It is noted that vertical oscillation causes a quiescent free surface to become unstable. Once this occurs, the amplitudes of surface wave increase rapidly. In this numerical example, the surface wave finally impacts the tank top and then breaks with bubbles in the liquid.

The higher-order initial velocity perturbation is used to stimulate the dynamic instability of vertical sloshing. The numerical results proved this to be very effective. The idea of using higher-order perturbation is also reasonable because there always exists perturbations in physical problems.

Sloshing in the tank with horizontal splitter ring. The horizontal splitter ring is placed at the distance of 14 cm above the tank bottom. In numerical simulation, the splitter ring is created by blocking out the thirty-six appropriate computational cells. The computed free surfaces are shown in Fig. 10 at two different times; 2.95s(10.5T) and 4.37s(15.5T). Fig. 11 shows the computed velocity-vector field on vertical (x,y) and (z,y) planes. In the numerical results, only small wave motion can be observed. This indicates that surface responses have been suppressed by splitter ring.

Sloshing in the tank with vertical splitter ring. The vertical splitter ring is so placed that it is parallel to the front wall of the tank and 11.43 cm from the front wall. In numerical simulation, the splitter ring is created by blocking out the forty-six appropriate computational cells. The computed free surfaces are shown in Fig. 12 at three different times; 2.95s(10.5T), 3.24s(11.5T) and 4.37s(15.5T). Fig. 13 shows the computed velocity-vector field on vertical (x,y) and (z,y) planes. The computed free surfaces still oscillate, but the responses of free surface decrease largely in the direction perpendicular to the splitter ring. So, the free surface wave oscillates mainly in the direction parallel to the splitter ring.

Shallow Water Sloshing

Sloshing in the tank without baffles. The frequency of forced oscillation is chosen as 18.188rad/s ($2.04\omega_N$). The computed free surfaces are shown in Fig. 14(a) through Fig. 14(e) at five different times; 5.69s(16.5T), 6.04s(17.5T), 6.74(19.5T), 7.08s(20.5T) and 7.42s(21.5T). Fig. 14(f) shows the free surface response at 7.42s(21.5T) without higher-order initial perturbation. The computed velocity-vector field on vertical (x,y) and (z,y) planes are shown in Fig. 15 through 17. From the numerical results, the subharmonic responses also occur in shallow water depth. In addition, with large surface motion, some parts of tank bottom become uncovered.

Sloshing in the tank with horizontal splitter ring. The location of horizontal ring is the same as in the deep water case. The computed free surfaces are shown in Fig. 18 at four different times; 5.69s(16.5T), 6.04s(17.5T), 7.08s(20.5T) and 7.42s(21.5T). The computed velocity-vector field on vertical (x,y) and (z,y) planes are shown in Fig. 19 through Fig. 21. The surface responses are the same as with the no baffle case as long as the surface wave does not impact the splitter ring. The surface wave does not go beyond the splitter ring, even though the large surface wave impacts it.

Sloshing in the tank with vertical splitter ring. The location of vertical splitter ring is the same as in the deep water case. The computed free surfaces are shown in Fig. 22 at three different times; 5.69s(16.5T), 6.04s(17.5T), and 7.42s(21.5T). The computed velocity-vector field on vertical (x,y) and (z,y) planes are shown in Fig. 23. In this case, the part of splitter ring on the tank bottom has much influence on free surface motion. Therefore, the free surface response on the direction perpendicular to splitter ring is much less in comparison with deep water case.

CHAPTER 4: THE CONTROL OF LATERAL SLOSHING IN RECTANGULAR TANKS - THE EFFECTIVENESS OF FIXED BAFFLE AND MOVING BAFFLE WITH FEEDBACK CONTROL

Within the moving container, various types of sloshing waves can be created depending on the liquid depth and motion frequency. Sloshing is essentially a nonlinear phenomena. For large amplitude excitations, the liquid response can be rather violent. Baffles have been used to suppress and control sloshing. However, it may be desirable to explore the possibilities of using active moving baffles to control sloshing when the tank acceleration is large. The subject study was to investigate, numerically, the relative effectiveness of passive (fixed) baffles and active (moving) baffles for control of liquid sloshing. Both the deep water case and the shallow water case were studied. The study showed that active control of liquid sloshing, using moving baffles with feedback mechanisms, can be very effective in suppressing large amplitude sloshing.

Fig. 24 illustrates the concept of active baffle for the sloshing control. The baffle is set up to move in the opposite sense of certain neighboring flow to suppress the sloshing. In the deep water case, a vertical component of the baffle movement is provided while the horizontal baffle velocity is given for the shallow water case. Issues in numerical implementation included the appropriate set-up of boundary condition for moving baffles, choosing the appropriate control strategy, such as using suitable information to provide feedback and choosing appropriate feedback coefficient. Furthermore, noisy data needs to be smoothed out to provide feedback.

For the horizontal baffles in Fig. 24(a), the feedback was provided by V^*, the vertical velocity of the cell near the baffle. For the left baffle at (IOBS, JOBS, KOBS), the baffle's vertical velocity is

$$Vb = -\nu V^* \left[\frac{X(IOBS)-X(2)}{\frac{1}{2}\Delta x} + 1 \right] \qquad (66)$$

where ν is the coefficient of feedback. For the vertical baffle in Fig. 24(b), the feedback was controlled through U^*, the horizontal velocity of the cell near the baffle, the baffle's horizontal velocity is

$$Ub = - \nu U^* \left[\frac{Y(JOBS)-Y(2)}{\frac{1}{2}\Delta y} + 1 \right] \qquad (67)$$

Since the computed time history of the reference velocity exhibits noisy character of complicated three-dimensional nonlinear wave, cross-validation method is used to estimate the smoothing parameter. The treated reference velocity information was extrapolated to provide the feedback for active baffle. The coefficient of feedback ν is defined in Fig. 24. The case of $\nu=0$, represents fixed baffle.

A rectangular tank of 38.1 cm long, 38.1 cm wide, and 38.1 cm high is used for the numerical simulation. Water depth h=28.6 cm is chosen for deep water sloshing simulation. Two baffles, one on each side, are located near equilibrium free surface. Horizontal harmonic excitations x_0=3.048 cm and the excitation frequency ω equal to 1.01 times the first linear natural sloshing frequency. Fig. 25(a-b) shows the free surface plot at t=8.25T for the case when the baffles are fixed and the case when the baffles are active with feedback coefficient ν=0.3 after a first quarter period. The wave height time history on the left wall of each tank is shown in Fig. 26. The scale is given in inches, and the tank top at Sa=15 is indicated as a dashed line. The effect of active baffle is obvious wave height reduction of 50% was indicated. The shallow water computation is carried out at a 25% fill-depth for the same tank with same amplitude for a forcing frequency at 1.05 times the fundamental linear natural frequency. A single baffle is located at the center. Fig. 27(a-b) shows the free surface plot for fixed and active baffle (ν=0.5), respectively. Drastic reduction of wave height on the left wall (more than 60%), after the activation of moving baffle at t=T/4, can be seen from Fig. 28(a-b).

33

CHAPTER 5: THE IMPACT IN 1 g ENVIRONMENT BY BAFFLESINTRODUCTION

For the study of impact in 1 g environment, breaking wave against vertical wall seated on a structural foundation, was numerically simulated. Laitone's second order solitary wave theory is used as the initial conditions. When no foundation is present, the run up of a solitary wave on a vertical wall for a range of wave height/water depth ratio agrees well with the experimental data. The phenomena of wave breaking, such as wave steepening, overturning and formation of bores have been successfully simulated. Very high intensity shock pressure and wave impact force on the vertical wall are also obtained.

A mesh of 180 cells in the x-direction and 50 cells in the y direction was used to represent the computation region. The space increments $\delta x = 4cm$ and $\delta y = 2cm$ in x and y direction were used for all cases. Definition sketch is shown in Fig. 29. Water depth d is 35cm; initial wave crest is located at $x_0 = 240cm$; water density $\rho = 1g/cm^3$; gravity acceleration $g = 980cm/s^2$; kinematic viscosity $\nu = 0.01002cm^2/s$; iteration convergence criterion $\epsilon = 0.001$.

First, solitary wave propagating toward a vertical wall without formation is computed. The wave run-up ratio R/d is compared with the experimental data of Street & Camfield (1988) [40] in Fig. 30. Clearly, the numerical results are in excellent agreement with experiments.

The computations have been carried out for several configurations of foundations. The berm of the foundation is 160cm and slope is 1:2. The relative water depth at the berm of foundations d_1/d are 0.71, 0.60, 0.49, 0.37 and 0.2. Wave height H is 18.9cm(H/d=0.54). Flow field for shallow foundation ($d_1/d=0.71$) is shown in Fig. 31. In this case, the solitary wave is fully reflected by the wall without breaking. Fig. 32 is the flow field for one of middle size foundation ($d_1/d=0.37$). As a wave propagates on the berm, water particle velocity at the wave crest increases and wave front becomes steeper. It eventually becomes unstable and breaks when water

particle velocity at the wave crest exceeds the wave speed (theoretical value is 230cm/s). Flow field for fairly high foundation ($d_1/d=0.2$) is shown in Fig. 33. It shows clearly the plunging breaker in front of the wall. After breaking, the bores are formed with high speed. The shock pressure occurs when the bores hit the wall. Fig. 34 and 35 are the evolution of waves for $d_1/d=0.37$ and 0.2. The time history of pressure at still water level on the wall is shown in Fig. 36. From Table 5, it is easier to find the maximum shock pressure and impulse force. Shock pressure on the wall, in the case of middle size foundation, is smaller than that in the case of high foundation.

TABLE 5

MAXIMUM WAVE PRESSURE AND FORCE VALUES (H/d=0.54)

d_1/d	1.0	0.71	0.60	0.49	0.37	0.2
$P_{max}/\rho g H$	1.48	1.54	1.73	1.99	2.57	3.31
$F_{max}/\rho g H d$	2.14	2.75	3.15	4.01	5.36	15.51

Fig. 37 to Fig. 39 show the computational results for wave height H=27.3cm(H/d=0.78) which is the limiting wave height from solitary wave theory. Again, it shows the plunging breaker in front of wall. The large jet is ejected forward from the tip of the wave. Very high shock pressure occurs when bore front hits the wall. The shock pressure $P_{max}/\rho g H$ is 5.32 and impulse force $F_{max}/\rho g H d$ is 8.70.

CHAPTER 6: SWIRLING IN CYLINDRICAL TANK AND ITS CONTROL

It is well known that lateral excitation, near the lowest liquid resonant frequency, causes an interesting type of liquid instability to take place in the form of swirl motion superimposed on the normal sloshing motion. As described in Reference 1, "*The motion is even more complicated as a ty. 'beating' also seems to exist; the first antisymmetric liquid-sloshing mot. first begins to transform itself into a rotational motion increasing in angular velocity in, say, the counterclockwise direction, which reaches a maximum and then decreases essentially to zero and then reverses and increases in angular velocity in the clockwise direction, and so on, alternately. The frequency of rotation is less than that of the surface wave motion and, therefore, the liquid appears to undergo a vertical up-and-down motion as it rotates about the tank axis; the rotational frequency about this up-and-down axis is about the same as that of the wave motion.*" As part of the algorithm testing, numerical experiments were carried out to examine this phenomena of flow instability.

An upright cylindrical tank of diameter d=19.558 cm and water depth h=d, is used for the numerical simulation. The dimensions of the cylindrical tank for numerical simulation are the same as the experimental tank in Ref. 41. With this diameter and water depth, the first antisymmetrical natural frequency ω_H=13.574 rad/s($\omega^2 d/g$=3.68). The amplitude of the forced-lateral oscillation is x_0=0.3363 cm(x_G/d=0.0172). The frequency of forced oscillation is ω=13.979 rad/s($\omega^2 d/g$=3.90). The parameters of forced-oscillation are selected in the swirl region predicted by laboratory experiment (Fig. 40), so that the swirl motion of liquid can be studied by numerical simulation.

The liquid is initially at rest. Under a sinusoidal excitation, the time history of wave height, pressure and force components are shown in Fig. 41. The location for wave height record S_b is 4.191 cm from the left tank wall.

The location for pressure record P_b is 4.191 cm from the left tank wall and 18.161 cm from the tank bottom. F_{hx} is force component in the direction of excitation and F_{hz} is force component perpendicular to the paper plane (transverse force). *"Beating"* is apparent. Fig. 42 shows computed free surface within one period of forced oscillation T; the time interval is 0.125 T. The computed velocity-vector field on horizontal (x,z) plane is shown in Fig. 43, in which section J=8 and J=9 are 18.161 cm and 20.955 cm from the tank bottom, respectively. The computed velocity-vector field on the vertical (x,y) and (z,y) plane is shown in Fig. 44. From the numerical results, swirl motion of free surface can be observed, in agreement with experiment results of Ref. 41. The period of swirling motion is the same as the period of forced oscillation. The horizontal velocity-vector field shows the swirling direction. One important characteristic of liquid swirl motion is that large transverse force component exists. This may be used to determine whether or not the swirl motion of free surface occurs.

Systematic numerical experiments were carried out to compare numerical predicted wave amplitude with laboratory test results of Ref. 41. Four levels of maximum amplitudes of oscillation, $x_0/d=0.0056$, 0.0115, 0.0172 and 0.0227, were used. In the numerical model, the number of cells in x, y and z direction are 7, 12 and 7 respectively. The position for wave height record is 1.397 cm from the left tank wall. Liquid amplitude responses in the first antisymmetric slosh mode are shown as a function of excitation frequency, for several constant values of excitation amplitude x_0/d in Fig. 40. For each excitation, the numerical data is obtained by averaging successively 10 wave heights after steady-state solution is approached. The numerical results agree well with experimental data when excitation frequency is less than ω_{II}. When excitation frequency is larger than ω_{II}, the numerical results predict a slightly larger result, but it still shows good agreement with experimental results. In the shaded region, the obviously swirl motion occurs as predicted by numerical simulation.

EFFECTS OF BAFFLES IN THE LATERAL SLOSHING OF A CYLINDRICAL TANK

The introduction of baffle changes the characters of liquid sloshing in many complicated ways. To evaluate baffle effect, four typical baffle arrangements were each added to the baseline case described earlier (Figs. 41-44) and tested numerically. Shown in Fig. 45, is the arrangement of these baffle types, namely,

(a) Short vertical splitter plates in transverse direction.

(b) Long vertical splitter plates in transverse direction.

(c) Short vertical splitter plates in the direction of excitation.

(d) Horizontal ring at undisturbed free surface.

Short Vertical Splitter Plates in Transverse Direction

The arrangement is shown in Fig. 45(a). The time history of wave height, pressure and force components is shown in Fig. 46. Fig. 47 shows the computed free surface within one period of forced oscillation. The computed velocity-vector field on horizontal (x,z) plane is shown in Fig. 48. The computed velocity-vector field on vertical (x,y) and (z,y) plane is shown in Fig. 49. Swirl motion of free surfaces are observed in this configuration and there still exists a large transverse force shown in Fig. 48(d). However, the amplitude of free surface wave is reduced due to the effect of splitter plates.

Long Vertical Splitter Plates in Transverse Direction

The arrangement is shown in Fig. 45(b). The time history of wave height, pressure and force components is shown in Fig. 50. Fig. 51 shows the computed free surface within one period of forced oscillation. The computed velocity-vector field on horizontal (x,z) plane is shown in Fig. 52. The computed velocity-vector field on the vertical (x,y) and (z,y) plane is shown in Fig. 53. Swirl motion of free surface is suppressed in this configuration. Only small surface wave can be observed. Small transverse force shown in Fig. 50(d) indicates no-swirl motion.

Short Vertical Splitter Plates in the Direction of Excitation

The baffle type is shown in Fig. 45(c). The time history of wave height, pressure and force components is shown in Fig. 54. Fig. 55 shows the computed free surface within one period of forced oscillation. The computed velocity-vector field on horizontal (x,z) plane are shown in Fig. 56. The computed velocity-vector field on the vertical (x,y) and (z,y) plane is shown in Fig. 57. Although swirl motion of free surface is easily suppressed in this configuration, very large wave motion in the direction of excitation is formed. Only small transverse force is shown in Fig. 54(d).

Horizontal Ring at Undisturbed Free Surface

The ring is located as shown in Fig. 45(d). The time history of height, pressure and force components is shown in Fig. 58. Fig. 59 shows the computed free surface within one period of forced oscillation. The computed velocity-vector field on horizontal (x,z) plane is shown in Fig. 60. The computed velocity-vector field on the vertical (x,y) and (z,y) plane is shown in Fig. 61. Swirl motion of free surface is not obvious in this configuration. But, one can conclude that there still exists swirl motion from large transverse force, as shown in Fig. 58.

Swirling and Drainage

Various combinations of swirling and drainage were computed. The swirling intensification and the air-entrainment induced during the liquid drainage through the tank bottom were noted. Surface and surface contour plots at various rates of drainage were shown in Fig. 62. A preliminary laboratory experiment was carried out which revealed rather complicated instability processes involved in the drainage. To include such processes would require further-refined numerical and laboratory modeling. Therefore, the topic was only briefly mentioned in this report.

CHAPTER 7:   CONCLUSION AND FUTURE WORK

Fuel sloshing in space environment is a problem of technical significance. The low gravity environment, the rapid maneuvering of the spacecraft, the flexible container, impact loads, surface tension, flow-induced sloshing (such as drainage) and the sloshing control and suppression offer many areas of possibility of advancement. Some progresses in sloshing simultion and control were reported in the present report. Many problems remain, relating to:

- Low gravity environment

- Surface tension

- Sub-grid phenomena

- Small scale flow physics and flow instability

- Impact on flexible structure

- Improving surface representation

- Experimental verification

More studies are required to address these issues.

REFERENCES

1. H. N. Abramson (ed.), "The Dynamic Behavior of Liquids in Moving Containers," NASA SP-106, 1966.

2. H. N. Abramson, "Dynamic Behavior of Liquids in Moving Containers," Appl. Mech. Revs., Vol. 16, No. 7, July 1963, pp. 501-506.

3. H. N. Abramson, "Some Current Aspects of the Dynamic Behavior of Liquids in Rocket Propellant Tanks," Applied Mechanics Surveys, Spartan Books, Inc., Washington, D.C., 1966.

4. M. N. Sloane, "The Dynamics of the Sloshing Phenomenon (a Literature Survey)," Rept. GM-60-5111-5, Space Technology Laboratories, Inc., April 1960.

5. R. M. Cooper, "Dynamics of Liquids in Moving Containers," ARS J., Vol. 30, Aug. 1960, pp. 725-729.

6. R. L. Bass, "Dynamic Slosh Induced Loads on Liquid Cargo Tank Bulkheads," Technical and Research Report R-19, The Society of Naval Architects and Marine Engineers, Aug. 1975.

7. J. W. Miles, "Ring Damping of Free Surface Oscillations in a Circular Tank," J. Appl. Mech., Vol. 25, No. 2, June 1958, pp. 274-276.

8. J. W. Miles, "Note on the Damping of Free-Surface Oscillations Due to Drainage," Rept. No. TDR-930 (2270-20) TN-1, Aerospace Corp., El Segundo, California, Sept. 1961.

9. J. W. Miles, "Nonlinear Surface Waves in Closed Basins", Journal of Fluid Mechanics, Vol. 75, Part 3, 1976, pp. 419-448.

10. C. C. Mei and L. F. Liu, "The Damping of Surface Gravity Waves in a Bounded Liquid", Journal of Fluid Mechanics, Vol. 59, Part 2, 1973, pp. 239-256.

11. K. M. Case and W. C. Parkinson, "Damping of Surface Waves in an Incompressible Liquid," J. Fluid Mech., Vol. 2, March 1957, pp. 172-184.

12. P. A. Cox, E. B. Bowles and R. L. Bass, "Evaluation of Liquid Dynamic Loads in Slack LNG Cargo Tanks", Southwest Research Institute Report No. SR-1251, May 1979.

13. D. C. Ma and T. C. Su (Co-editor), "Fluid-Structure Vibration and Liquid Sloshing", PVP-Vol. 128, The American Society of Mechanical Engineers, June 1987, pp. 112.

14. V. W. Nee, R. B. Samant and Z. Huang, "Viscous Effects on the Fluid-Structure Interaction during Earthquake", Advancements in Aerodynamics, Fluid Mechanics and Hydraulics, ASCE, 1986, pp. 617-628.

15. M. Wang and T. Hung, "A Nonlinear hydrodynamic Analysis on Pine Flat Dam", Advancements in Aerodynamics, Fluid Mechanics and Hydraulics, ASCE, 1986, pp. 629-636.

16. E. W. Graham and A. M. Rodriquez, "The Characteristics of Fuel Motion which Affect Airplane Dynamics," J. Appl. Mech., Vol. 19, No. 3, Sept. 195 pp. 381-388.

17. W. H. Chu, J. F. Dalzell and J. E. Modisette, "Theoretical and Experimental Study of Ship-Roll Stabilization Tanks," JSR, Sept. 1968, pp. 168-181.

18. O. M. Faltinsen, "A Nonlinear Theory of Sloshing in Rectangular Tanks," JSR, Dec. 1974, pp. 224-241.

19. J. H. G. Verhagen and L. Van Wijngaarden, "Nonlinear Oscillations of Fluid in a Container," Jour. of Fluid Mechanics, Vol. 22, Part 4, 1965.

20. O. M. Faltinsen, "A Numerical Nonlinear Method of Sloshing in Tanks with Two-Dimensional Flow," Journal of Ship Research, Vol. 22, No. 3, Sept. 1978, pp. 193-2-2.

21. M. Ikegawa, "Finite Element Analysis in Fluid Motion in a Container," Finite Element Methods in Flow Problems, UAH Press, Huntsville, 1974, pp. 737-738.

22. T. Nakayama and K. Washizu, "The Boundary Element Method Applied to the Analysis of Two-Dimensional Non-linear Sloshing Problems", International Journal for Numerical Method in Engineering, Vol. 17, 1981, pp. 1631-1646.

23. C. W. Hirt, B. D. Nichols and N. C. Romero, "SOLA-A Numerical Solution Algorithm for Transient Fluid Flows", Los Alamos Scientific Laboratory Report LA-5852, April 1975.

24. J. Navickas, J. C. Peck, R. L. Bass III, E. B. Bowles, N. Yoshimura and S. Endo, "Sloshing of Fluids at High-Fill Levels in Closed Tanks", presented at the Winter Annual Meeting of the American Society of Mechanical Engineers, Washington, D.C., November 15-20, 1981.

25. N. E. Mikelis, J. K. Miller and K. V. Taylor, "Sloshing in Partially Filled Liquid Tanks and its Effect on Ship Motions: Numerical Simulations and Experimental Verification", Proceedings, The Royal Institution of Naval Architects, Spring Meeting, 1984.

26. C. W. Hirt and B. D. Nichols, "Volume of Fluid (VOF) Method for the Dynamics of Free Boundaries", Journal of Computational Physics, Vol. 39, pp. 201-225, 1981.

27. T. C. Su, Y. K. Lou, J. E. Flipse and T. Bridges, "A Numerical Analysis of Large Amplitude Liquid Sloshing in Baffled Containers", Report No. MA-RD-940-82046, U.S. Department of Transportation, Maritime Administration, 290 pages, March 1982.

28. T. C. Su, Y. K. Lou, J. E. Flipse and T. Bridges, "A Nonlinear Analysis of Liquid Sloshing in Rigid Containers," Report No. DOT/RSPA/DMA-50/82/1, Office of University Research, U.S. Department of Transportation, 1982.

29. T. C. Su and S. Y. Kang, "Analysis of Liquid Impact on Moving Containers, "Proceedings of the 12th Southeastern Conference on Theoretical and Applied Mechanics, 1984, Vol. 1, pp. 474-479. (Also appeared in Development in Applied Mechanics, Vol. 12).

30. T. C. Su and S. Y. Kang, "Numerical Simulation of Liquid Sloshing," Engineering Mechanics in Civil Engineering, Ed. A. P. Boresi and K. P. Chong, American Society of Civil Engineers, Volume 2, 1984, pp. 1069-1072.

31. S. Y. Kang, "Analysis of Liquid Impact on Moving Containers", M.S.-Thesis, Florida Atlantic University, August 1984.

32. T. C. Su and S. Y. Kang, "Analysis and Testing of the Large Amplitude Liquid Sloshing in Rectangular Containers," Seismic Engineering for Piping Systems, Tanks and Power Plant Equipment, PVP-Vol. 108, ASME, 1986, pp. 149-154.

33. T. C. Su, "Numerical Study on the Three Dimensional Liquid Sloshing and Liquid Impact," Presented to the Post-SMIRT Seminar on IMPACT, August 26-27, 1987, Ecole Polytechnique Federale de Lausanne Switzerland (Invited Paper).

34. T. C. Su and Y. X. Wang, "On Three Dimensional Liquid Sloshing", to be presented to the ASME Pressure Vessel and Piping Conference, Honolulu, Hawaii, July, 1989.

35. Y. X. Wang, "Numerical Simulation of Sloshing in Arbitrary Containers", Ph.D. Dissertation Submitting to Dalian University of Technology, China (Thesis Advisor: T. C. Su).

36. R. J. Hung, Y. D. Tsao and B. B. Hong, "Effect of Surface Tension on the Dynamical Behavior of Bubble in Rotating Fluids under Low Gravity Environment", Proceedings, First National Fluid Dynamics Congress, July, 1988, pp. 1399-1409.

37. J. Navickas, "Space-Based System Disturbances Caused by On-Board Fluid Motion During Systems Maneuvers", Proceedings, First National Fluid Dynamics Congress, July, 1988, pp. 1558-1562.

38. P. Y. Liang, "A Numerical Method for Calculation of Surface Tension Flows in Arbitrary Grids", Proceedings, First National Fluid Dynamics Congress, July, 1988, pp. 1629-1638.

39. M. Faraday, "On the Forms and States Assumed by Fluids in Contact with Vibrating Elastic Surfaces", Phil. Trans. Roy. Soc. (London), Vol. 121, 1831, pp. 319-340.

40. R. L. Street and F. E. Camfield, "Observations and Experiments on Solitary Wave Deformation", Proceedings of 10th International Conference on Coastal Engineering, 1966, Chapter 19, pp. 284-301.

41. H. N. Abramson, W. H. Chu, and D. D. Kana, "Some Studies of Nonlinear Lateral Sloshing in Rigid Containers", Journal of Applied Mechanics, Vol. 33, No. 4, December 1966, pp. 777-784.
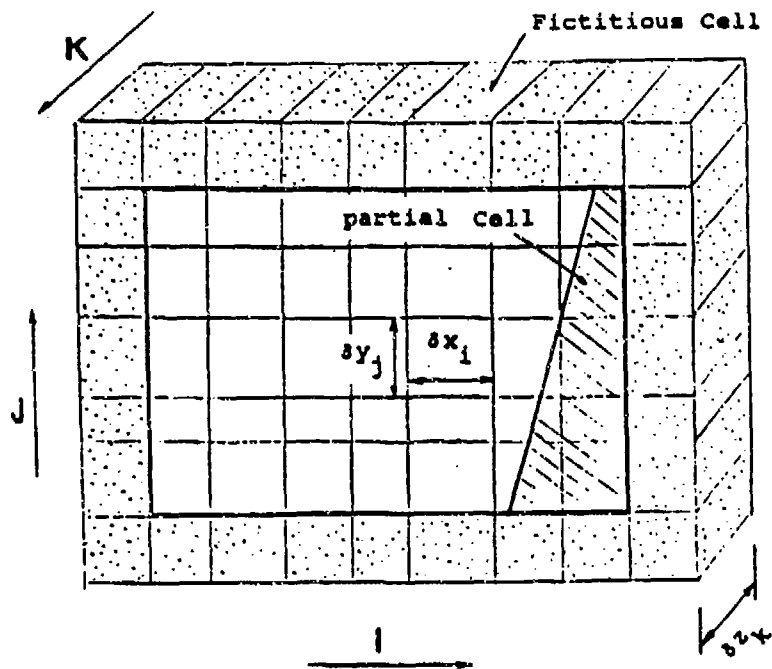
Fig. 1. General mesh setup
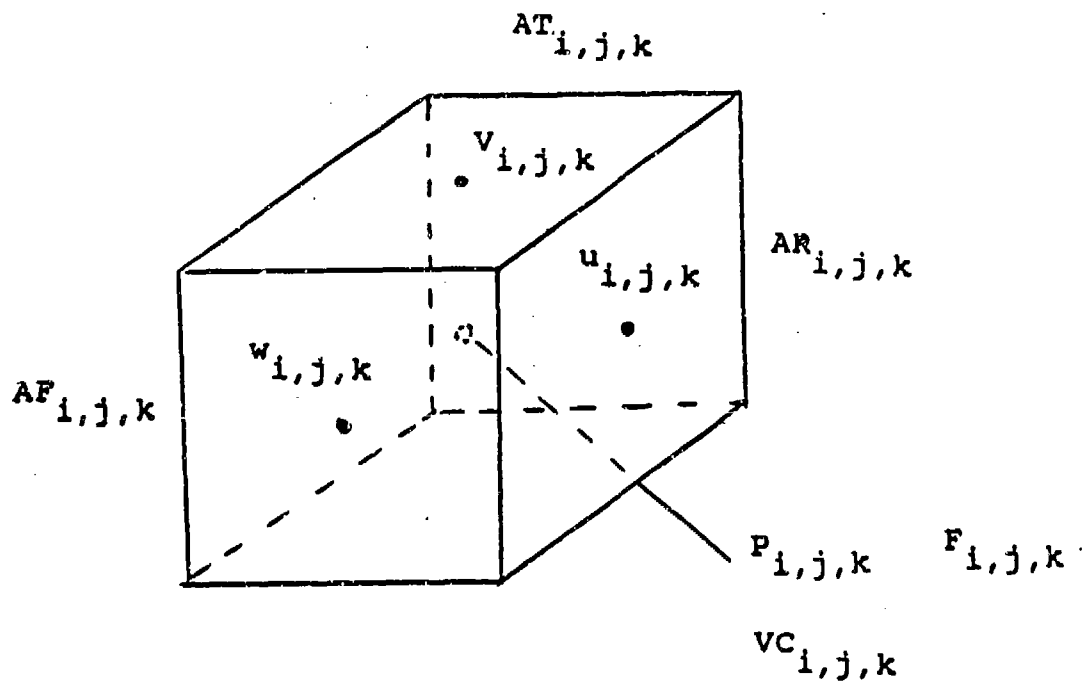
Fig. 2. Location of dependent variables

44
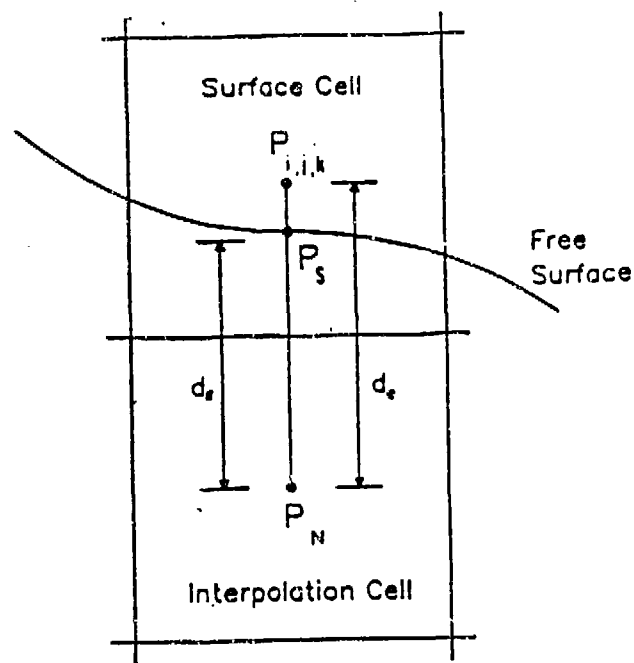
Fig. 3 Pressure Interpolation for Free Surface

(a)

(b)
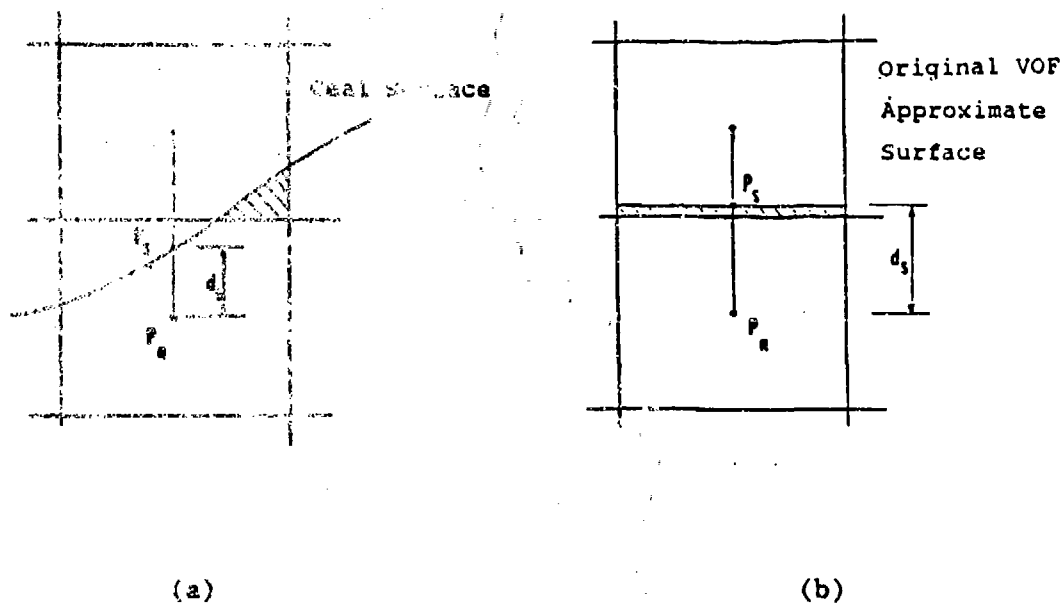
Fig. 4. Distance ds for different free surface approximation

45
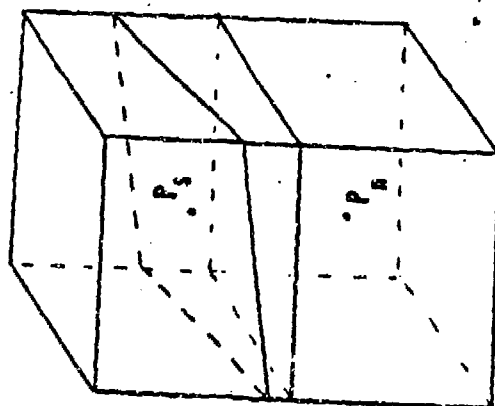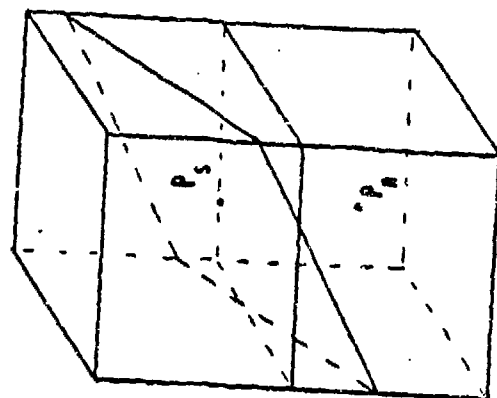
Fig. 5. Surface position in free surface cell

(a)

(b)

46
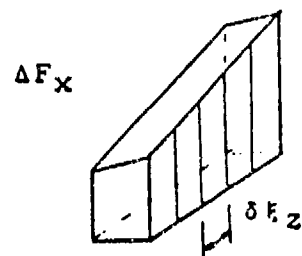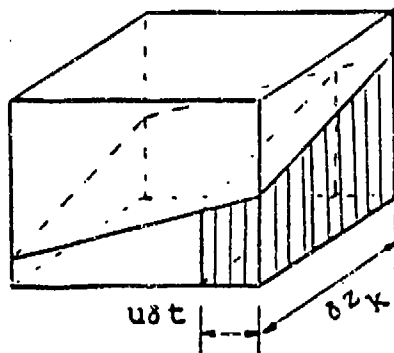
(a) The flux in x direction
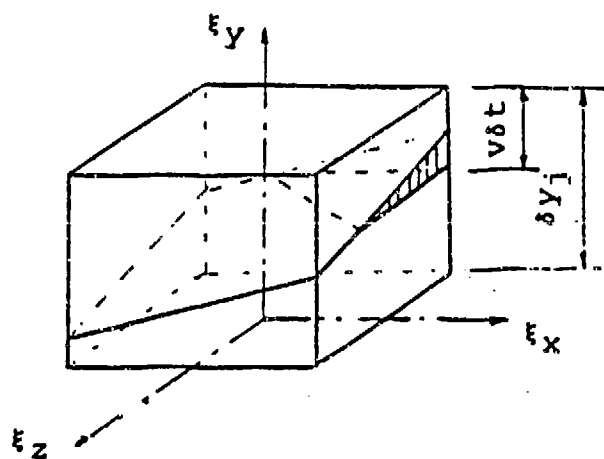
(b) The flux in y direction
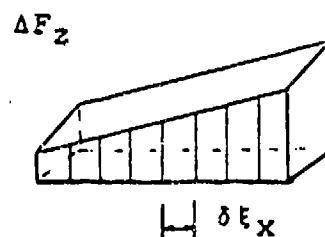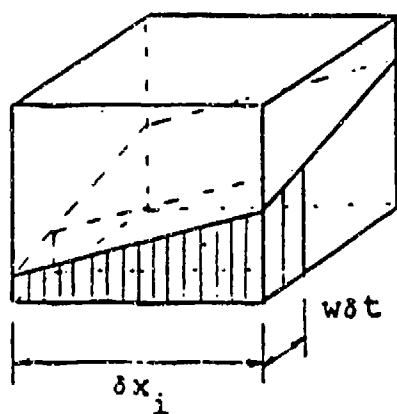
(c) The Flux in z Direction

Fig. 6. Examples of the advection of F in the case of NF-3
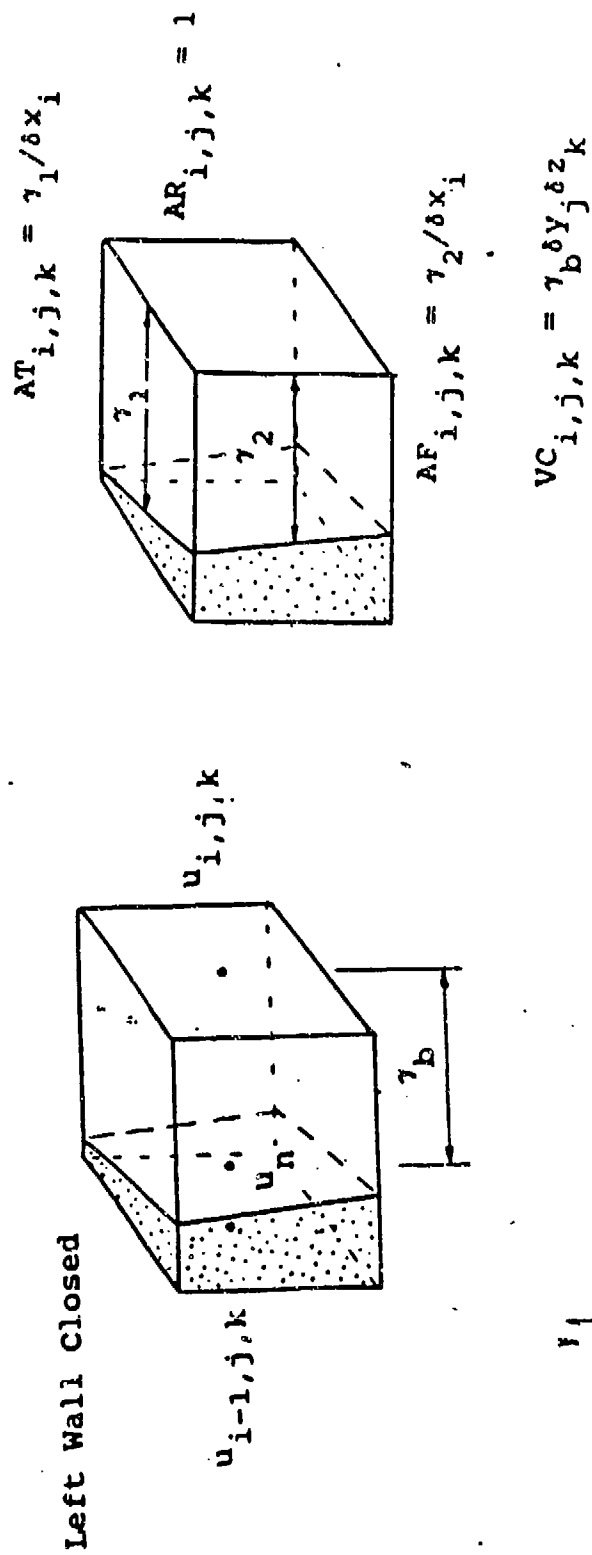
Fig. 7. Examples of the arbitrary boundary in the case of NFB=2
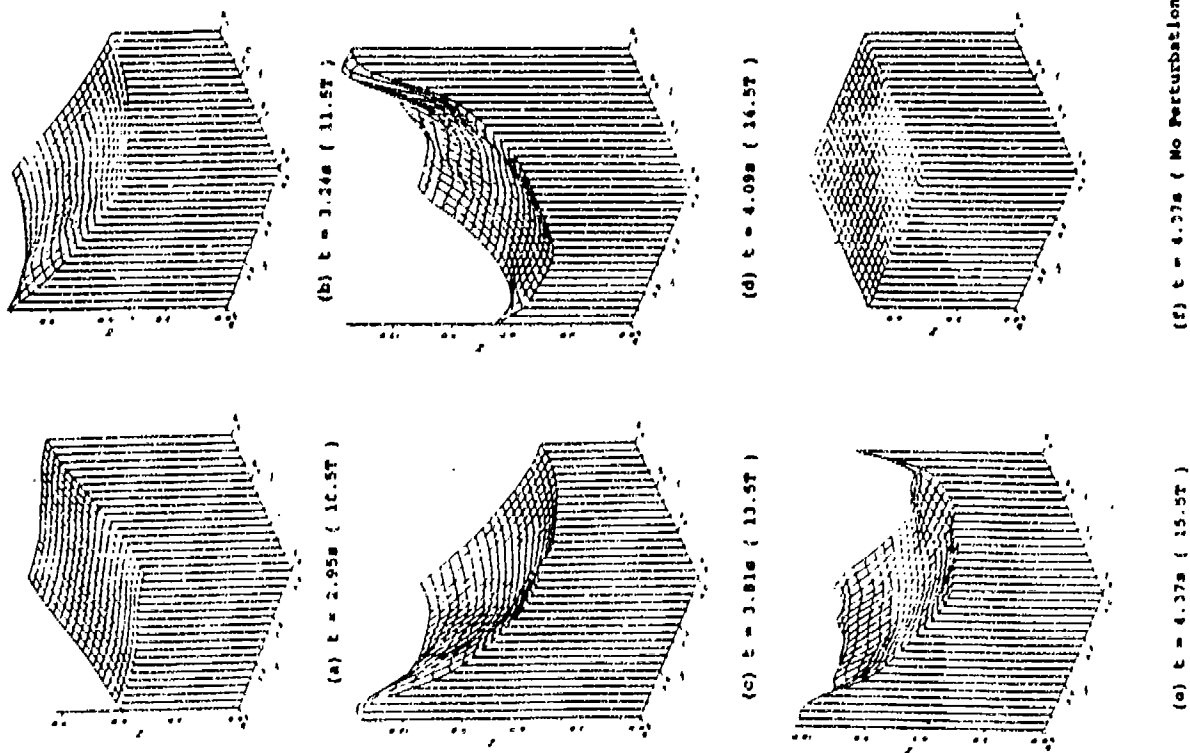
$AT_{i,j,k} = \gamma_1/\delta x_i$

$AR_{i,j,k} = 1$

$AF_{i,j,k} = \gamma_2/\delta x_i$

$VC_{i,j,k} = \gamma_b \delta y_j \delta z_k$

(b)

$u_{i,j,k}$

γ_2

γ_2

Left Wall Closed

γ_b

u_n

$u_{i-1,j,k}$

(a)

48

Fig. 9. Velocity plot for deep water sloshing under vertical excitation (no baffles)

Fig. 8. Surface plot for deep water sloshing under vertical excitation (no baffles)

49
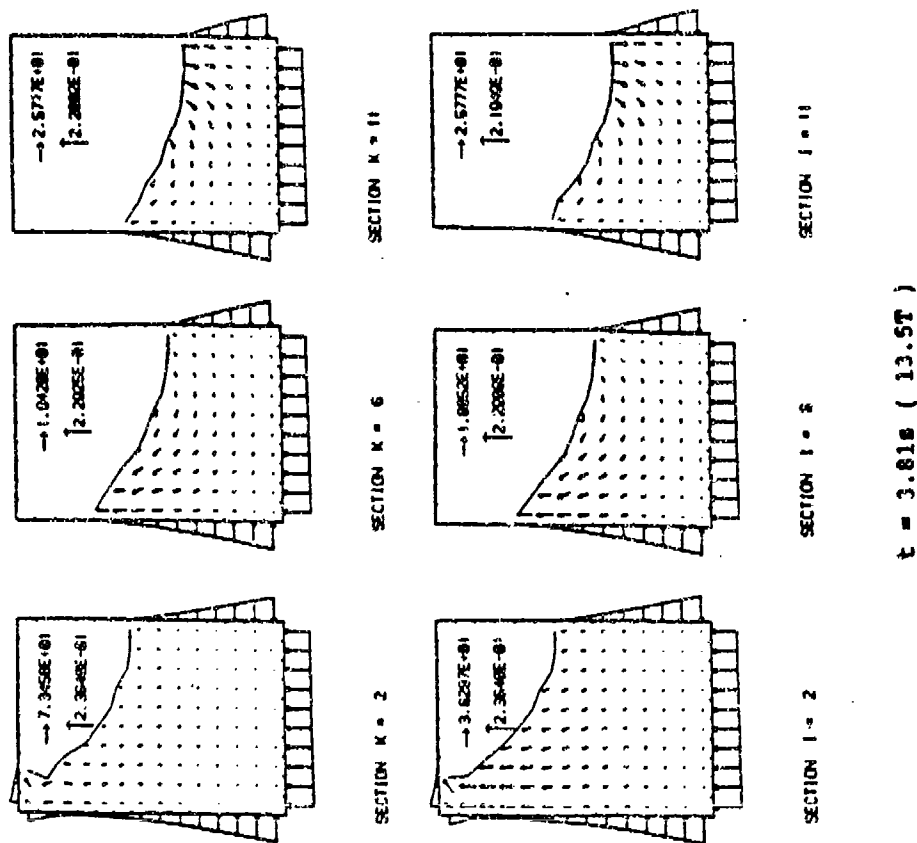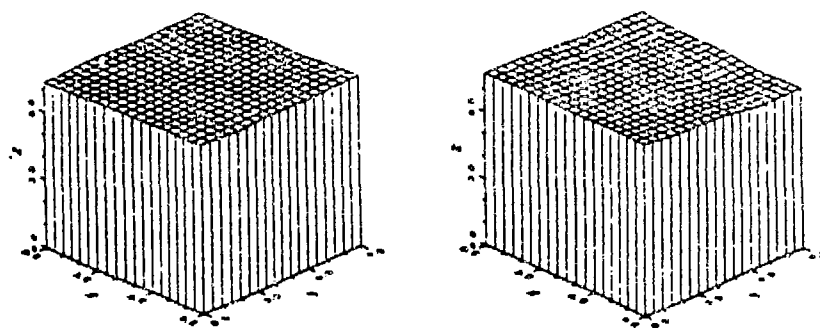
(a) t = 2.95s (10.5T)   (b) t = 4.37s (15.5T)

Fig. 10. Surface plot for deep water sloshing under vertical excitation
          (horizontal baffles)

SECTION K = 2   SECTION K = 3   SECTION K = 6   SECTION K = 10   SECTION K = 11

SECTION I = 2   SECTION I = 3   SECTION I = 6   SECTION I = 10   SECTION I = 11

t = 4.37s (15.5T)   TIME 4.3728E+00
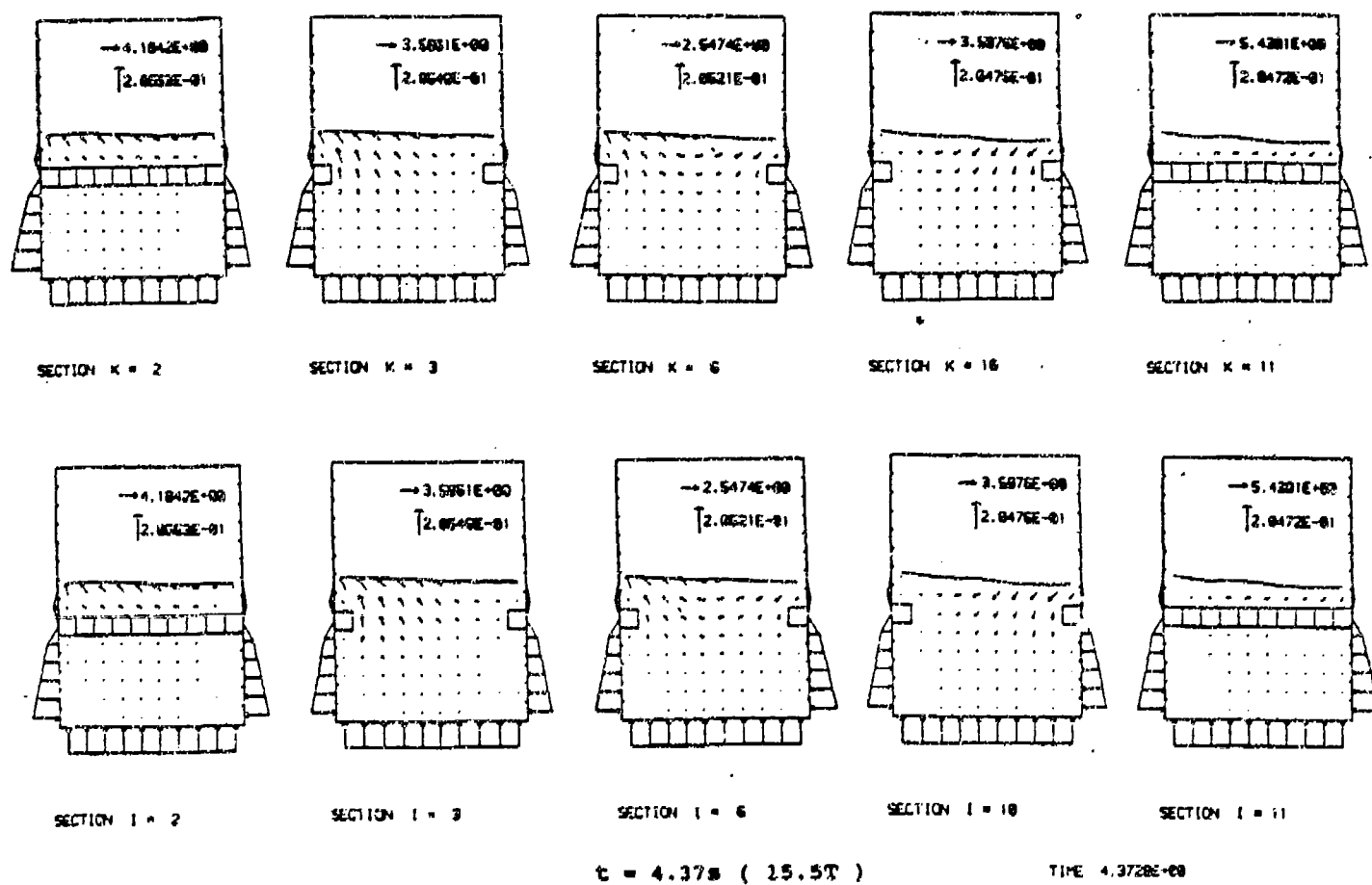
Fig. 11. Velocity plot for deep water sloshing under vertical excitation
          (horizontal baffles)
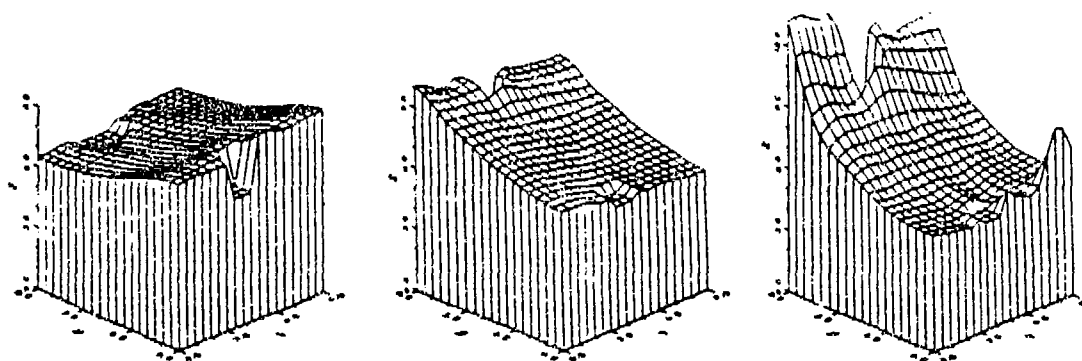
(a) t = 3.95s (10.5T)   (b) t = 3.24s (11.5T)   (c) t = 4.37s (15.5T)

Fig. 12.   Surface plot for problem of deep water sloshing under vertical
excitation (vertical baffles)

SECTION K = 2   SECTION K = 5   SECTION K = 6   SECTION K = 7   SECTION K = 11

SECTION I = 2   SECTION I = 3   SECTION I = 6   SECTION I = 10   SECTION I = 11

TIME 4.3744E+00

t = 4.37s (15.5T)
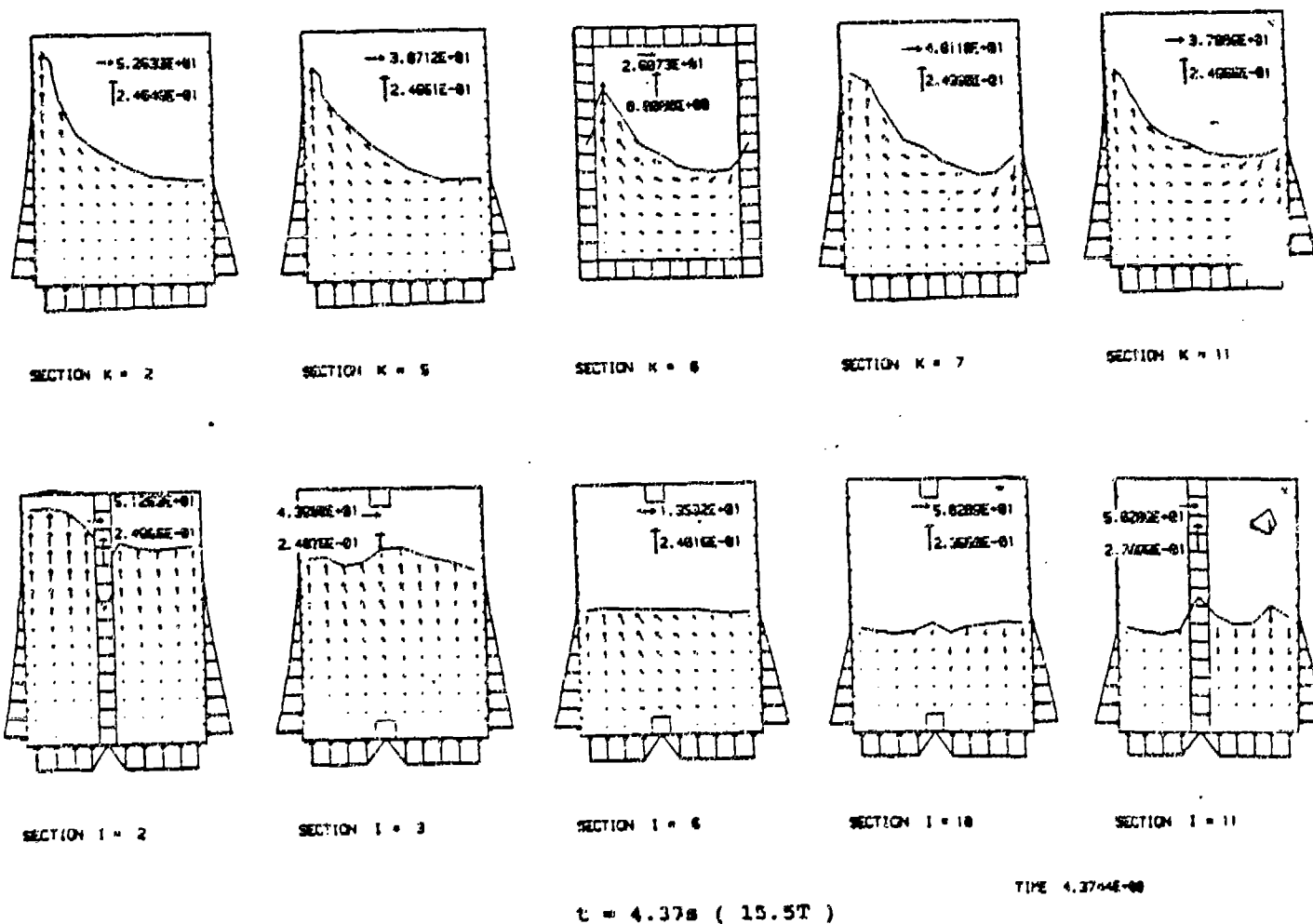
Fig. 13.   Velocity plot for problem of deep water sloshing under vertical
excitation (vertical baffles)
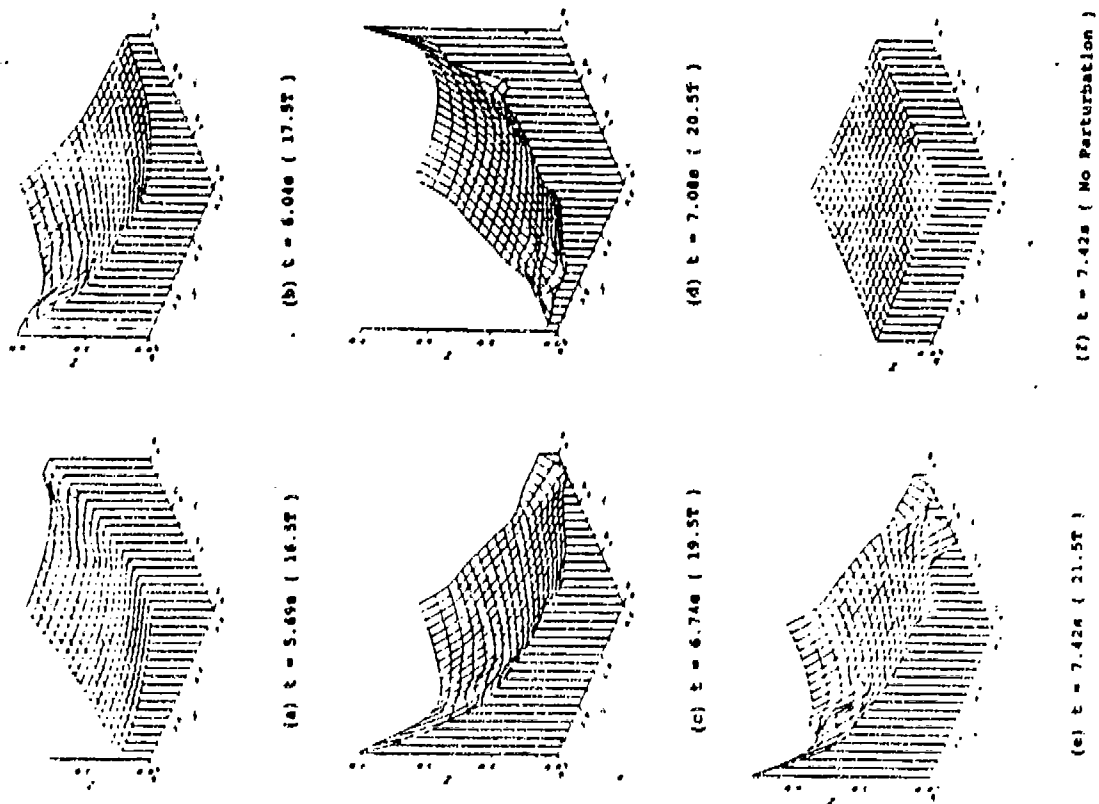
51
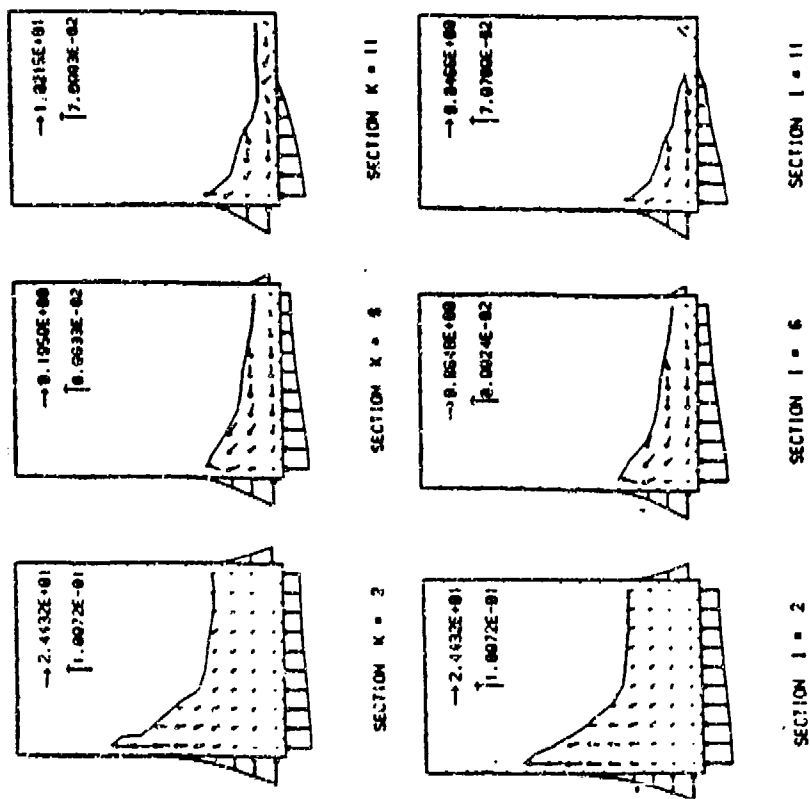
Fig. 15. Velocity plot for shallow water sloshing under vertical excitation (no baffles)

Fig. 14. Surface piot for shallow water sloshing under vertical excitation (no baffles)

52

SECTION K = 11 SECTION K = 8 SECTION K = 2

SECTION I = 11 SECTION I = 8 SECTION I = 2

t = 7.42s (21.5T)

Fig. 17.   Velocity plot for shallow water sloshing
under vertical excitation (no baffles)

SECTION K = 11 SECTION K = 8 SECTION K = 2

SECTION I = 11 SECTION I = 8 SECTION I = 2

t = 7.08s (20.5T)
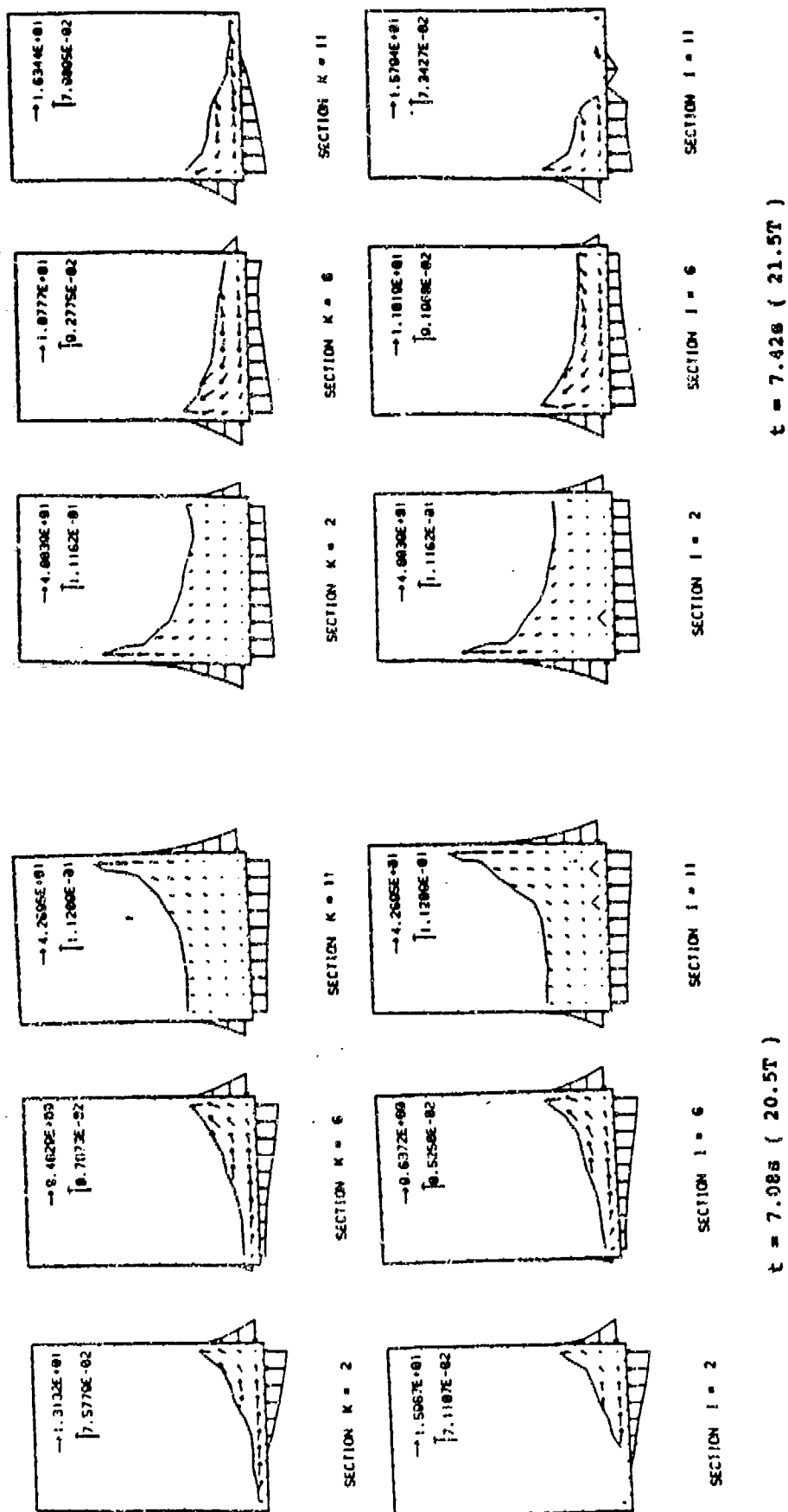
Fig. 16.   Velocity plot for shallow water sloshing
under vertical excitation (no baffles)

53

(a) t = 5.69s (16.5T)   (b) t = 6.04s (17.5T)

(c) t = 7.08s (20.5T)   (d) t = 7.43s (21.5T)
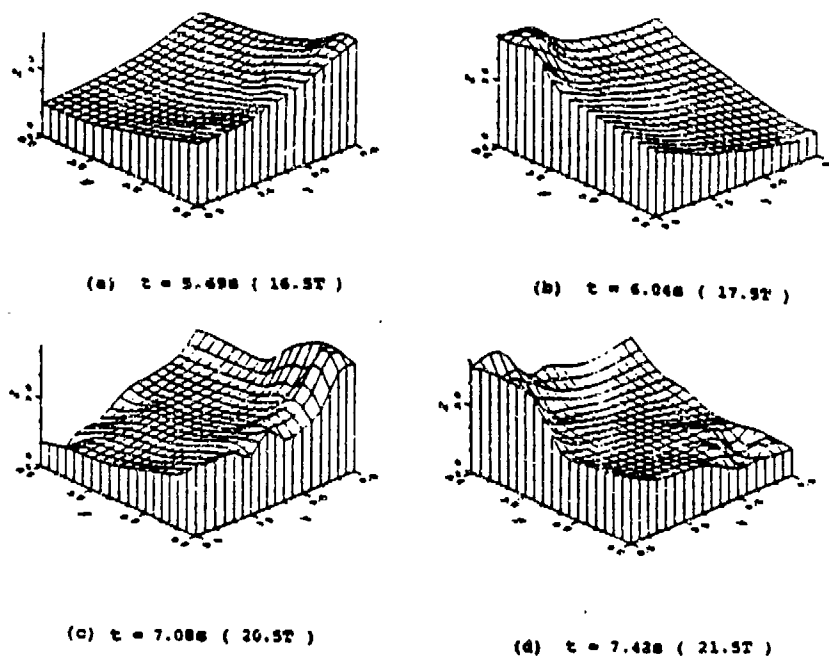
Fig. 18.   Surface plot for shallow water sloshing under vertical excitation
(horizontal baffles)

t = 5.69s (16.5T)
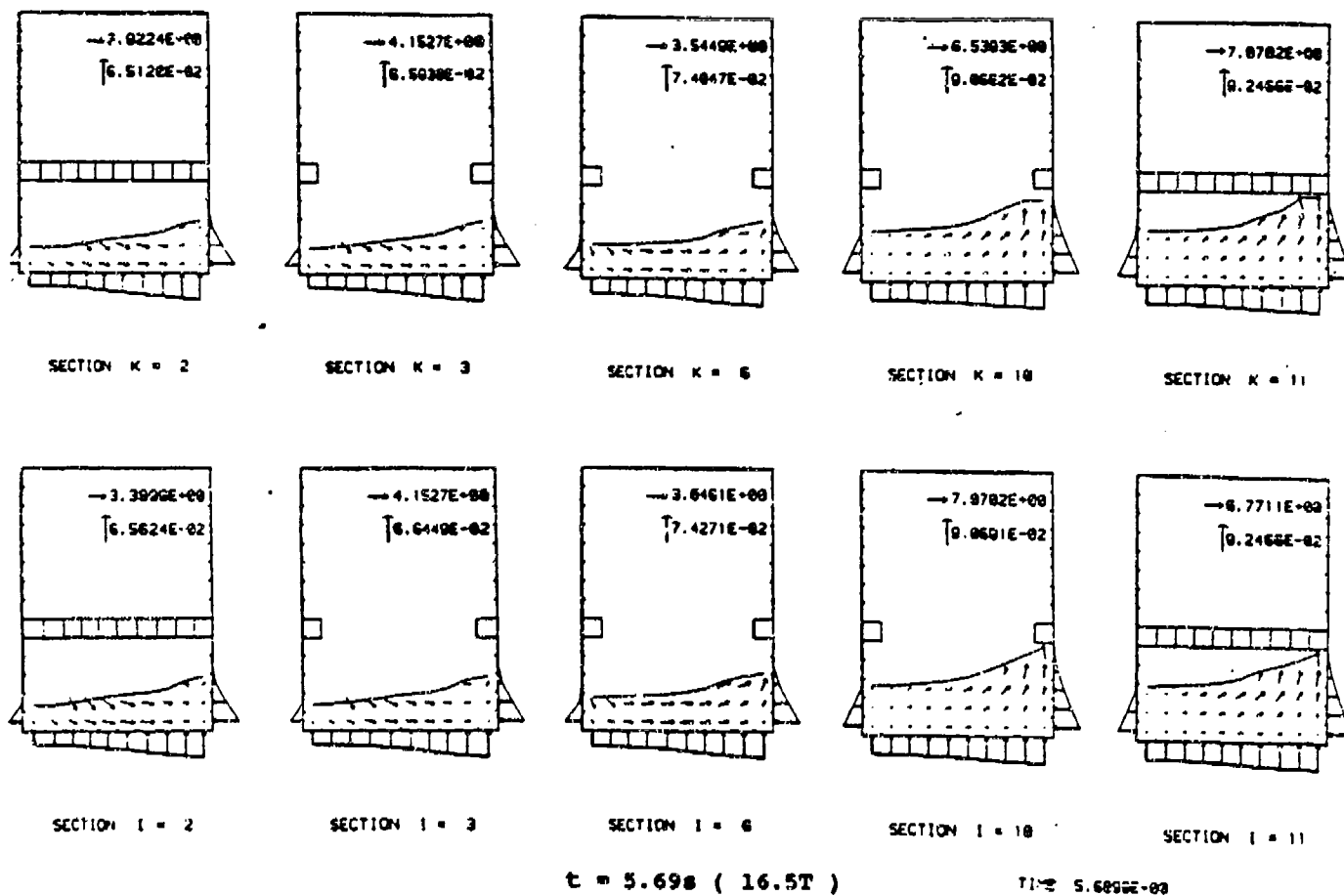
Fig. 19.   Velocity plot for shallow water sloshing under vertical excitation
(horizontal baffles)

54
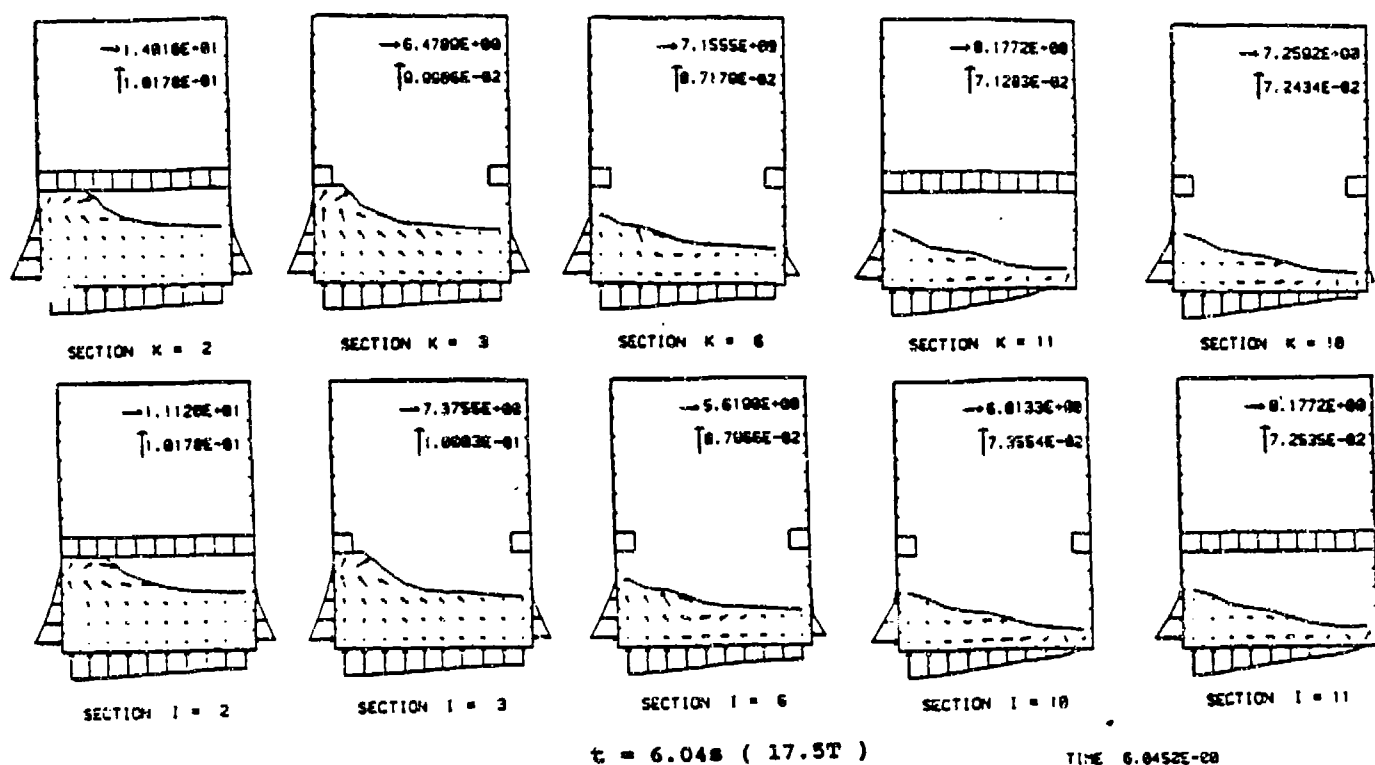
Fig. 20. Velocity plot for shallow water sloshing under vertical excitation (horizontal baffles)
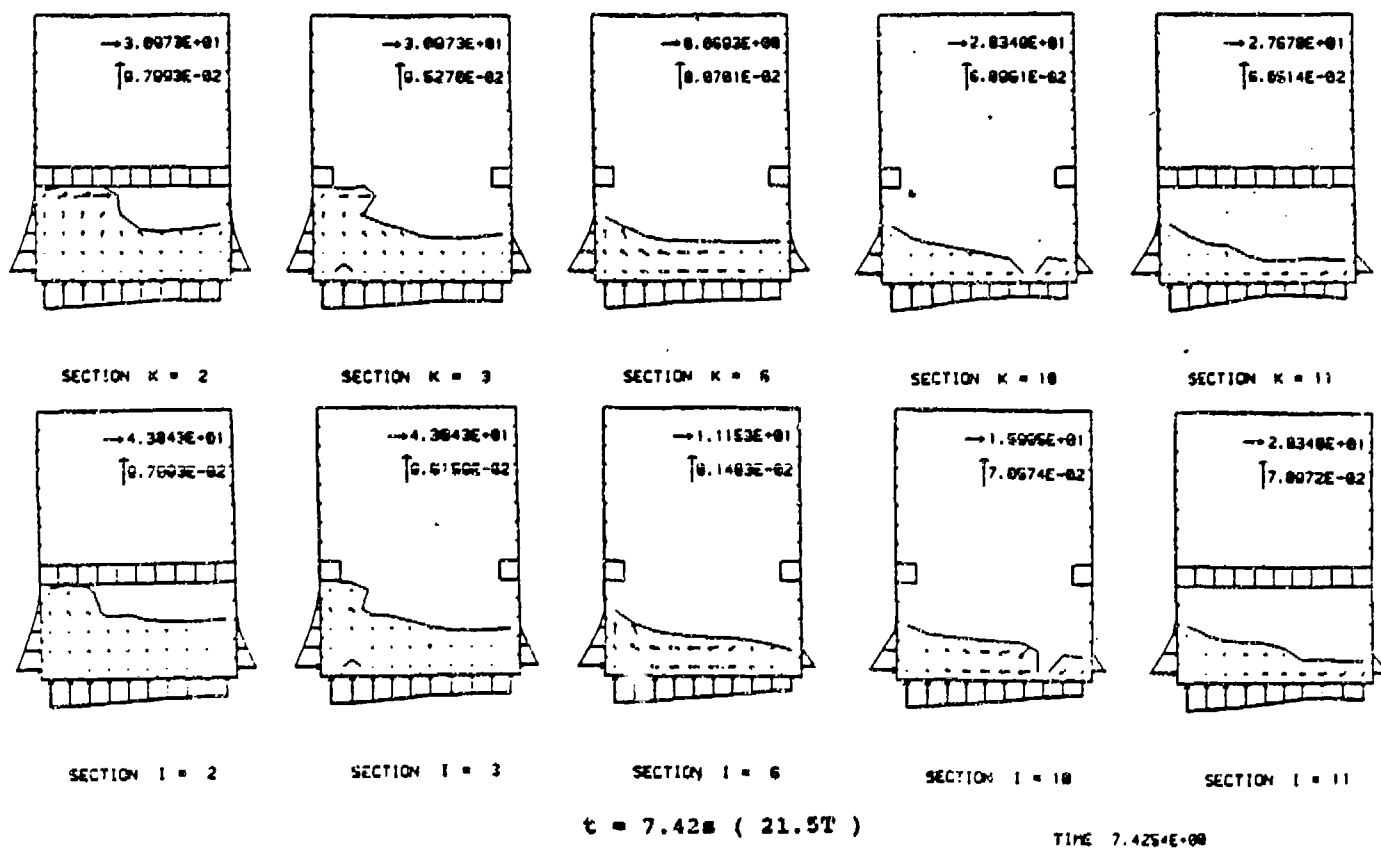
Fig. 21. Velocity plot for shallow water sloshing under vertical excitation (horizontal baffles)

(a) t = 5.69s (16.5T)   (b) t = 6.04s (17.5T)   (c) t = 7.42s (21.5T)

Fig. 22. Surface plot for shallow water sloshing under vertical excitation (horizontal baffles)

SECTION K = 2   SECTION K = 5   SECTION K = 6   SECTION K = 7   SECTION K = 11

SECTION I = 2   SECTION I = 3   SECTION I = 6   SECTION I = 10   SECTION I = 11

t = 7.42s (21.5T)

TIME 7.423E+00
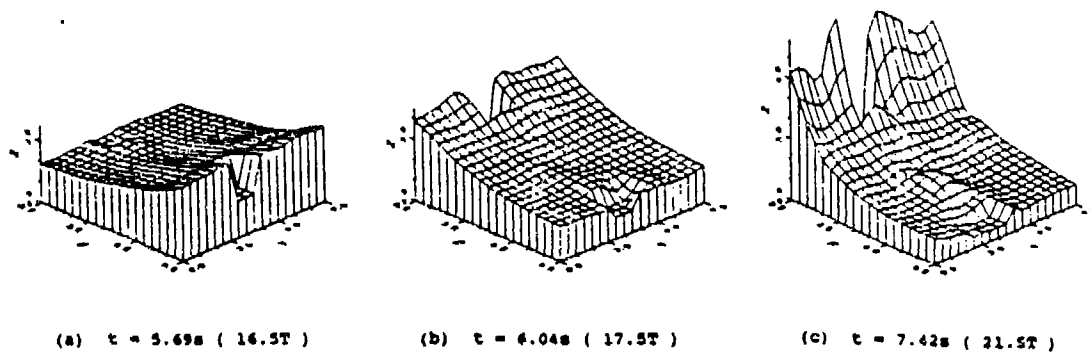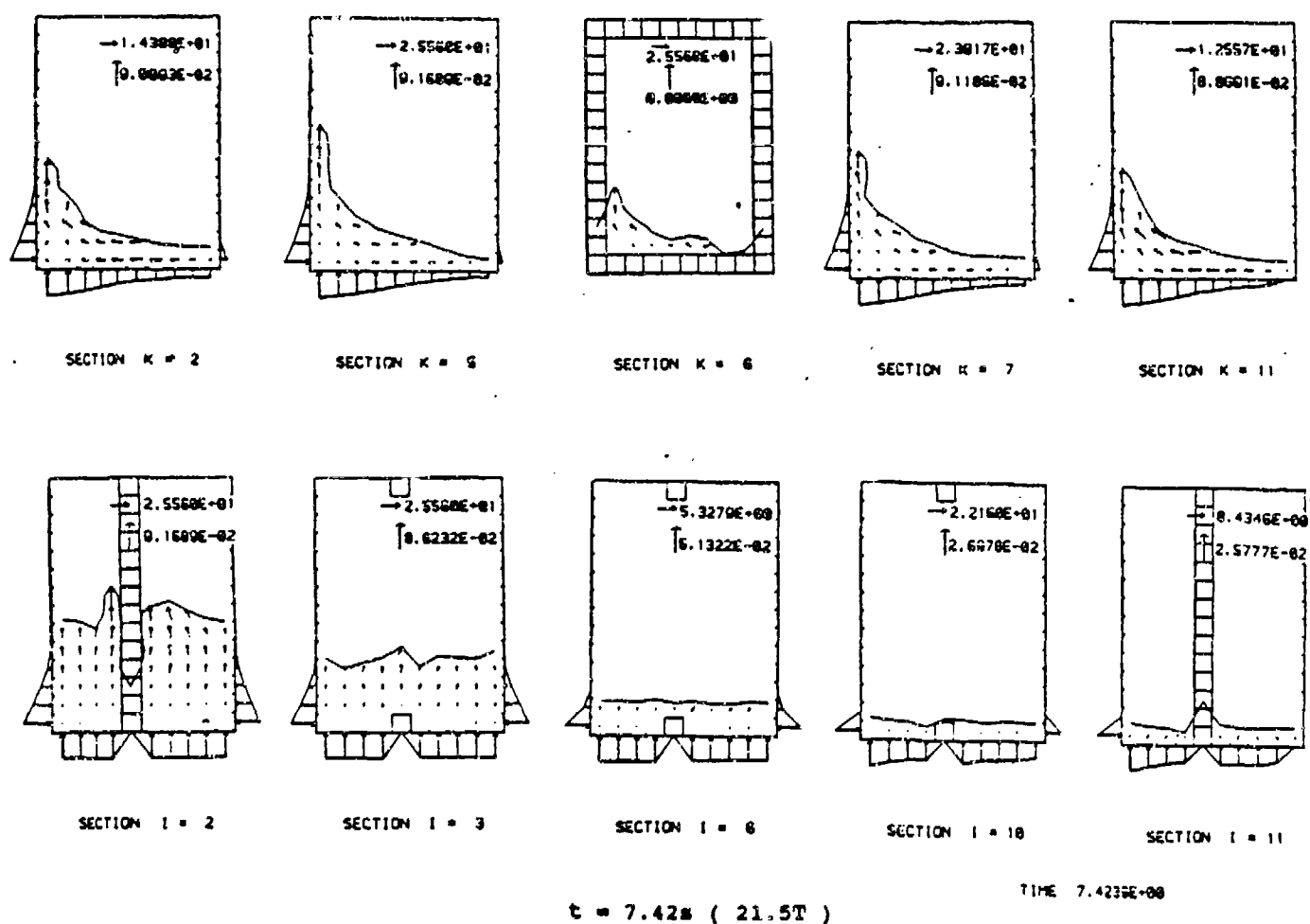
Fig. 23. Velocity plot for shallow water sloshing under vertical excitation (vertical baffles)

56
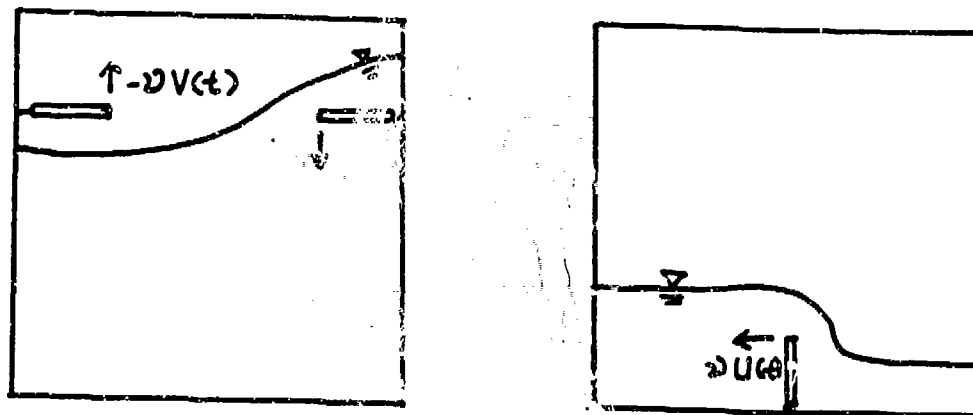
Fig. 24. Active baffle for the control of liquid sloshing
          (a) deep water case; (b) shallow water case

(a)

(b)
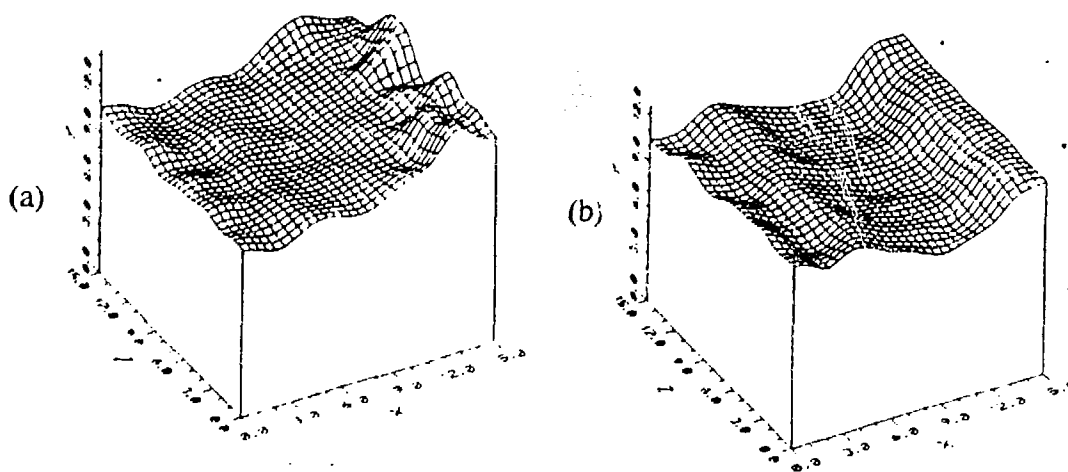
Fig. 25. Free surface plot for deep water cases
          (a) with fixed baffle; (b) with active baffle
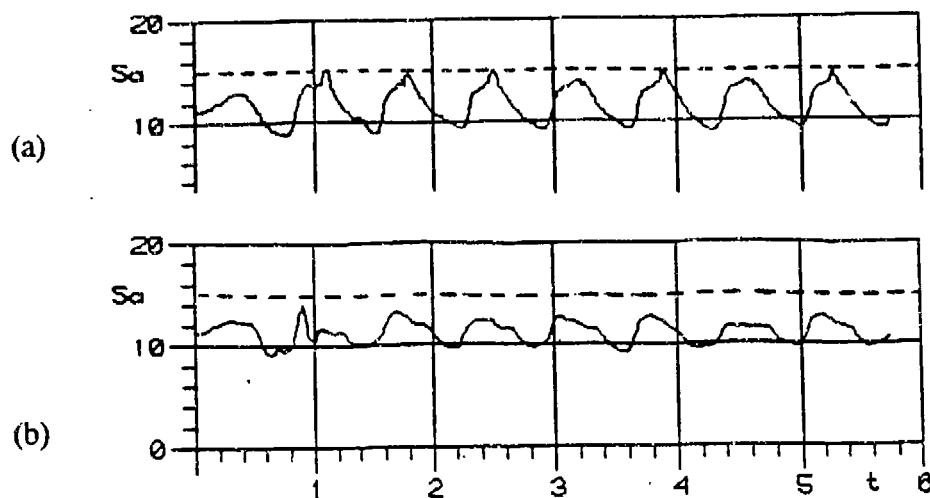
Fig. 26. Effect of baffles on surface height history
(a) baffle fixed; (b) baffle active
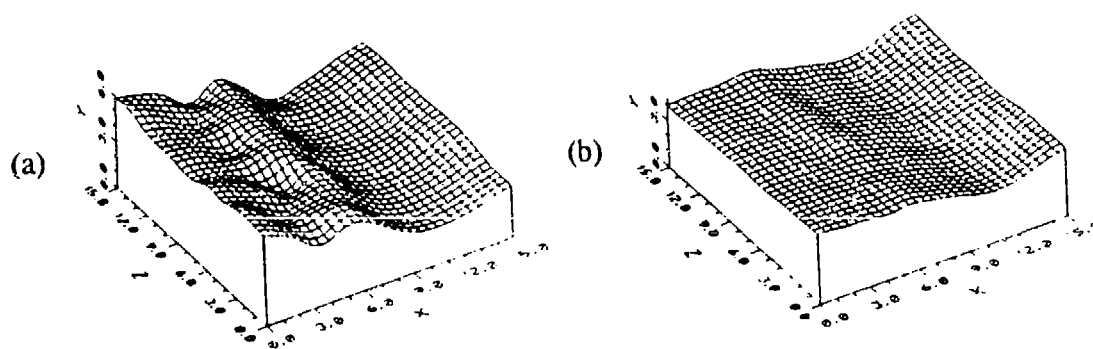
Fig. 27. Free surface plot for shallow water cases
(a) baffle fixed; (b) baffle active
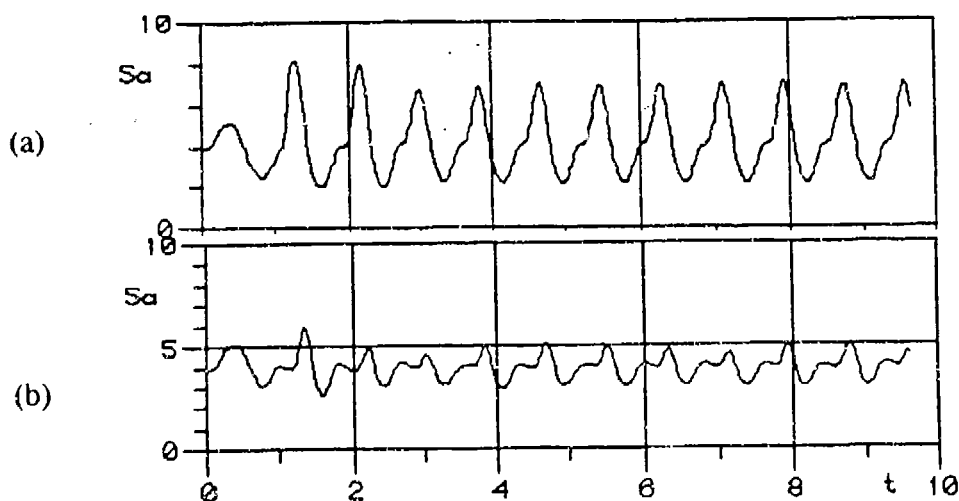
Fig. 28. Effect on baffles on surface height history
(a) baffle fixed; (b) baffle active
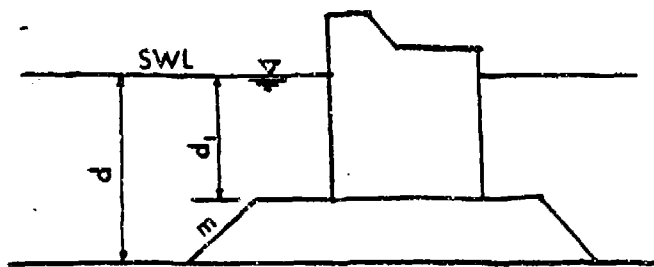
Fig. 29. Definition sketch
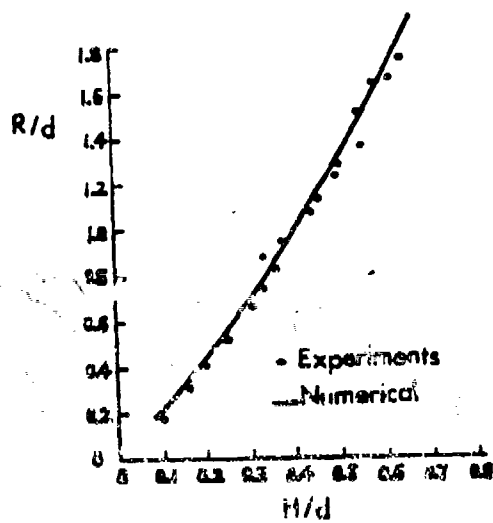
Fig. 30. Comparison of wave run-up on a vertical wall with
          Experimental Data
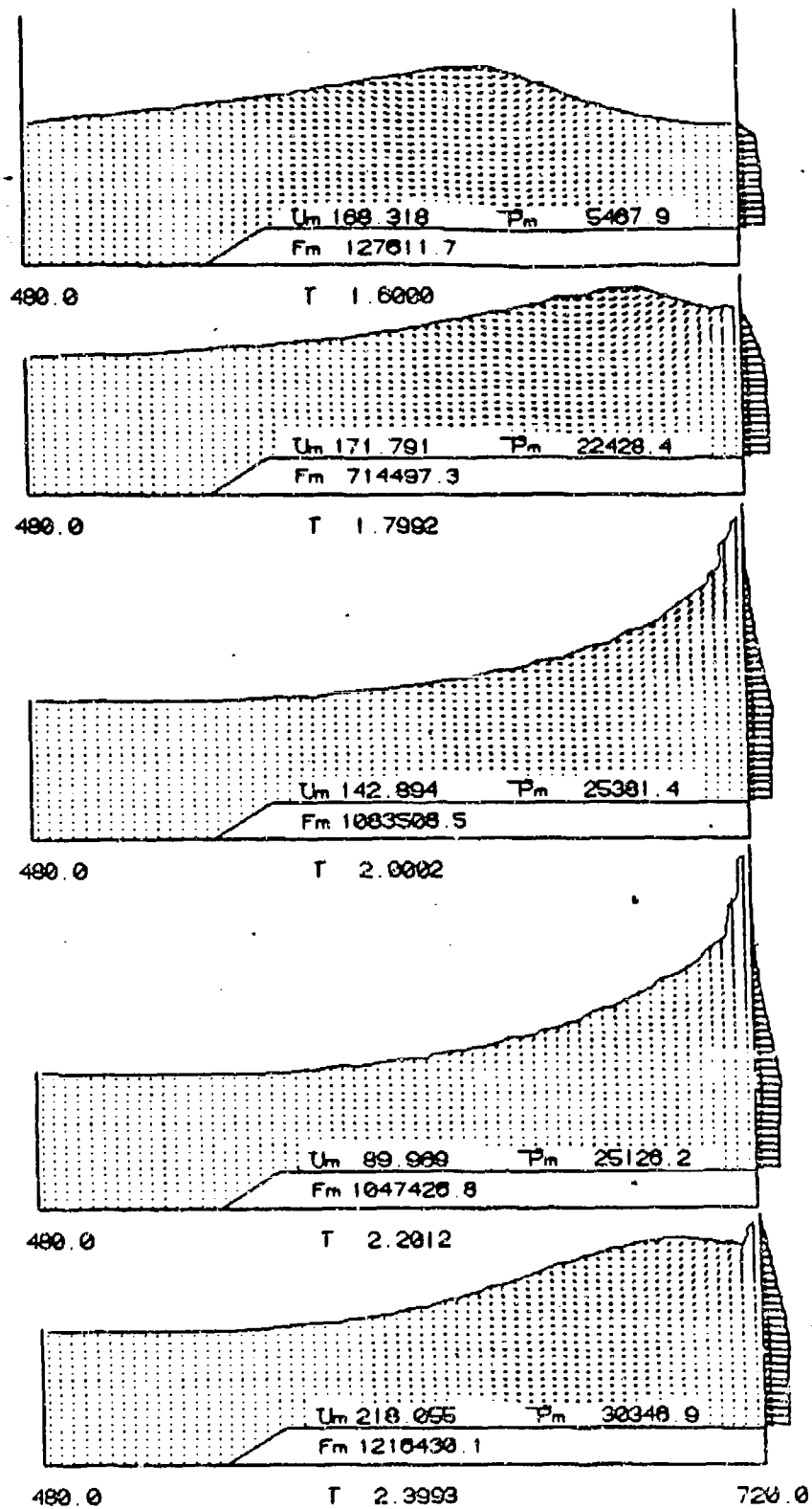
Fig. 31. Flow field plot in front of wall (H/d=0.54, d₁/d=0.71)

Um 191.834   Pm   1752.6
Fm   19456.5

480.0   T   1.7189

Um 204.826   Pm   3455.9
Fm   38633.9

480.0   T   1.7583

Um 218.495   Pm   5665.6
Fm   69683.7

480.0   T   1.8024

Um 280.034   Pm   14873.6
Fm   206552.1

480.0   T   1.8382

Um 494.816   Pm   62629.4
Fm 1433092.5

480.0   T   1.8788   720.0
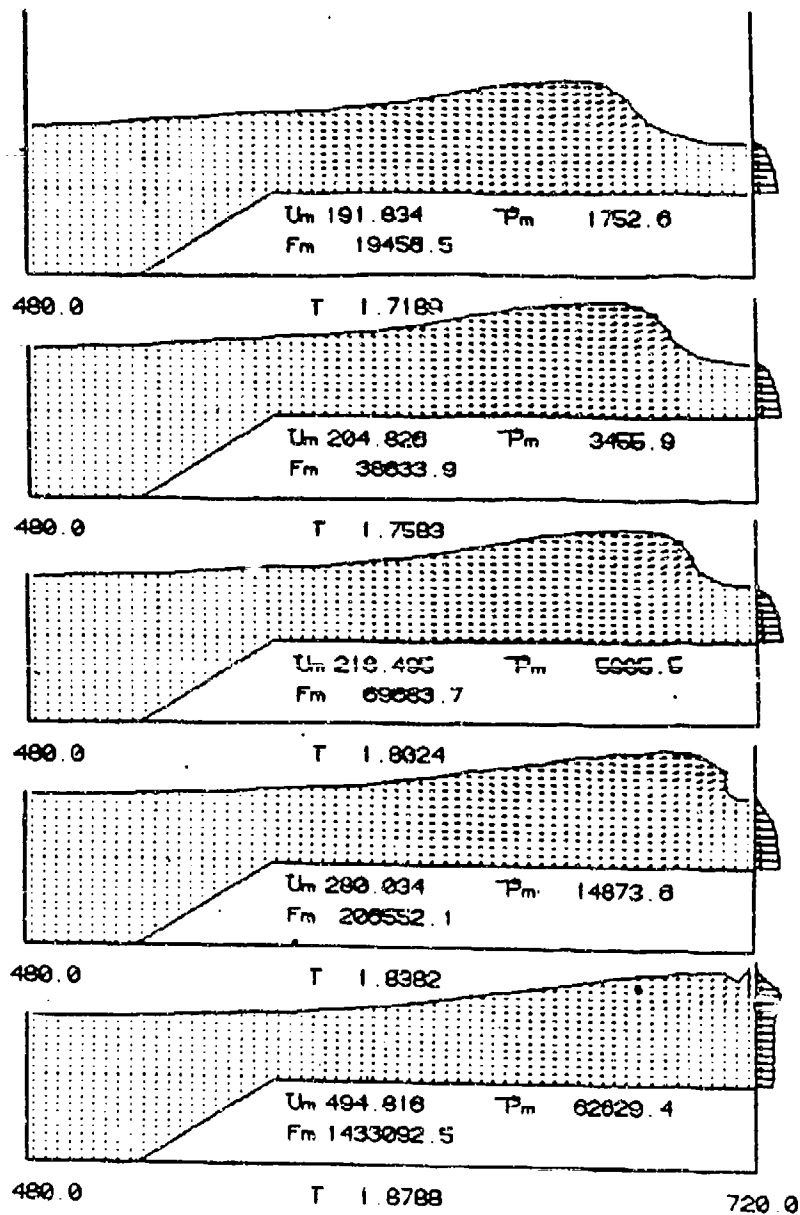
Fig. 32.   Flow field plot in front of wall (H/d=0.54, d_1/d=0.37)

61
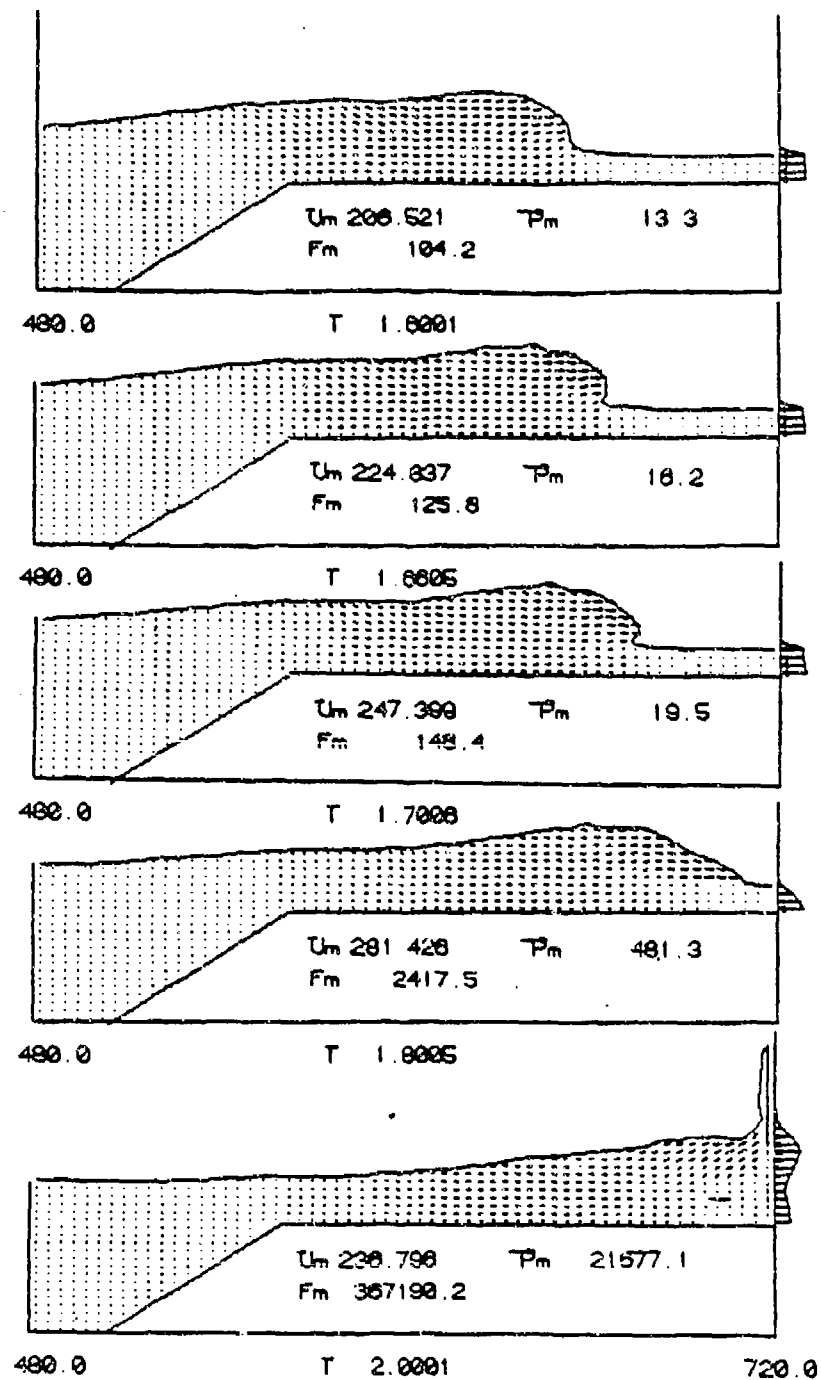
Fig. 33. Flow field plot in front of wall (H/d=0.54, d$_1$/d=0.20)
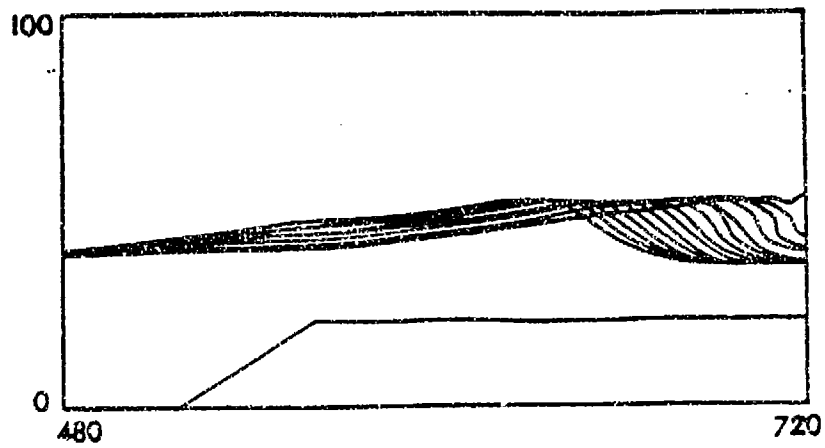
Fig. 34. Evolution of a wave in front of wall (H/d=0.54, d$_1$/d=0.37, t=1.60-1.88, δt=0.02)
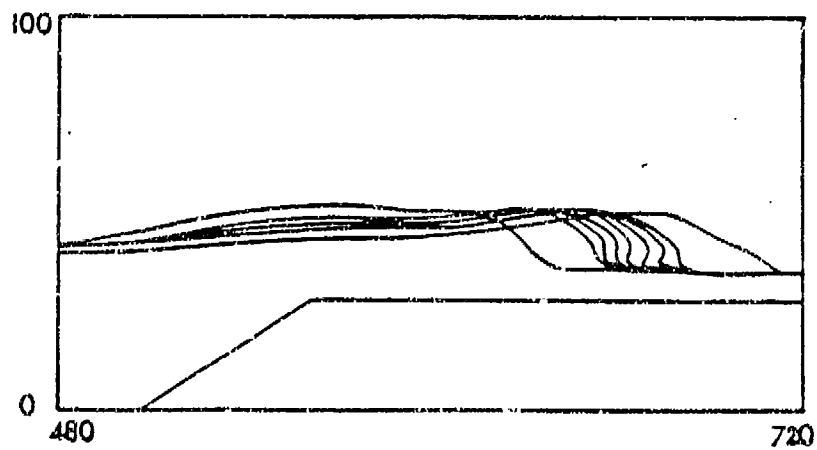
Fig. 35. Evolution of a wave in front of wall (H/d=0.54, d$_1$/d=0.20, t=1.40, 1.50, 1.62, 1.64, 1.66, 1.68, 1.70, 1.72, 1.80)

63
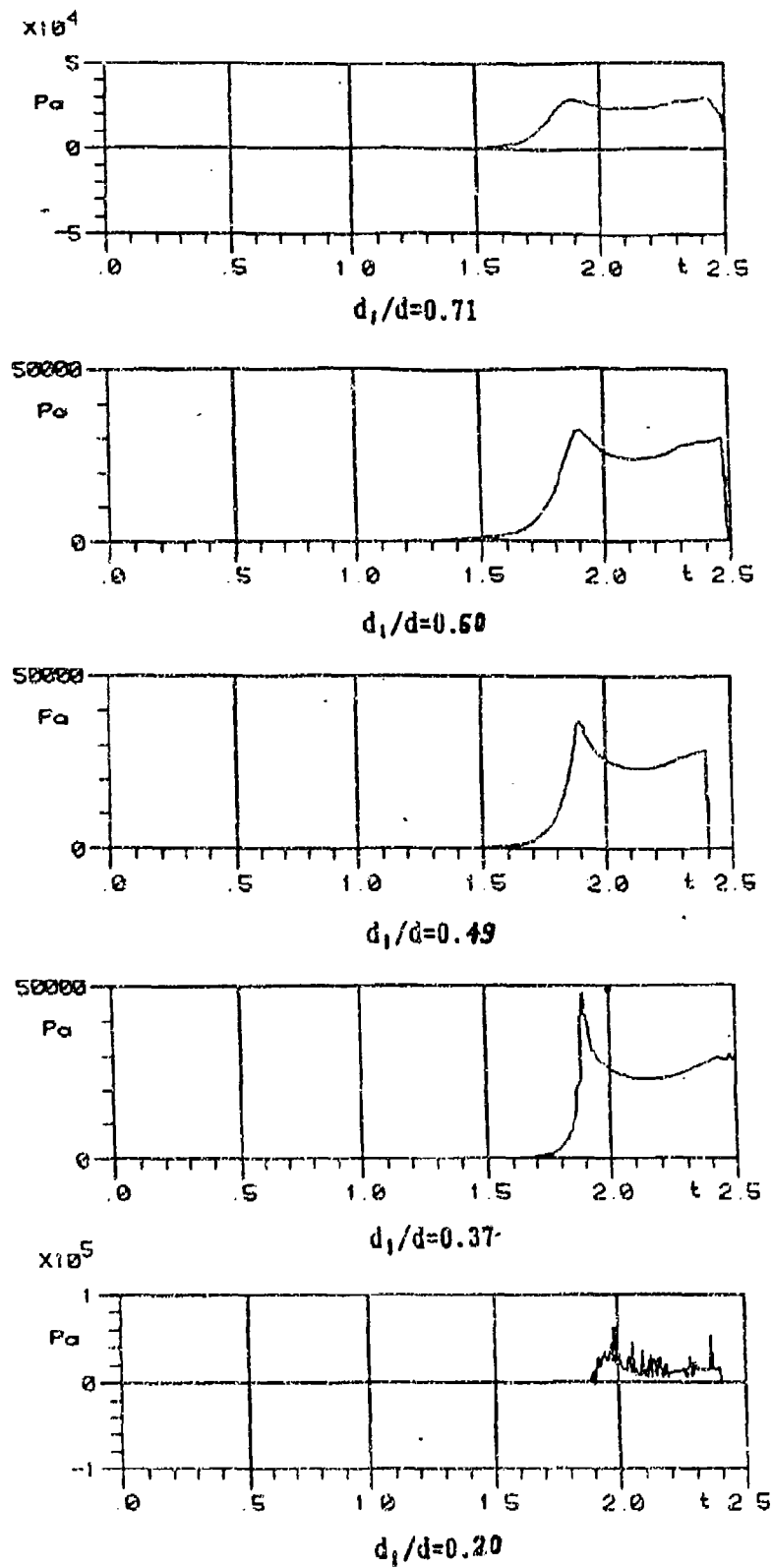
Fig. 36.   Time history of pressure at still water level on the wall
(H/d=0.54)

Um 406.337   Pm   325.4
Fm   3656.1

480.0   T 1.4785

Um 337.337   Pm   618.6
Fm   6674.6

480.0   T 1.5183

Um 425.929   Pm   1302.7
Fm 13689.6

480.0   T 1.5587

Um 316.790   Pm   1965.1
Fm 20578.2

480.0   T 1.5983

Um 428.120   Pm   4993.3
Fm 52624.9

480.0   T 1.6375

Um 540.058   Pm 106801.0
Fm 1853586.5

480.0   T 1.6778   720.0
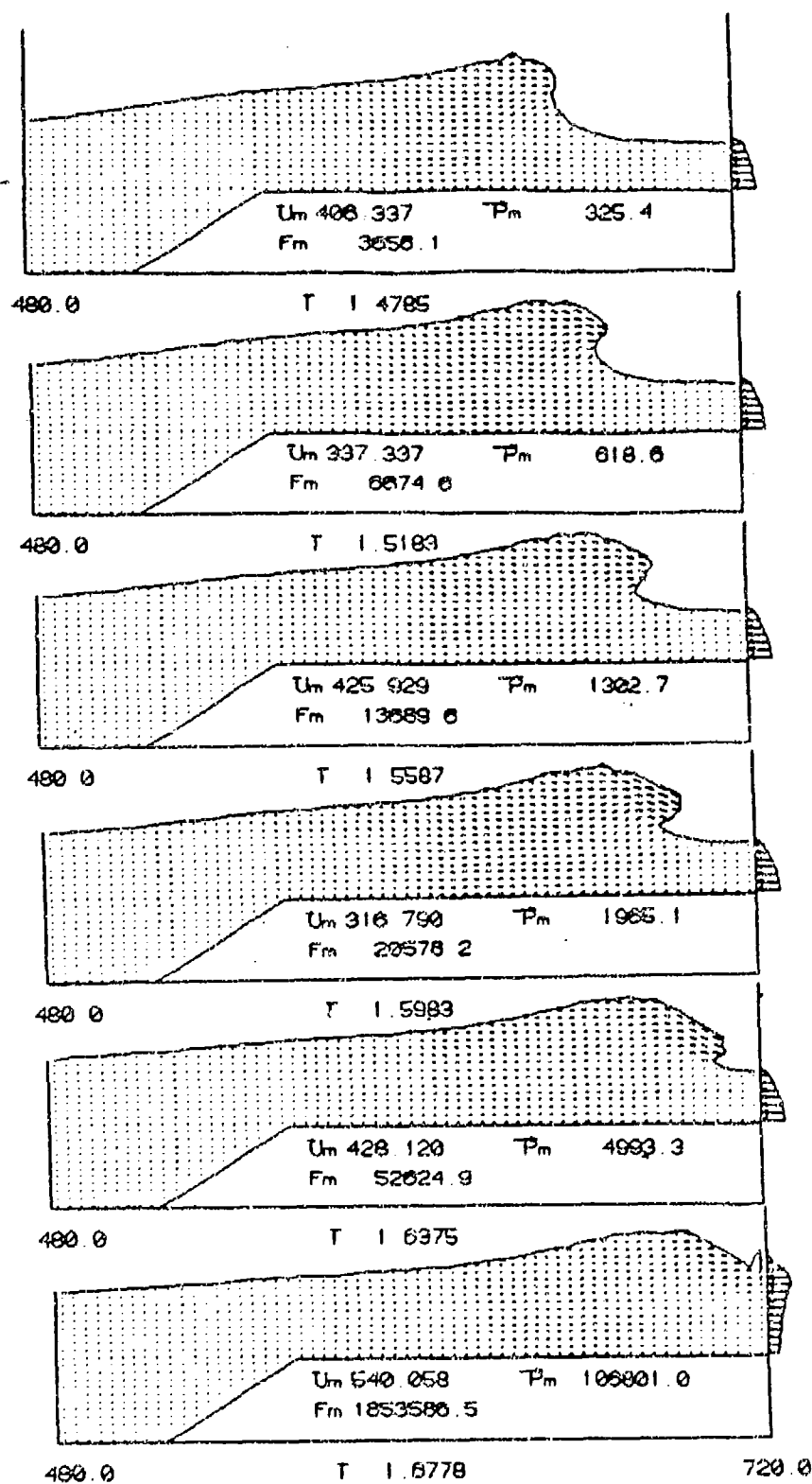
Fig. 37.   Flow field plot in front of wall (H/d=0.78, d$_1$/d=0.37)

65
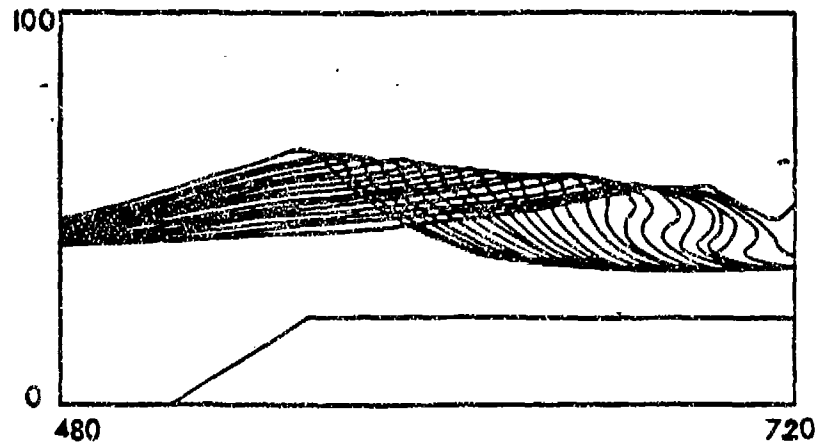
Fig 38. Evolution of a wave in front of wall (H/d=0.78, d_1/d=0.37, t=1.20-1.68, δt=0.02)
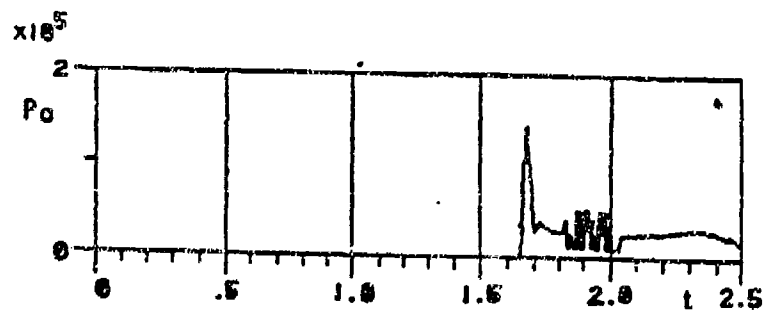
Fig. 39. Time history of pressure at still water level on the wall (H/d-0.78, d_1/d-0.37)
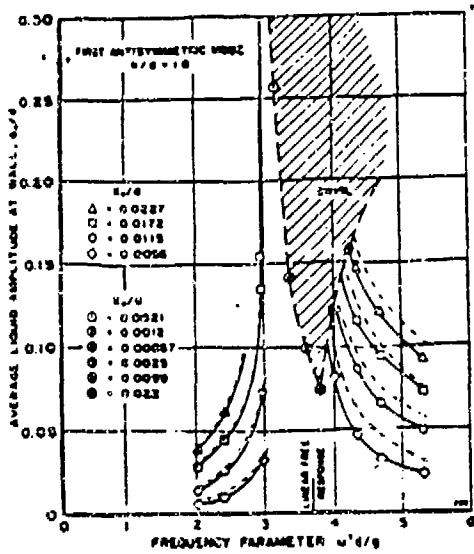
Fig. 40. Comparison of the liquid free surface response, numarical results, - - - - - - - experimental results (Ref. 41)
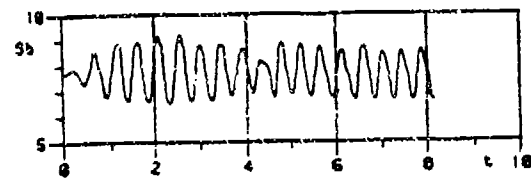
(a) Wave Height
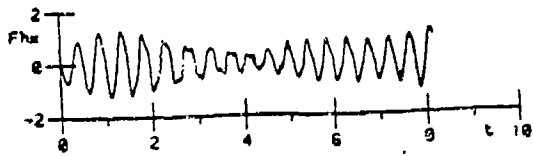
(c) In-line Force
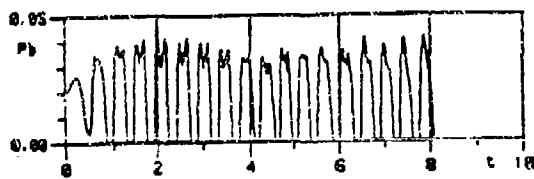
(b) Pressure
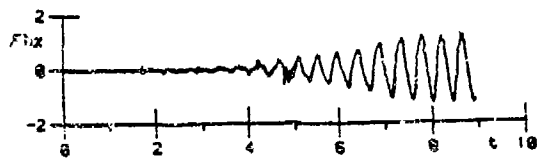
(d) Transverse Force

Fig. 41. Wave height, pressure and force history - lateral sloshing in cylindrical tank

(a)   (b)   (c)   (d)

(e)   (f)   (g)   (h)
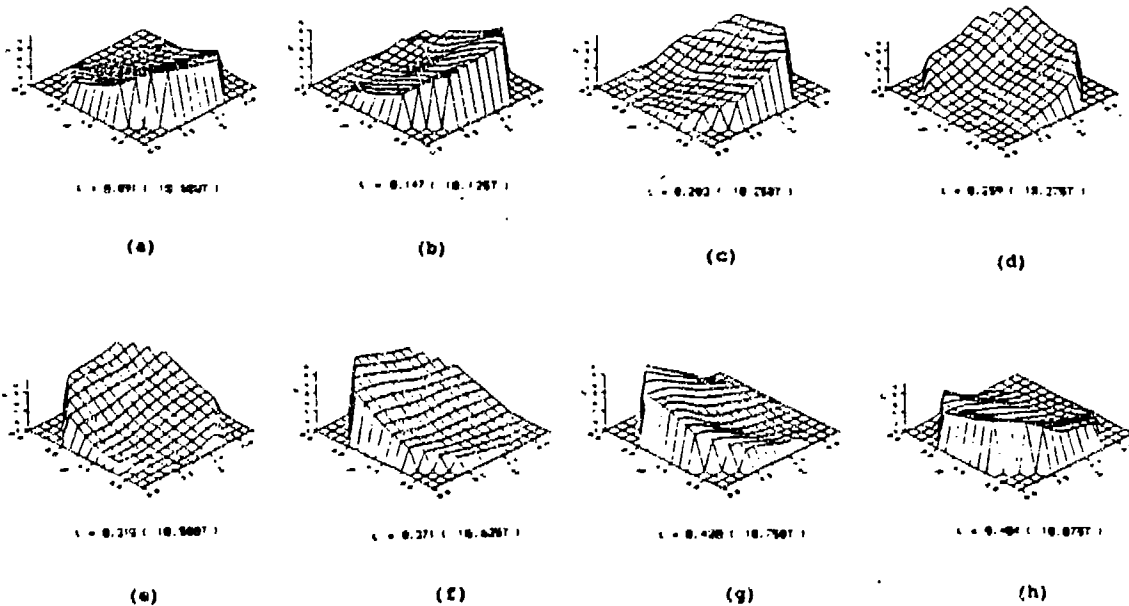
Fig. 42. Surface plot showing swirl phenomena - lateral sloshing in cylindrical tank
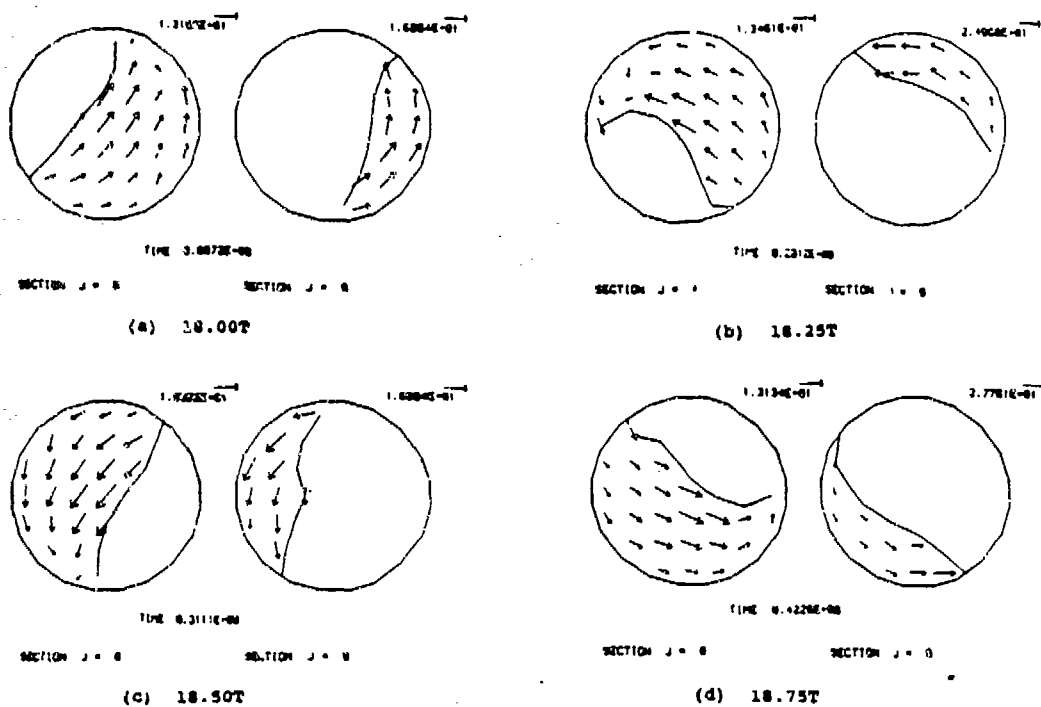
Fig. 43. Flow field plot for horizontal sections J=8 and J=9
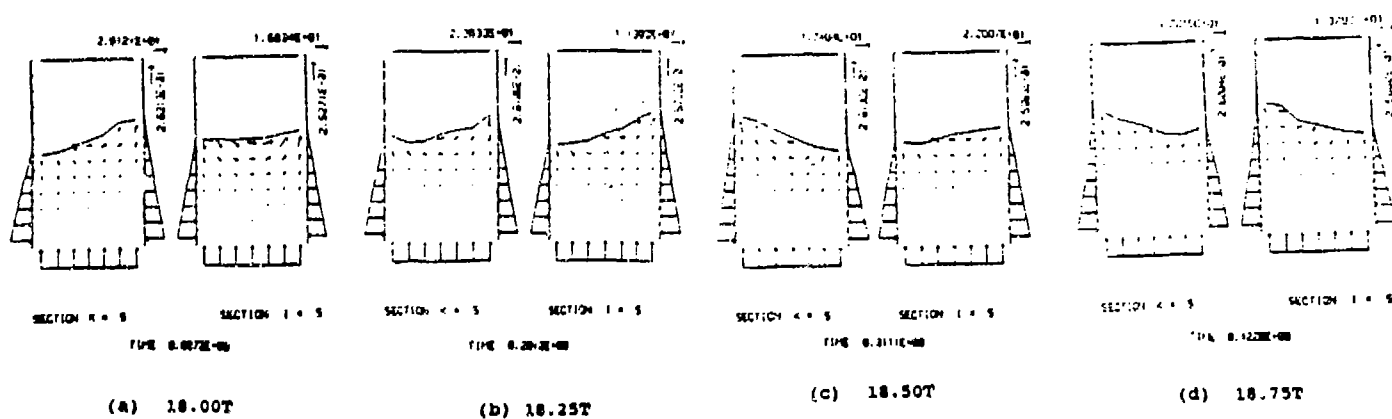
Fig. 44. Flow field plot for vertical sections K=5 and I=5
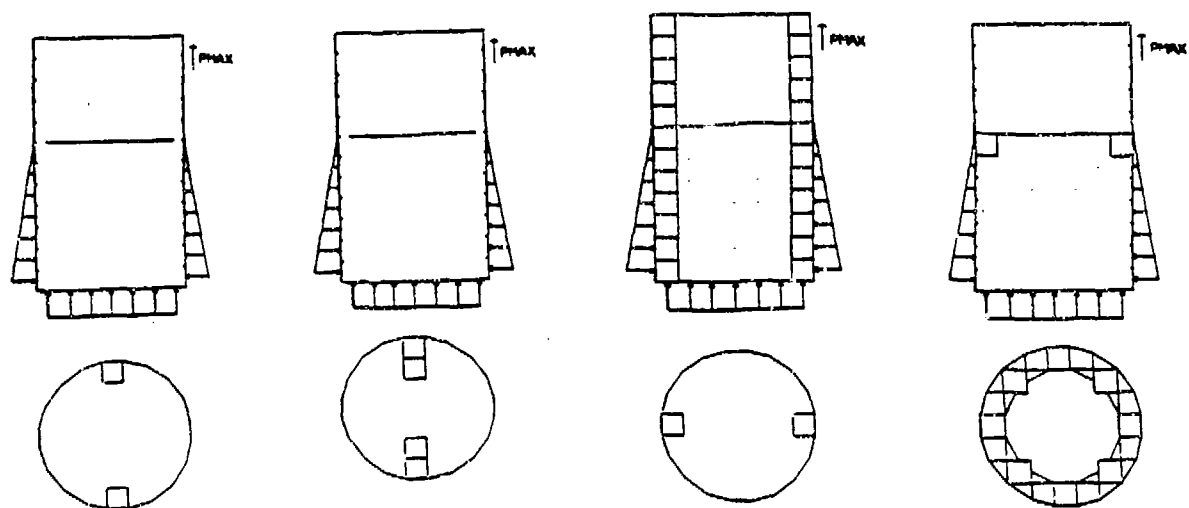
Fig. 45.   Arrangement of typical baffles

(a) Wave Height

(b) Pressure

(c) In-line Force

(d) Transverse Force
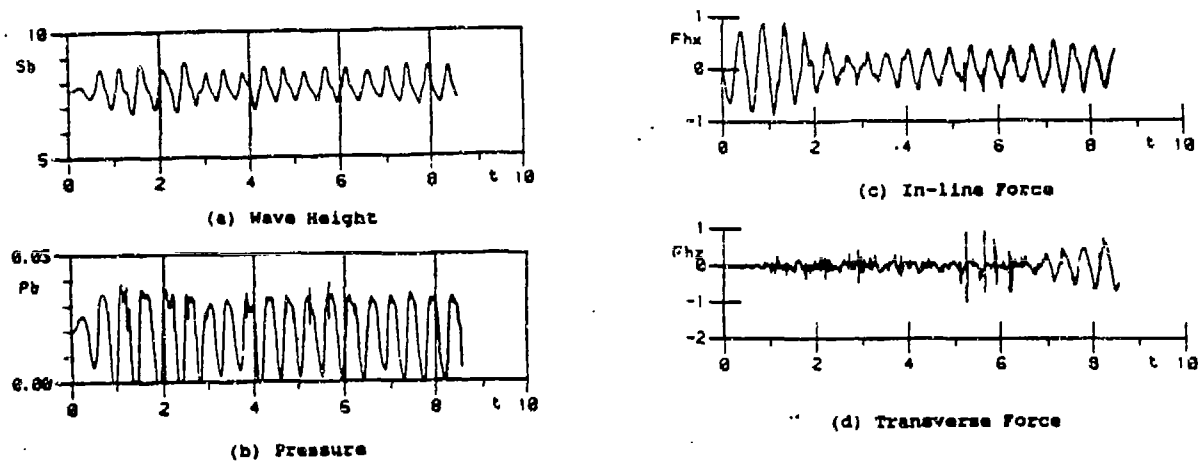
Fig. 46.   Wave height, pressure and force history - effect of vertical splitter plates

(a)   (b)   (c)   (d)

(e)   (f)   (g)   (h)
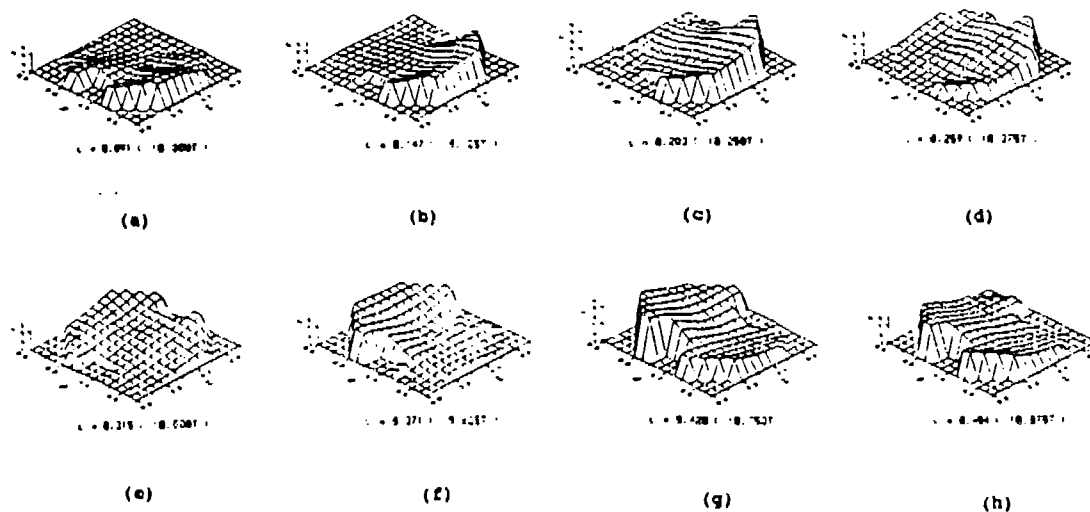
Fig. 47.   Surface plot showing the effect of vertical splitter plates
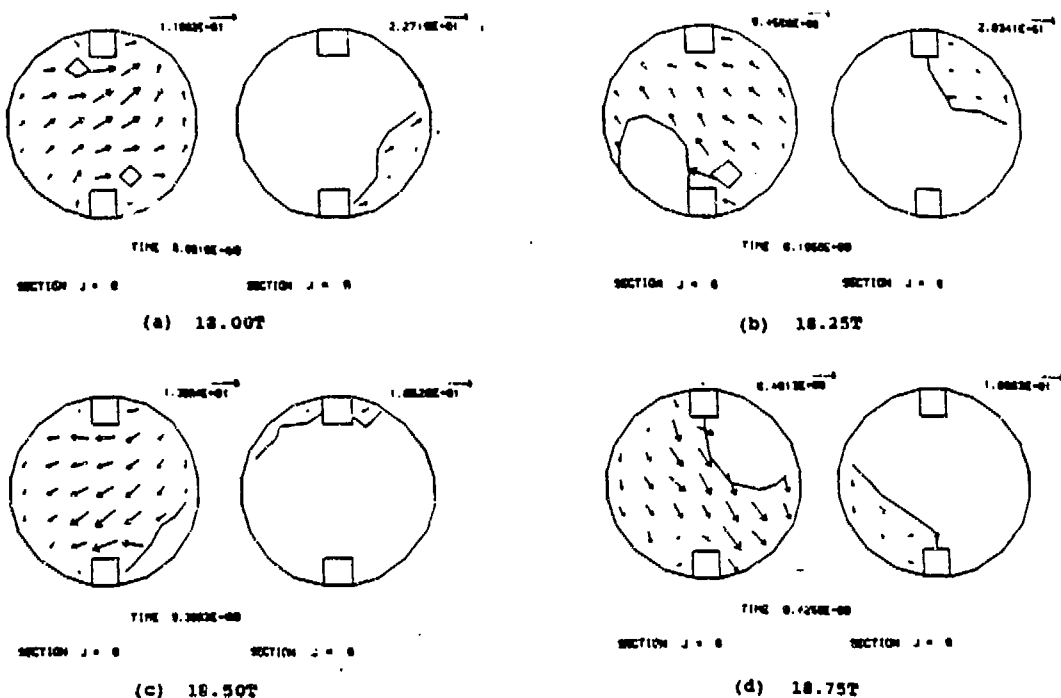
Fig. 48. Flow field plot for horizontal sections J=8 and J=9

Fig. 49. Flow field plot for vertical sections K=5 and I=5

70

(a) Wave Height

(b) Pressure

(c) In-line Force

(d) Transverse Force
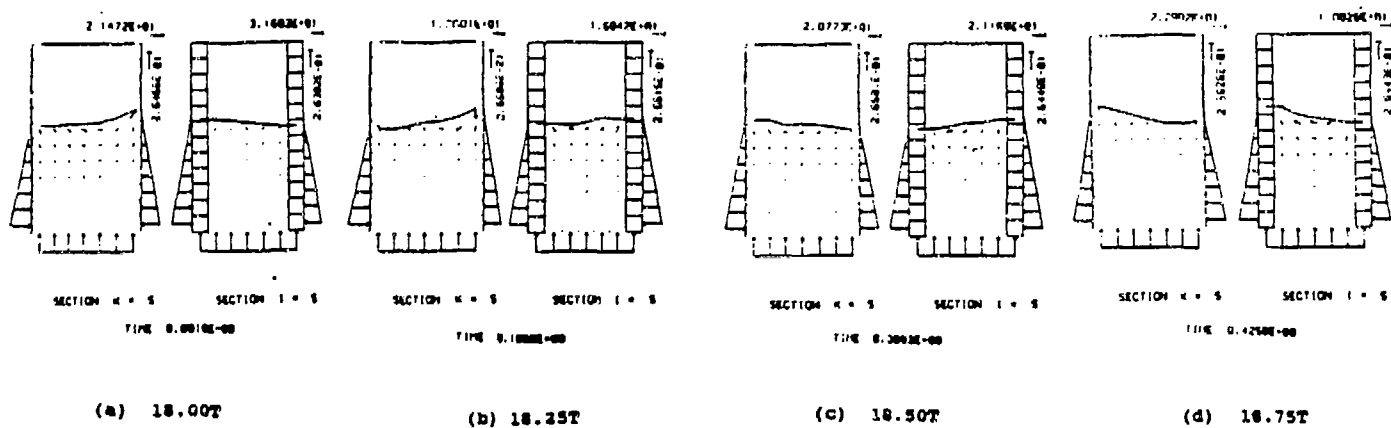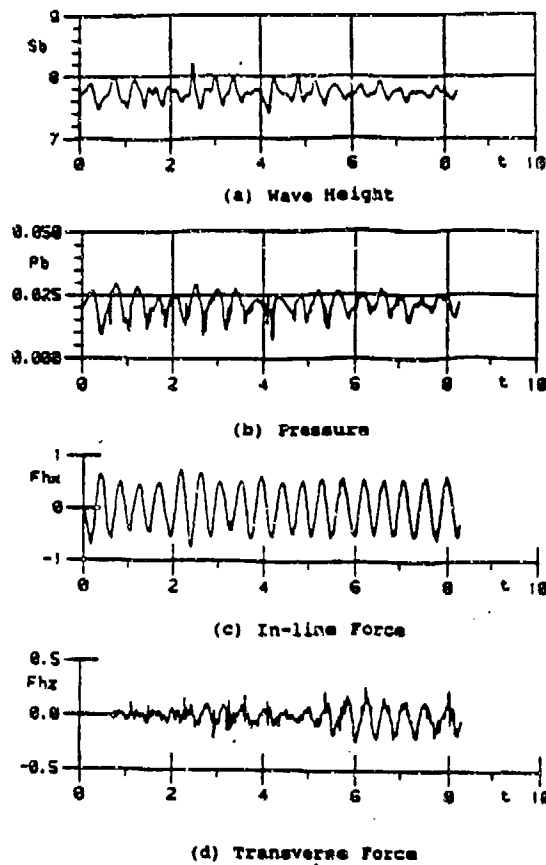
Fig. 50. Wave height, pressure and force history - effects of longer vertical splitter plates
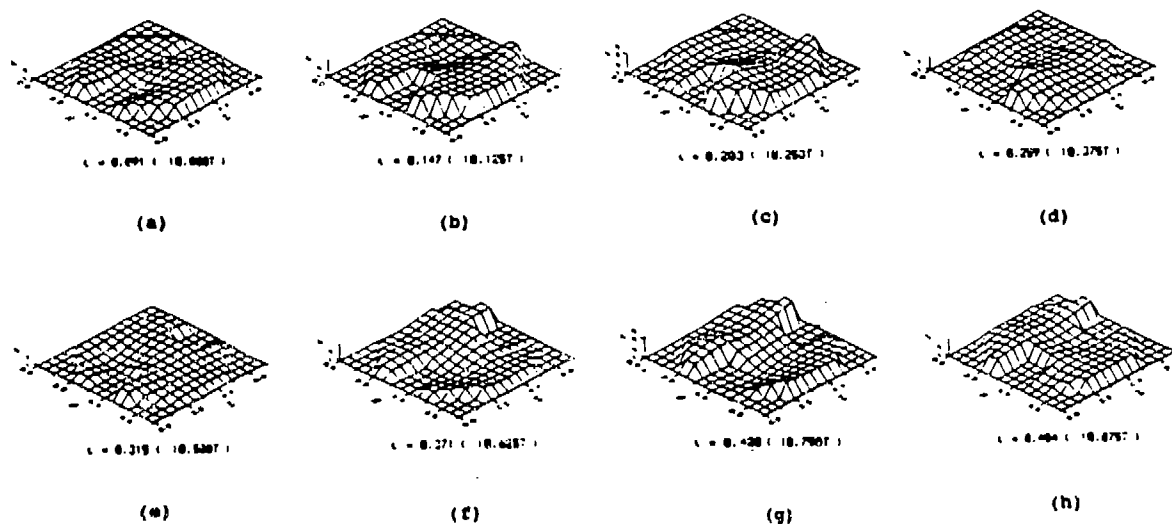
Fig. 51. Surface plot showing the effect of longer vertical splitter plates

71
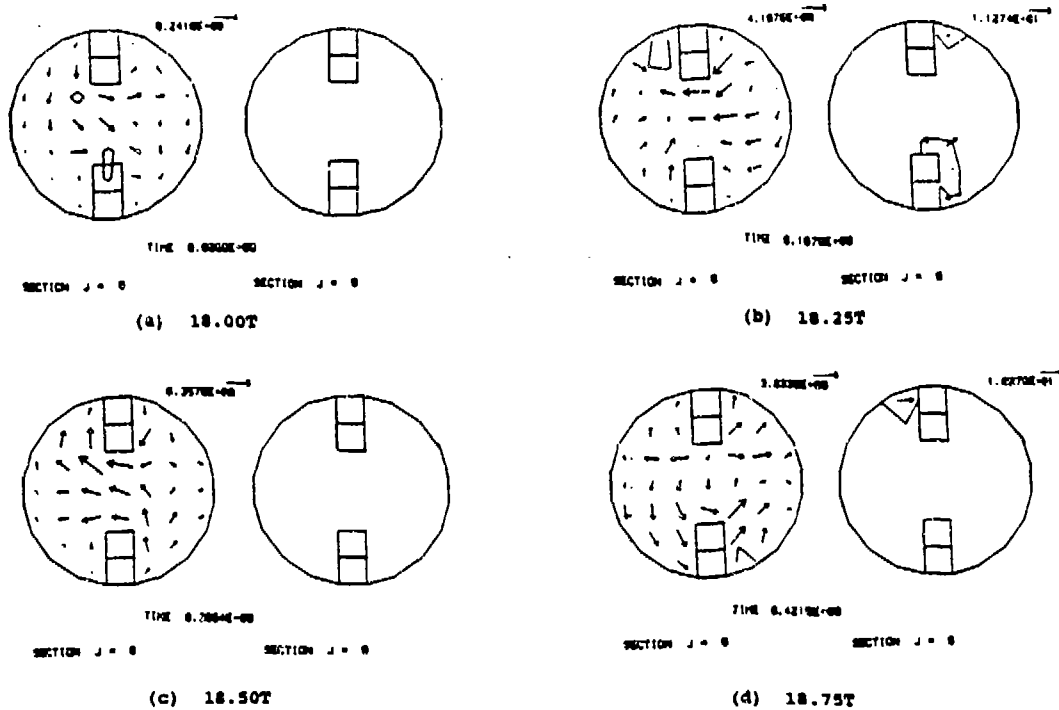
Fig. 52. Flow field plot for horizontal sections J=8 and J=9
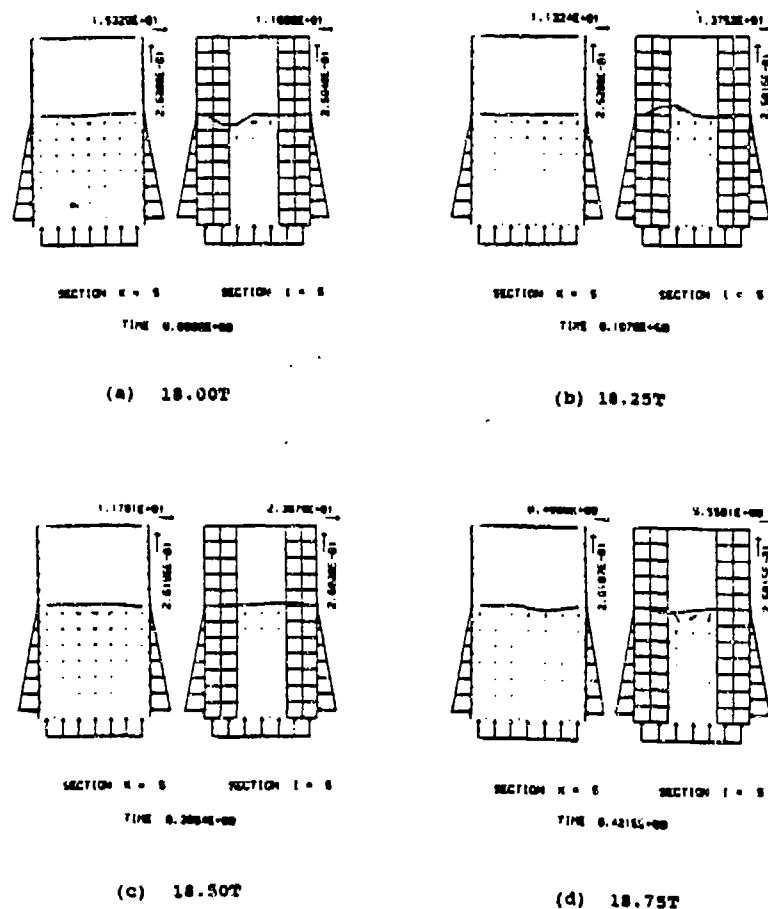
Fig. 53. Flow field plot for vertical sections K=5 and I=5
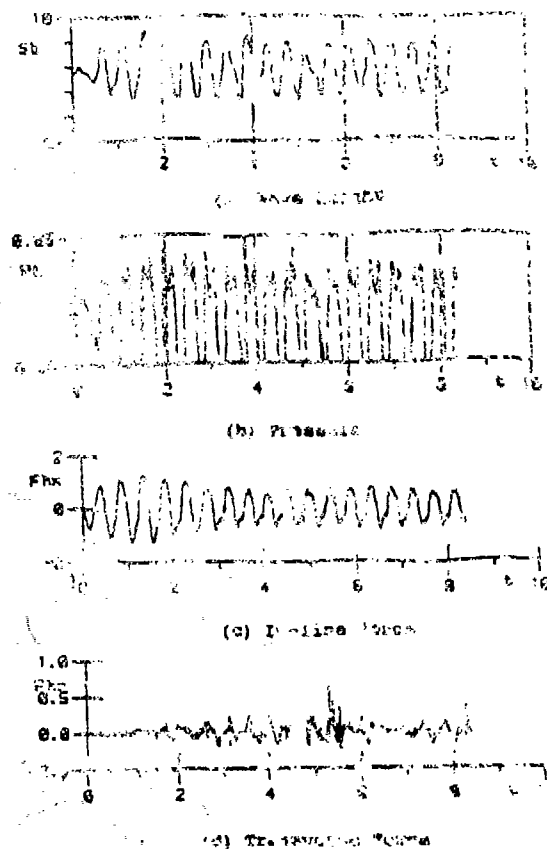
Fig. 54. Wave height, pressure and force history - effect of in-line
vertical splitter plates
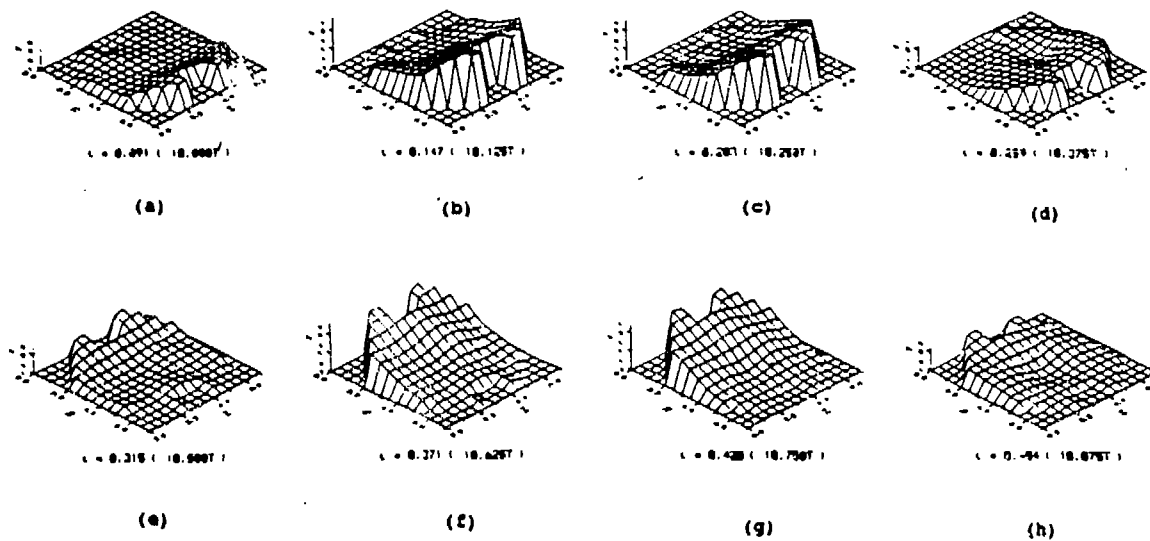
Fig. 55. Surface plot showing the effect of effect of in-line vertical
splitter plates

(a) 18.00T

(b) 18.25%

(c) 18.50T

(d) 18.75T

Fig. 56.   Flow field plot for horizontal sections J=8 and J=9

(a) 18.00T

(b) 18.25T
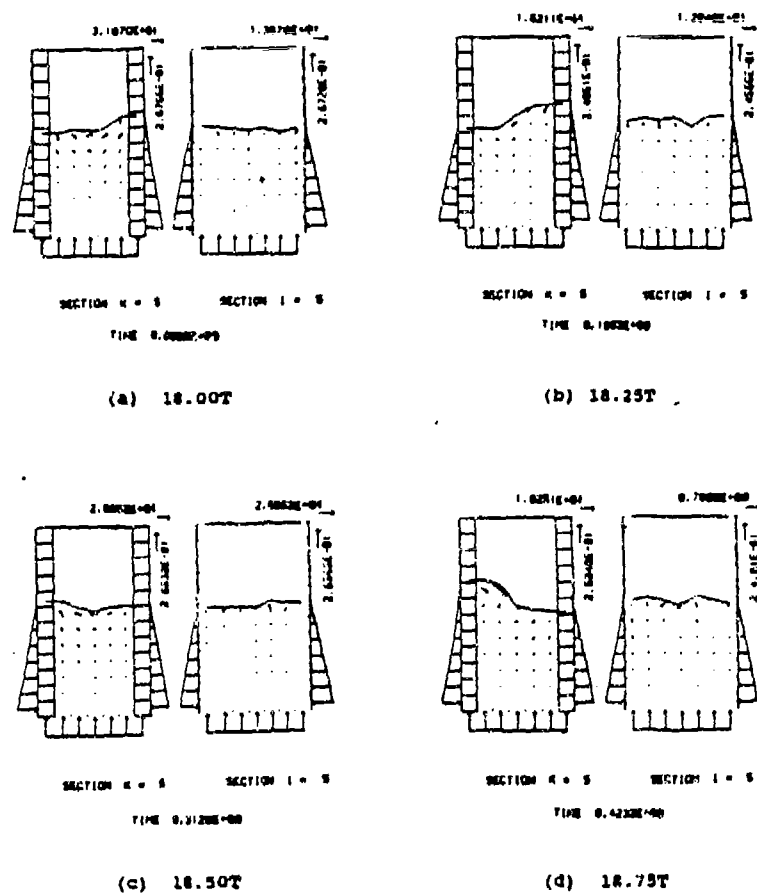
(c) 18.50T

(d) 18.75T

Fig. 57.   Flow field plot for vertical sections K-5 and I-5
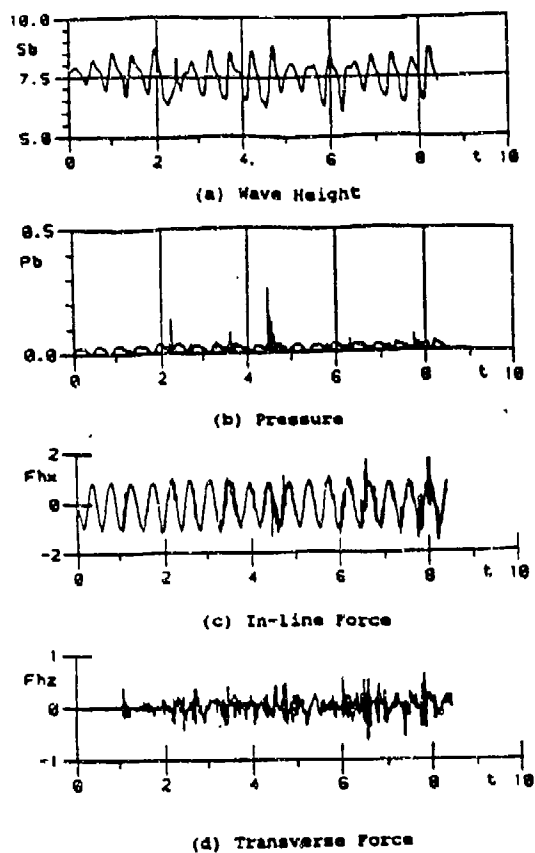
Fig. 58.   Wave height, pressure and force history - effect of a
            horizontal ring baffle.
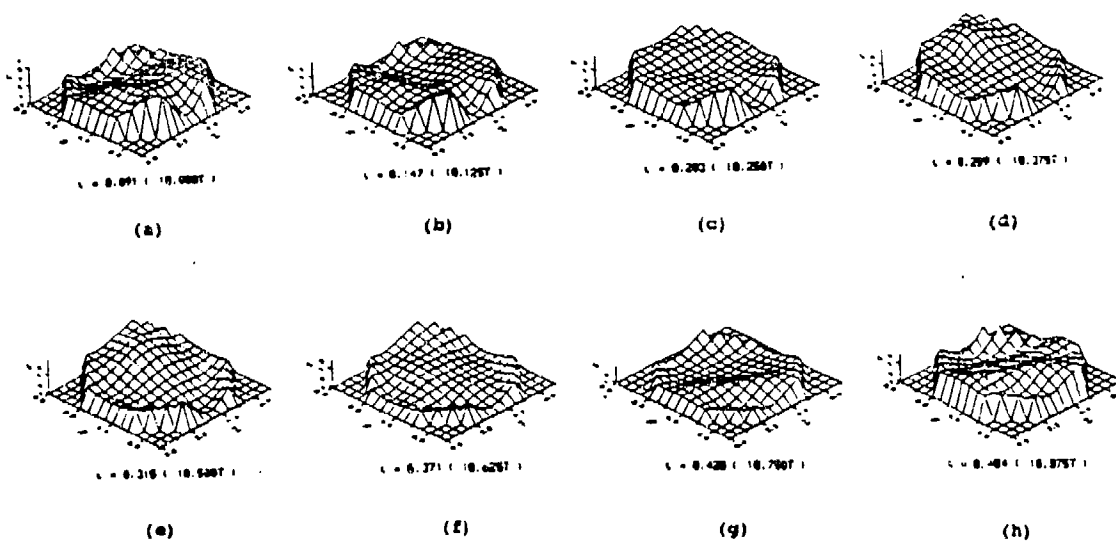
Fig. 59.   Surface plot showing the effect of a horizontal ring baffle.

75
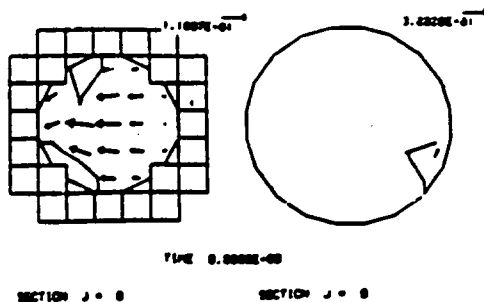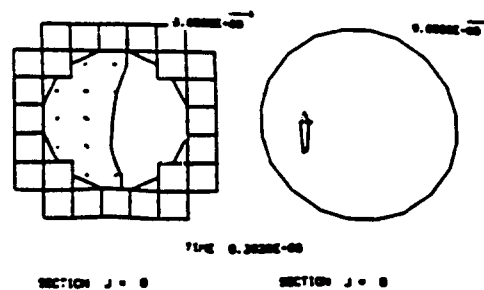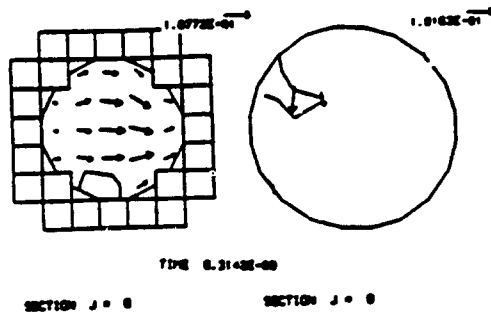
(a) 18.00T   (b) 18.25T
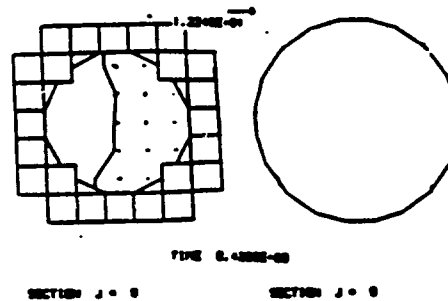
(c) 18.50T   (d) 18.75T

Fig. 60.   Flow field plot for horizontal sections J=8 and J=9
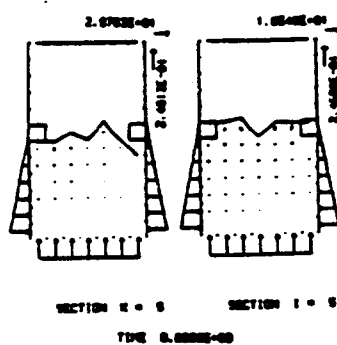
(a) 18.00T   (b) 18.25T
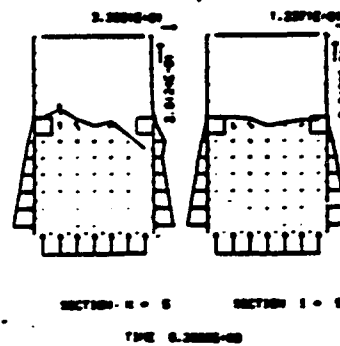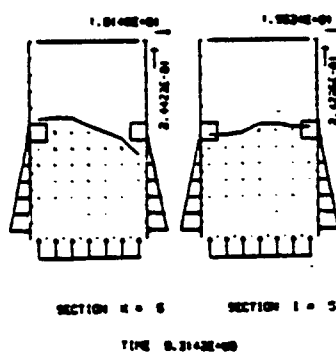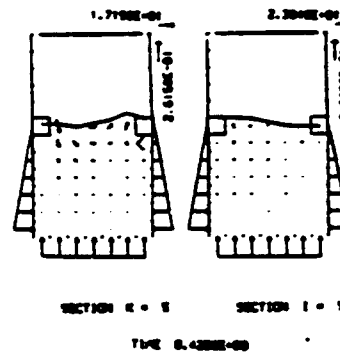
(c) 18.50T   (d) 18.75T

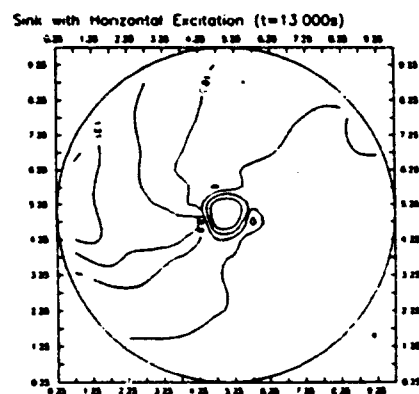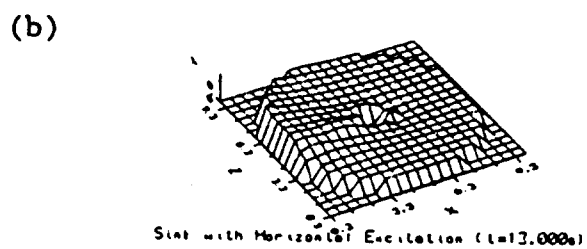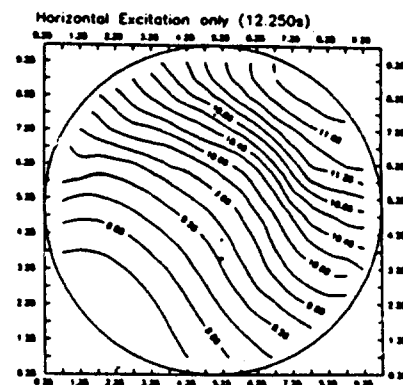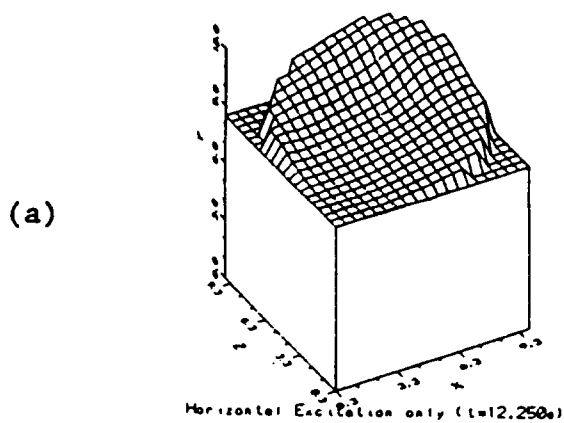Fig. 61.   Flow field plot for vertical sections K=5 and I=5
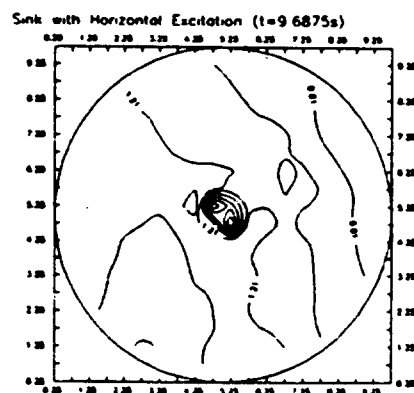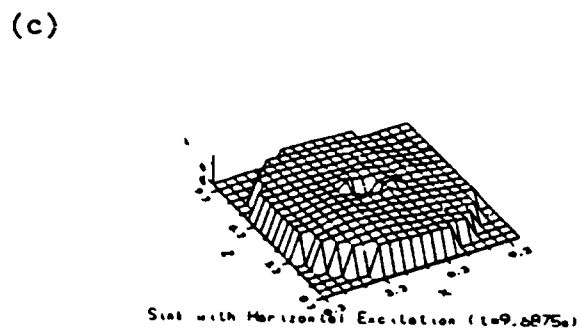
Fig. 62. Surface and surface contour plots at various rates of drainage
(a) no drainage, (b) low drainage, and (c) high drainage